Methods in Wave Propagation and Scattering

by

Henning Braunisch

M. S. Electrical Engineering
Michigan State University, East Lansing, May 1995
Dipl.-Ing. Electrical Engineering
University of Hanover, Germany, November 1996

Submitted to the Department of Electrical Engineering and Computer Science
in partial fulfillment of the requirements for the degree of

Doctor of Philosophy

at the

MASSACHUSETTS INSTITUTE OF TECHNOLOGY

February 2001

Author _____
Department of Electrical Engineering and Computer Science
January 12, 2001

Certified by _____
Jin A. Kong
Professor of Electrical Engineering
Thesis Supervisor

Accepted by _____
Arthur C. Smith
Professor of Electrical Engineering
Chairman, Department Committee on Graduate Students

Methods in Wave Propagation and Scattering

by

Henning Braunisch

Submitted to the Department of Electrical Engineering and Computer Science
on January 12, 2001 in partial fulfillment of the requirements for the
Degree of Doctor of Philosophy

Abstract

Aspects of wave propagation and scattering with an emphasis on specific applications in engineering and physics are examined. Frequency-domain methods prevail. Both forward and inverse problems are considered.

Typical applications of the method of moments to rough surface three-dimensional (3-D) electromagnetic scattering require a truncation of the surface considered and call for a tapered incident wave. It is shown how such wave can be constructed as a superposition of plane waves, avoiding problems near both normal and grazing incidence and providing clean footprints and clear polarization at all angles of incidence. The proposed special choice of polarization vectors removes an irregularity at the origin of the wavenumber space and leads to a wave that is optimal in a least squared error sense. Issues in the application to 3-D scattering from an object over a rough surface are discussed. Approximate 3-D scalar and vector tapered waves are derived which can be evaluated without resorting to any numerical integrations. Important limitations to the accuracy and applicability of these approximations are pointed out.

An analytical solution is presented for the electromagnetic induction problem of magnetic diffusion into and scattering from a permeable, highly but not perfectly conducting prolate spheroid under axial excitation, expressed in terms of an infinite matrix equation. The spheroid is assumed to be embedded in a homogeneous non-conducting medium as appropriate for low-frequency, high-contrast scattering governed by magnetoquasistatics. The solution is based on separation of variables and matching boundary conditions where the prolate spheroidal wavefunctions with complex wavenumber parameter are expanded in terms of spherical harmonics. For small skin depths, an approximate solution is constructed, which avoids any reference to the spheroidal wavefunctions. The problem of long spheroids and long circular cylinders is solved by using an infinite cylinder approximation. In some cases, our ability to evaluate the spheroidal wavefunctions breaks down at intermediate frequencies. To deal with this, a general broadband rational function approximation technique is developed and demonstrated. We treat special cases and provide numerical reference data for the induced magnetic dipole moment or, equivalently, the magnetic polarizability factor. The magnetoquasistatic response of a distribution of an arbitrary number of interacting small conducting and permeable objects is also

investigated. Useful formulations are provided for expressing the magnetic dipole moment of conducting and permeable objects of general shape.

An alternative to Tikhonov regularization for deblurring and inverse diffraction, based on a local extrapolation scheme, is described, analyzed, and illustrated numerically for the cases of continuation of fields obeying Laplace and Helmholtz equations. At the outset of the development, a special deconvolution problem, where a parameter describes the degree of additive blurring, is considered. No *a priori* knowledge on the unblurred data is assumed. A standard solution based on an output least-squares formulation includes a regularization parameter into a linear, shift-invariant filter. The proposed alternative approach takes advantage of the analyticity of the smoothing process with respect to the blurring parameter. Here a simple local extrapolation scheme is employed. The problem is encountered in applications involving potential theories dealing with magnetostatics, electrostatics, and gravity data. As a generalization to the dynamic case, inverse diffraction of scalar waves is considered. Examples are presented and the two methods compared numerically.

The problem of inferring unknown geometry and material parameters of a waveguide model from noisy samples of the associated modal dispersion curves is considered. In a significant reduction of the complexity of a common inversion methodology, the inner of two nested iterations is eliminated: The approach described does not employ explicit fitting of the data to computed dispersion curves. Instead, the unknown parameters are adjusted to minimize a cost function derived directly from the determinant of the boundary condition system matrix. This results in a very efficient inversion scheme that, in the case of noise-free data, yields exact results. Multi-mode data can be simultaneously processed without extra complications. Furthermore, the inversion scheme can accommodate an arbitrary number of unknown parameters, provided that the data have sufficient sensitivity to these parameters. As an important application, the sonic guidance condition for a fluid-filled borehole in an elastic, homogeneous, and isotropic rock formation is considered for numerical forward and inverse dispersion analysis. The parametric inversion with uncertain model parameters and the influence of bandwidth and noise are investigated numerically. The cases of multi-frequency and multi-mode data are examined. Finally, the borehole leaky-wave modes are classified according to the location of the roots of the characteristic equation on a multi-sheeted Riemann surface. A comprehensive set of dipole leaky-wave modal dispersions is computed. In an independent numerical experiment the excitation of some of these modes is demonstrated. The utilization of leaky-wave dispersion data for inversion is discussed.

Thesis Supervisor: Jin A. Kong
Title: Professor of Electrical Engineering

Acknowledgments

I would sincerely like to thank Professor Kong for continuously supporting and guiding my research at the Massachusetts Institute of Technology. I enjoyed considerable freedom in pursuing research topics of my own choice, which ultimately made the creation of this thesis possible. Anybody familiar with Professor Kong's writings and teaching will undoubtedly recognize his influence on this dissertation.

I am indebted to Tarek M. Habashy for his support during my summer internships at Schlumberger-Doll Research, Ridgefield, Connecticut in 1995 and 1998–2000. Over the years he has been both a mentor and friend to me. He suggested the third and fourth topics in this thesis and helped at every stage of the development. I wish to express my thanks also to the numerous other scientists and engineers at Schlumberger with whom I have had the privilege to interact. Through technical and non-technical discussions they have given me invaluable insights into research and engineering.

I am grateful to Chi O. Ao, Kung-Hau Ding, Ronald R. Haladyna, Joel T. Johnson, Kevin O'Neill, Jahir Pabon, Shih-En Shih, Bikash K. Sinha, David H. Staelin, Leung Tsang, Y. Eric Yang, and Yan Zhang for their comments and suggestions regarding the projects in this thesis and their description. Special thanks go to Kevin O'Neill for providing the experimental data from a creative electromagnetic induction measurement carried out by him.

I would like to thank Abraham Bers for his academic advice and the encouraging conversations that marked the beginning of each semester of my doctoral program. The effort of the following individuals for participating in the three required oral examinations is appreciated: Alan J. Grodzinsky, Tarek M. Habashy, Qing Hu, Jin A. Kong, Stephen D. Senturia, David H. Staelin, Fernando L. Teixeira, Cardinal Warde, and Yan Zhang.

To all current and former graduate students that I have met here during our time together in Professor Kong's group, namely Jerome J. Akerson, Chi O. Ao, Benjamin B. Barrowes, Konstantinos Konistis, Christoper D. Moss, Peter Orondo, Joe Pacheco, Sang-Hoon Park, Shih-En Shih, Bae-Ian Wu, and Yan Zhang: Thanks for friendship and fruitful discussions, all the best for you and your families, and good luck with your future studies and professional lives.

The sponsorship of the German Academic Exchange Service that provided partial financial support during the academic year 1997/98 is acknowledged.

I want to thank my parents, Karl-Heinz and Ilse Braunisch, for everything they have done for me throughout my life. My father, an engineer himself, has been an example to me from my childhood on.

I am dedicating this thesis to my wonderful wife, Monica, whose love, passion, and understanding have been the true inspiration for this work. Thank you for everything, especially your patience, and that our dreams and wishes may come true.

Para mi esposa Mónica
con amor y admiración

Contents

List of Figures

List of Tables

Chapter 1

Introduction

Fields and waves emanate from sources producing them and travel through space and time while interacting with generally composite media, giving rise to secondary sources and a complex response of sensors placed in the scene. The thesis presented here investigates various aspects of this phenomenon with an emphasis on specific applications in engineering and physics.

The fundamental concept of wave propagation and scattering is schematically represented by Fig. 1-1. Indicated are the four main themes addressed and the focus of each core chapter. This illustration thus serves as a first graphical outline of the thesis. The following is a concise narrative description.

The first topic in this work deals with a question in computational electrodynamics (Chapter 2): How can we propagate energy to a limited region in space while resembling an unlimited plane wave as closely as possible? A wave that is optimal in a certain least squared error sense is constructed. The key here lies in projecting the requirements of space limitedness and polarization into the class of waves formed as superposition of plane waves. Both exact, Maxwellian and approximate, non-Maxwellian vector fields are considered. The application of this material is in the numerical simulation of the scattering of waves from randomly rough surfaces via a surface integral equation approach, the method of moments.

The larger portion of the next chapter treats a canonical scattering problem in low-frequency electromagnetic induction sensing (Chapter 3). It demonstrates how

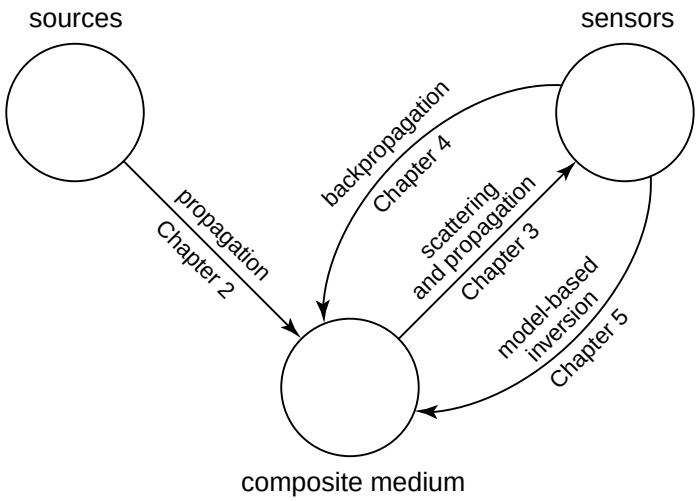

Figure 1-1: The concept of wave propagation and scattering and its relation to the chapters of this thesis.

analytical methods of mathematical physics can lead to useful numerical results. To this end, the method of separation of variables is applied in the prolate spheroidal coordinate system, tailored to the problem of a conducting and permeable prolate spheroid under axial excitation. The enforcement of the boundary conditions on the tangential electric and magnetic fields leads to a marriage of solutions to the Helmholtz and Laplace partial differential equations. In addition to the numerical implementation of the resulting—within the domain of magnetoquasistatics—exact analytical solution, certain approximate approaches are considered. The magnetoquasistatic problem of multiple scattering from clusters of discrete scatterers is also investigated.

The subjects of the two chapters above can be classified as direct or forward problems of wave propagation and scattering. They are complemented with solutions to two inverse problems (note the reversed direction of the corresponding arrows in Fig. 1-1).

The first encompasses a method for numerically reverting the propagation phenomenon in order to "image" the secondary sources (Chapter 4). Backpropagation of

both static and dynamic fields in planar geometries is deconvolution and the method described constitutes a form of physics-based signal processing. It is contrasted with the widely used, and more formal, method of Tikhonov regularization in conjunction with an output least-squares formulation. We discuss a number of applications that fall into the class of problems with additive blurring kernel, identified and analyzed at the beginning of the chapter.

While in source inversion the data depend linearly on the unknowns, the second inverse problem is of nonlinear character (Chapter 5). Here we are aiming at inferring unknown waveguide parameters from guided-wave dispersion data, which calls for a model-based inversion scheme. An important virtue of the inversion methodology developed is the complete elimination of the inner of two nested iterations from the inversion algorithm. The application to the field of acoustics shows the interdisciplinary character of wave propagation and scattering; the methods described in the thesis are not limited to the applications exemplified.

Glancing once again through the above description, a relatively broad and somewhat unconventional view of this thesis in the context of wave propagation and scattering is offered in terms of contrasting concepts or opposites. By no means exhaustive, Table 1.1 summarizes some of the pairs of typical classifiers encountered in the general subject discussed here. Indicated as well are examples of their relation to different parts of this work. This serves as another overview of the thesis and its structure and may help locating its place in the world of fields and waves. The entries in Table 1.1 are ordered, from top to bottom, with increasing disbalance in thesis content. To avoid misunderstandings, this schematic list is not to be considered accurate or exclusive. For example, the scalar approximate 3-D tapered wave given in Section 2.3.1, within a chapter focusing on electromagnetics, has an application in *acoustic* rough surface scattering. Conversely, the application to acoustics in Chapter 5 is motivated by a specific technology (borehole logging for exploration of hydrocarbons) but note the similarity of the structure in Fig. 5-1 with a step-index

Chapter 2, 3	forward	inverse	Chapter 4, 5
Chapter 2	computational	analytical	Chapter 3
Chapter 2	integral	differential	Chapter 3
Chapter 4	linear	nonlinear	Chapter 5
Chapter 4	imaging	parametric inversion	Chapter 5
Chapter 2, 3	exact	approximate	Chapter 2, 3
Chapter 2, 4, 5	dynamic	quasistatic or static	Chapter 3, 4
Chapter 2 to 4	electromagnetics	acoustics	Chapter 5
most of this thesis	theory	experiment	Section 3.3.3
this thesis	deterministic	stochastic	—
this thesis	frequency domain	time domain	—

Table 1.1: Some opposites in wave propagation and scattering and their exemplified association with the contents of this thesis.

optical fiber (along which the propagation of guided waves is also governed by four scalar boundary conditions). The absence of stochastic methods, often associated with the expectation operator E, does not imply that randomness plays no role in the problems considered. In fact, the inverse methods of Chapter 4 and Chapter 5 are tested and evaluated using noisy data, which, of course, is a necessity when dealing with ill-conditioned problems.

Standard methods that are used in or are akin to this dissertation include, e. g., Fourier synthesis and the method of moments for surface integral equations (Chapter 2), the method of separation of variables and asymptotic methods (Chapter 3), regularization, extrapolation, and fast Fourier transformation (Chapter 4), and nonlinear optimization (Chapter 5), to name only a few. Examples of methods in wave propagation and scattering that are not discussed here are volume integral equation methods, the finite-difference time-domain (FDTD) technique, the finite element method, the T-matrix method, and perturbation theory. This does not mean that the latter methods are not important or not applicable to the problems considered in this thesis. For example, the FDTD method is an alternative to the method of moments for the numerical simulation of scattering involving random media.

While in this introduction we have emphasized the interrelation of the four main chapters of the thesis between each other in the general framework of wave propagation and scattering, each of them is self-contained. Each part features an introduction and conclusions of its own. Previous works and relevant existing literature are referenced throughout.

Looking at the chapters individually shows that they aim at very specific and in a narrower sense seemingly unrelated problems. They attempt to make contributions in particular special fields, providing hopefully useful approaches and solutions, and thereby fueling the perpetual expansion of the general arsenal of methods in wave propagation and scattering.

The time convention adopted in the thesis is $\mathrm{e}^{-\mathrm{i}\omega t}$ and this factor is suppressed throughout.

Chapter 2

Tapered waves for the simulation of 3-D rough surface scattering

2.1 Introduction

Recent years have seen major advances in the development of fast method of moments (MoM) solvers for three-dimensional (3-D) scattering of electromagnetic vector waves from rough surfaces [1]–[3], [5]–[10]. Efforts are now also being directed towards inclusion of objects situated in the neighborhood of the rough surface [4], [11]–[15]. Since the problem of scattering from an object next to a rough surface is computationally complex, two-dimensional (2-D) investigations are also popular and of importance [16]–[23]. The 3-D case with or without objects is aimed at by the research presented in this chapter [24]–[26].

The methods employed usually require a truncation of the rough surface because of limited computing resources which leads to erroneous results due to artificial edge diffraction when ideal plane waves are used to excite the system. The tapered wave concept is based on providing an illumination for the numerical simulation that resembles the plane wave case to be modeled closely at the center of the scattering scenario (including a particular arbitrary polarization) while its intensity becomes negligibly

small upon approaching the artificially introduced edges of the rough surface. Thus unwanted edge effects due to the primary incident wave are avoided and the proper normalization of computed scattering coefficients allows a meaningful comparison with the ideal plane wave case; near-field quantities, such as current distributions induced near the center of the tapered wave, are also expected to be similar. Furthermore, the tapered wave should be constructed in such a way that it satisfies the Maxwell equations without any approximation. This helps to increase the confidence in the results obtained from the generally rather complex MoM simulation codes. It should also be possible to substitute it for a plane wave of arbitrary polar and azimuthal angles of incidence without loss of polarization and degradation of tapering. The above requirements lead us to revise and modify the tapered wave found in the open literature.

2.2 Maxwellian 3-D tapered wave optimal in a least squared error sense

2.2.1 Superposition of plane waves

Consider a homogeneous, isotropic medium with real wavenumber k and wave impedance η. Then the following superposition of a 2-D spectrum of plane waves is an exact solution to the Maxwell equations and represents a wave incident upon the x-y plane from $z > 0$:

$$\overline{E}_i(\overline{r}) = \int_{-\infty}^{\infty} \mathrm{d}\overline{k}_\rho \, \mathrm{e}^{\mathrm{i}\,(\overline{k}_\rho \cdot \overline{\rho} - k_z z)} \, \psi(\overline{k}_\rho) \, \overline{e}(\overline{k}_\rho) \tag{2.1}$$

$$\overline{H}_i(\overline{r}) = \int_{-\infty}^{\infty} \mathrm{d}\overline{k}_\rho \, \mathrm{e}^{\mathrm{i}\,(\overline{k}_\rho \cdot \overline{\rho} - k_z z)} \, \frac{\psi(\overline{k}_\rho)}{\eta} \, \overline{h}(\overline{k}_\rho) \tag{2.2}$$

where

$$\overline{r} = \overline{\rho} + \hat{z}\, z \tag{2.3}$$

$$\overline{k}_\rho = \hat{x}\, k_x + \hat{y}\, k_y \tag{2.4}$$

and

$$k_z = k_z(k_\rho) = \begin{cases} \sqrt{k^2 - k_\rho^2} & k_\rho \le k \\ -\mathrm{i}\sqrt{k_\rho^2 - k^2} & k_\rho > k \end{cases} \tag{2.5}$$

with $k_\rho = |\overline{k}_\rho|$.

The spectrum ψ in (2.1), (2.2) carries the information on the shape of the footprint (defined as the distribution of the magnitude in the x-y plane) of the incident field and also on the direction of incidence. It is assumed to be centered about

$$\begin{aligned} \overline{k}_{i\rho} &= \hat{x}\, k_{ix} + \hat{y}\, k_{iy} && (2.6) \\ &= k\, \sin\theta_i\, (\hat{x}\, \cos\phi_i + \hat{y}\, \sin\phi_i) && (2.7) \end{aligned}$$

where θ_i and ϕ_i are the polar and azimuthal angles of incidence of the central plane wave and—*pars pro toto*—of the tapered wave (Fig. 2-1). In an application, the central plane wave, traveling in the direction of $\overline{k}_i$ as indicated in Fig. 2-1(a), would coincide with the plane wave that was replaced by the tapered wave in the numerical simulation. Details about the functional dependence of ψ are given in Section 2.2.2.

The polarization vectors $\overline{e}$ and $\overline{h}$ are of the general form

$$\overline{e}(\overline{k}_\rho) = e_h(\overline{k}_\rho)\, \hat{h}(\overline{k}_\rho) + e_v(\overline{k}_\rho)\, \hat{v}(\overline{k}_\rho) \tag{2.8}$$

and

$$\overline{h}(\overline{k}_\rho) = e_v(\overline{k}_\rho)\, \hat{h}(\overline{k}_\rho) - e_h(\overline{k}_\rho)\, \hat{v}(\overline{k}_\rho) \tag{2.9}$$

The notations

$$\hat{h}(\overline{k}_\rho) = \begin{cases} \hat{x}\, \sin\phi_i - \hat{y}\, \cos\phi_i & k_\rho = 0 \\ \frac{1}{k_\rho}\, (\hat{x}\, k_y - \hat{y}\, k_x) & k_\rho > 0 \end{cases} \tag{2.10}$$

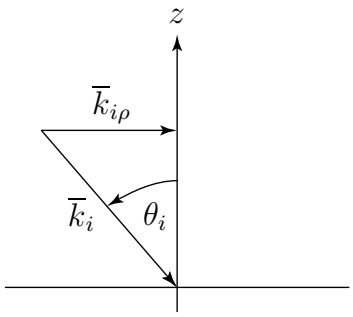

(a) Incident wavevector in 3-D space.

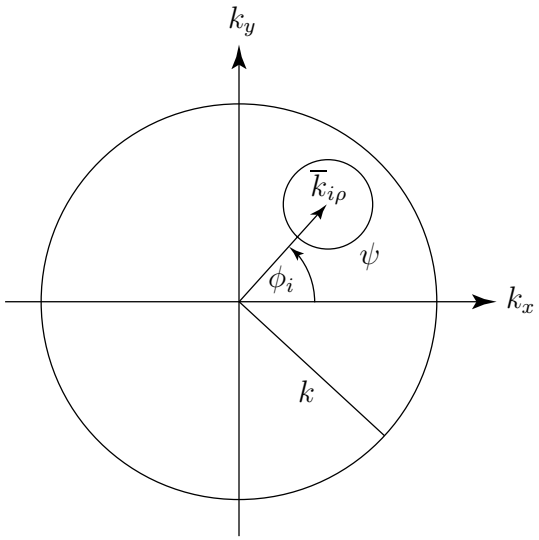

(b) The 2-D wavenumber space.

Figure 2-1: Relation between the incident wavevector $\overline{k}_i$ and the spectrum of plane waves, ψ.

and

$$\hat{v}(\overline{k}_\rho) = \begin{cases} \hat{x}\,\cos\phi_i + \hat{y}\,\sin\phi_i & k_\rho = 0 \\ \frac{k_z}{k\,k_\rho}\,(\hat{x}\,k_x + \hat{y}\,k_y) + \hat{z}\,\frac{k_\rho}{k} & k_\rho > 0 \end{cases} \tag{2.11}$$

are found in similar form in [27, 28]. The chosen definitions for $k_\rho = 0$ take care of the special case of a normally incident pure plane wave. $k_\rho > k$ corresponds to evanescent waves (Section 2.2.2) and, due to (2.5), the horizontal part of $\hat{v}(\overline{k}_\rho)$ is imaginary in this case. It is important to note the discontinuity of $\hat{h}$ and $\hat{v}$ at $\overline{k}_\rho = 0$; both *unit* vectors change sign when crossing the origin along a straight line in the $\overline{k}_\rho$ plane.

The general superposition integrals (2.1), (2.2) were stated similarly in [10, 29]; however, only normal incidence is considered in what follows there. If e_h and e_v in (2.8), (2.9) are set to constants then (2.1), (2.2) specializes to the tapered wave used in [1]–[5], with a particular spectrum ψ briefly discussed in Section 2.2.2. Problems with this tapered wave encountered near the grazing incidence (for discussion and references see Section 2.2.2) and near the normal incidence (Section 2.2.3) motivated our formulation of a different kind of tapered wave, especially with respect to the polarization vectors.

2.2.2 Amplitude spectrum

If the polarization vector $\overline{e}$ on the right-hand side of (2.1) is replaced by a scalar constant e_i, then the resulting integral

$$\mathcal{E}_i(\overline{r}) = e_i \int_{-\infty}^{\infty} \mathrm{d}\overline{k}_\rho\, \mathrm{e}^{\mathrm{i}\,(\overline{k}_\rho\cdot\overline{\rho} - k_z z)}\, \psi(\overline{k}_\rho) \tag{2.12}$$

is the plane-wave representation of a scalar wave satisfying the scalar Helmholtz equation and ψ can be identified with the well-known angular spectrum in scalar diffraction theory [30, 31]. Thus, by obtaining ψ via 2-D Fourier transformation and making sure that $\overline{e}$ and $\overline{h}$ vary only moderately over the spatial frequency range where ψ is not negligible, arbitrary footprints of the vector tapered wave can be

approximated. [The mentioned requirement leads to a problem with the tapering in [1]–[5] near normal incidence (Section 2.2.3).] The information on the direction of incidence of the tapered wave is included by shifting ψ in the k_x-k_y plane to be centered about $\overline{k}_{i\rho}$. The prescribed footprint itself is fixed with respect to angle of incidence.

A Gaussian-shaped footprint (Fig. 2-2) whose amplitude at $\rho = g$ is down to 1/e times the level at the center is implemented by choosing

$$\psi(\overline{k}_\rho) = \frac{g^2}{4\pi}\, \mathrm{e}^{-\frac{g^2}{4}|\overline{k}_\rho - \overline{k}_{i\rho}|^2} \tag{2.13}$$

A pure plane wave is described by

$$\psi(\overline{k}_\rho) = \delta(\overline{k}_\rho - \overline{k}_{i\rho}) \tag{2.14}$$

with δ the Dirac delta function. Equation (2.14) follows from (2.13) as the generalized limit as $g \to \infty$. It should be pointed out that—as is well known from signal theory—among all footprints of given finite energy and width, the Gaussian leads to the smallest bandwidth (for the appropriate definition of space and frequency domain widths) which is desirable for synthesis.

Spectral components with $k_\rho > k$ are the amplitudes of plane waves that travel along the x-y plane and are evanescent for $z > 0$. Their inclusion makes it possible to synthesize a given footprint near or at grazing incidence.

The spectrum in [1]–[5] is given as a 2-D Fourier integral that needs to be evaluated numerically. It cannot be used near grazing incidence where the field distribution in the x-y plane becomes highly oscillatory. Its continued use is rooted in its close relation to a scalar tapered wave employed previously [32, 33]. The latter wave, on the other hand, goes back to a popular incident field introduced by E. I. Thorsos [34] who—for the 2-D case—derived it as an approximation to a summation of plane waves, accurate for sufficiently *small* angles of incidence θ_i (also employed in [18],

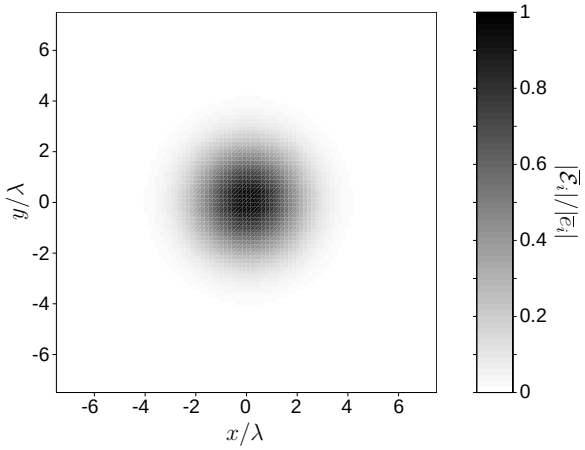

Figure 2-2: Example of a prescribed Gaussian-shaped footprint to be approximated by the vector tapered wave ($g = 2\,\lambda$).

[35]–[39].) The limitations of the 2-D scalar Thorsos wave at low grazing angles were analyzed and discussed in [40, 41]. The bound in the resolvability criterion discussed by Ngo and Rino [42] also becomes significant at low grazing angles.

The recommendation for the 3-D vector case is to start over and simply use the spectrum given by (2.13) which has the additional benefit of being given in closed form. Taking advantage of the functional dependence of the Gaussian spectrum, an option in the 2-D case is to use path deformation techniques to speed up the evaluation of the exact expression for the incident field [43]. In the 3-D case we can at least band-limit the integration to a disk about $\overline{k}_\rho = \overline{k}_{i\rho}$ within which the spectrum exhibits a significant magnitude (disk radius a few multiples of $2/g$). This leads to an approximation of the original incident field which satisfies Maxwell's equations exactly. The derivation of approximate non-Maxwellian 3-D tapered waves which can be evaluated without integration is discussed in Section 2.3.

2.2.3 Polarization

In order to construct a wave that is both reliably tapered and clearly polarized, for all angles of incidence, we suggest choosing the polarization of the individual plane wave components as follows:

$$e_h(\overline{k}_\rho) = \overline{e}_i \cdot \hat{h}(\overline{k}_\rho) \tag{2.15}$$

$$e_v(\overline{k}_\rho) = \overline{e}_i \cdot \hat{v}(\overline{k}_\rho) \tag{2.16}$$

with the polarization vector of the central plane wave

$$\overline{e}_i = \overline{e}(\overline{k}_{i\rho}) = E_h\, \hat{h}(\overline{k}_{i\rho}) + E_v\, \hat{v}(\overline{k}_{i\rho}) \tag{2.17}$$

Hence, in dyadic notation

$$\overline{e}(\overline{k}_\rho) = \overline{e}_i \cdot \left[\hat{h}(\overline{k}_\rho)\, \hat{h}(\overline{k}_\rho) + \hat{v}(\overline{k}_\rho)\, \hat{v}(\overline{k}_\rho)\right] \tag{2.18}$$

and

$$\overline{h}(\overline{k}_\rho) = \overline{e}_i \cdot \left[\hat{v}(\overline{k}_\rho)\, \hat{h}(\overline{k}_\rho) - \hat{h}(\overline{k}_\rho)\, \hat{v}(\overline{k}_\rho)\right] \tag{2.19}$$

The dominant polarization state of the tapered wave is then determined by the choice of E_h and E_v in (2.17) which describe the (generally elliptical) polarization of the central plane wave.

Note that with this choice the integrands of (2.1), (2.2) are continuous at $\overline{k}_\rho = 0$ [as follows from Section 2.3, we have in fact analyticity throughout the k_x-k_y plane excluding the circle $|\overline{k}_\rho| = k$ provided an analytic spectrum such as (2.13) is used; at $|\overline{k}_\rho| = k$ the integrands are still continuous] as opposed to the tapered wave in [1]–[5]. The latter wave is characterized by the choices

$$e_h(\overline{k}_\rho) = E_h \tag{2.20}$$

$$e_v(\overline{k}_\rho) = E_v \tag{2.21}$$

leading to rapidly varying polarization vectors $\overline{e}$ and $\overline{h}$ near $\overline{k}_\rho = 0$. For the near normal incidence case this will violate the basic assumption of the footprint design technique described in Section 2.2.2. When examined numerically it is found that the approximation of a prescribed, e. g., Gaussian, footprint is poor; the result for normal incidence shows the largest intensity along a ring in the x-y plane rather than at the center (Fig. 2-3). This effect is also evident from the following consideration. For a spectrum that satisfies

$$\psi(\overline{k}_\rho) = \psi(-\overline{k}_\rho) \tag{2.22}$$

it can be shown that, for $E_v = 0$, we have

$$\overline{E}_i(\overline{\rho}, z) = -\overline{E}_i(-\overline{\rho}, z) \tag{2.23}$$

with the consequence

$$\overline{E}_i(\overline{\rho} = 0, z) = 0 \tag{2.24}$$

for all z [Fig. 2-3(a)]. Similarly, for $E_h = 0$ it is found that

$$\hat{z} \times \overline{E}_i(\overline{\rho}, z) = -\hat{z} \times \overline{E}_i(-\overline{\rho}, z) \tag{2.25}$$

and [Fig. 2-3(b)]

$$\hat{z} \times \overline{E}_i(\overline{\rho} = 0, z) = 0 \tag{2.26}$$

Other problems are leakage of the intensity to larger radii than expected (Fig. 2-3) and the non-existence of a clear polarization of the wave. By using (2.18), (2.19) these problems are removed (Fig. 2-4). [The 101×101 tapered wave field values for the results in Fig. 2-3, 2-4, 2-7, and 2-8 were calculated using a summation of 128×128 plane waves with a 2-D DFT sampling of the $\overline{k}_\rho$ space. The spectrum after [1]–[5] was calculated using a 2-D FFT algorithm. The horizontal periodicity of the fields

in the space domain was in all cases $30\,\lambda$, i. e., twice the surface length shown in the figures, in order to avoid aliasing (Section 2.2.4).]

Least squared error property

The tapered wave with polarization vectors (2.18), (2.19) is optimal in a least squared error sense. Consider a vector field

$$\overline{\mathcal{E}}_i(\overline{r}) = \overline{e}_i \int_{-\infty}^{\infty} \mathrm{d}\overline{k}_\rho \, \mathrm{e}^{\,\mathrm{i}\,(\overline{k}_\rho \cdot \overline{\rho} - k_z z)} \, \psi(\overline{k}_\rho) \tag{2.27}$$

obtained by multiplying a scalar tapered wave with the constant polarization vector $\overline{e}_i$ as in (2.17). This field combines the desirable properties of well-defined polarization and controllable tapering. [Note that $|\overline{\mathcal{E}}_i(\overline{\rho}, z=0)|/|\overline{e}_i|$ corresponds to the prescribed footprint as discussed in Section 2.2.2 and illustrated in Fig. 2-2.] However, the field defined by (2.27) is not a valid electric field because in general

$$\nabla \cdot \overline{\mathcal{E}}_i(\overline{r}) \neq 0 \tag{2.28}$$

We can therefore ask for a permissible wave of form (2.1) with the same spectrum ψ that approximates $\overline{\mathcal{E}}_i$ as close as possible. Defining

$$S(z) = \int_{-\infty}^{\infty} \mathrm{d}\overline{\rho} \, \left| \overline{E}_i(\overline{\rho}, z) - \overline{\mathcal{E}}_i(\overline{\rho}, z) \right|^2 \tag{2.29}$$

we find from Parseval's theorem for 2-D Fourier transforms

$$S(z) = 4\pi^2 \int_{-\infty}^{\infty} \mathrm{d}\overline{k}_\rho \left| \mathrm{e}^{-\mathrm{i}\,k_z z} \, \psi(\overline{k}_\rho) \right|^2 \left| \overline{e}(\overline{k}_\rho) - \overline{e}_i \right|^2 \tag{2.30}$$

To minimize S for all z note that

$$\left| \overline{e}(\overline{k}_\rho) - \overline{e}_i \right|^2 = \left| \overline{e}(\overline{k}_\rho) - \overline{e}_i \cdot \left[\hat{h}(\overline{k}_\rho)\, \hat{h}(\overline{k}_\rho) + \hat{v}(\overline{k}_\rho)\, \hat{v}(\overline{k}_\rho) \right] \right|^2 + \left| \overline{e}_i \cdot \hat{k}(\overline{k}_\rho) \right|^2 \tag{2.31}$$

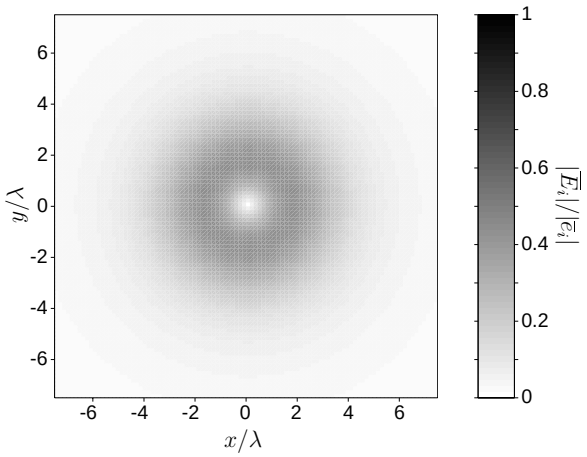

(a) Horizontally polarized plane wave components.

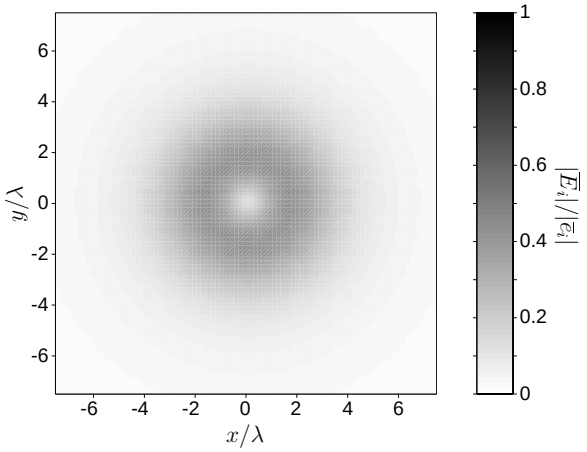

(b) Vertically polarized plane wave components.

Figure 2-3: Resulting footprints at normal incidence for the tapered wave after [1]–[5]. The approximation of the prescribed footprint (Fig. 2-2) is not satisfactory.

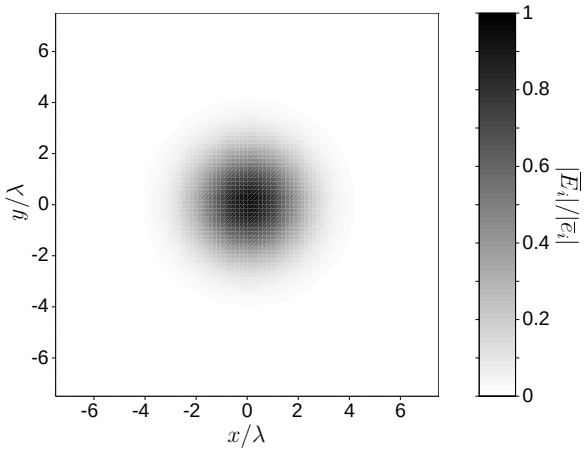

(a) Horizontal polarization.

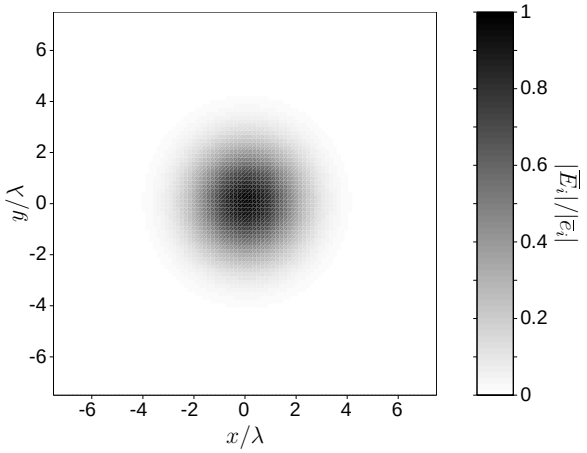

(b) Vertical polarization.

Figure 2-4: Resulting footprints at normal incidence for the tapered wave introduced in the present work and approximating the prescribed footprint of Fig. 2-2.

where

$$\hat{k}(\overline{k}_\rho) = \hat{v}(\overline{k}_\rho) \times \hat{h}(\overline{k}_\rho) = \frac{1}{k}\,(\hat{x}\,k_x + \hat{y}\,k_y - \hat{z}\,k_z) \tag{2.32}$$

Hence, (2.18) yields the optimal $\overline{E}_i$ and the minimum S_m is given by

$$S_m(z) = 4\pi^2 \int\limits_{-\infty}^{\infty} \mathrm{d}\overline{k}_\rho \left|\mathrm{e}^{-\mathrm{i}\,k_z z}\,\psi(\overline{k}_\rho)\right|^2 \left|\overline{e}_i \cdot \hat{k}(\overline{k}_\rho)\right|^2 \tag{2.33}$$

It is emphasized that we refer to $S(z)$ and $S_m(z)$ as "errors" only in the familiar mathematical sense. The purpose of comparing with the non-Maxwellian field $\overline{\mathcal{E}}_i(\overline{r})$ is to uniquely identify a functional dependence of $\overline{e}(\overline{k}_\rho)$ which can be expected to guarantee tapering and a dominant polarization state of the total field (both as prescribed). In other words, $\overline{\mathcal{E}}_i(\overline{r})$ which is ideal with respect to tapering and polarization is projected into the space of waves constructed as 2-D superpositions of plane waves, lending its desirable properties to an exact solution of Maxwell's equations.

To illustrate the approximation behavior numerically we computed the relative root mean squared (RMS) error

$$\sqrt{S(0) \Big/ \int\limits_{-\infty}^{\infty} \mathrm{d}\overline{\rho}\,\left|\overline{\mathcal{E}}_i(\overline{\rho}, 0)\right|^2} = \frac{\sqrt{2\,S(0)/\pi}}{g\,|\overline{e}_i|} \tag{2.34}$$

where $\overline{\mathcal{E}}_i$ is formed using the spectrum (2.13), for varying tapering parameter g and incidence angle θ_i (in Fig. 2-5 and 2-6 contour levels decrease monotonically for fixed θ_i and increasing g and are separated by 2 dB steps.) The results in Fig. 2-5 for the tapered wave in [1]–[5] exhibit the previously mentioned problems near normal and grazing incidence. It is noted that for intermediate angles θ_i and larger g the error can be smaller than 1% (-20 dB) and that the approximation behavior for horizontally polarized [Fig. 2-5(a)] and vertically polarized [Fig. 2-5(b)] plane wave components is similar. For the tapered wave composed according to (2.18) and (2.13) and for horizontal polarization [Fig. 2-6(a)] the error is small everywhere and practically in-

dependent of θ_i. For vertical polarization [Fig. 2-6(b)] the error grows larger towards grazing but does not exceed moderate levels. The fact that approximating a vertically polarized plane wave near grazing incidence is harder can be understood intuitively by noting that the energy flow of the tapered wave has to "bend down" in order to form the exponentially space-limited footprint, a requirement in apparent contradiction with maintaining a vertical polarization state. However, Fig. 2-6(b) shows that the optimal approximation finds a reasonable compromise. [For the results shown in Fig. 2-5 and 2-6 the RMS error was evaluated using a Gauss-Legendre quadrature over a surface of size $7\,g \times 7\,g$, choosing in both dimensions 5 times the number of sampling points obtained when rounding $7\,g/\lambda$ to the nearest integer. 128×128 plane waves were summed to space domain fields with horizontal periodicity of $7\,g$. The tapering parameter g was changed in steps of $\lambda/2$ and the angle of incidence θ_i in steps of 5^{o}.]

Another important property of the wave based on (2.18) is found from (2.19) by noting that

$$\overline{e}_i \cdot \overline{h}(\overline{k}_\rho) = \overline{h}(\overline{k}_\rho) \cdot \overline{e}_i = \overline{e}_i \cdot \left[\hat{v}(\overline{k}_\rho)\,\hat{h}(\overline{k}_\rho) - \hat{h}(\overline{k}_\rho)\,\hat{v}(\overline{k}_\rho)\right] \cdot \overline{e}_i = 0 \tag{2.35}$$

and thus, according to (2.2),

$$\overline{e}_i \cdot \overline{H}_i(\overline{r}) = 0 \tag{2.36}$$

The total magnetic field of the tapered wave is everywhere perpendicular to the electric field of the central plane wave.

The fact (2.36) is reminiscent of the tapered wave (given for the case of normal incidence only) in [29], designed to have no y component of the magnetic field. Setting

$$\overline{e}_i = -\hat{y} \tag{2.37}$$

in (2.18), (2.19) or, more conveniently, in (2.49), (2.53) of Section 2.3 and comparing

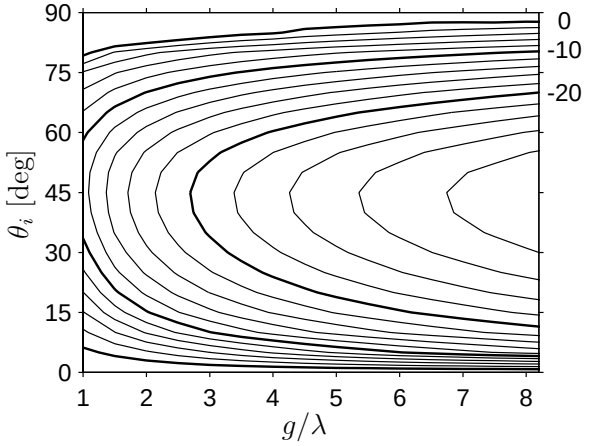

(a) Horizontally polarized components.

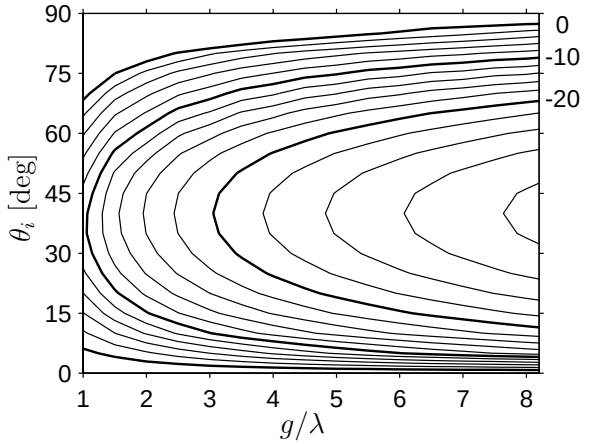

(b) Vertically polarized components.

Figure 2-5: Relative RMS error [dB] at $z = 0$ for the tapered wave after [1]–[5] as compared to a non-Maxwellian field with prescribed tapering and polarization.

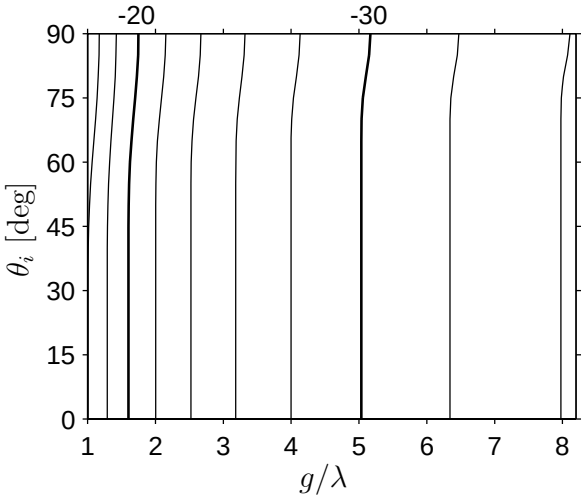

(a) Horizontal polarization.

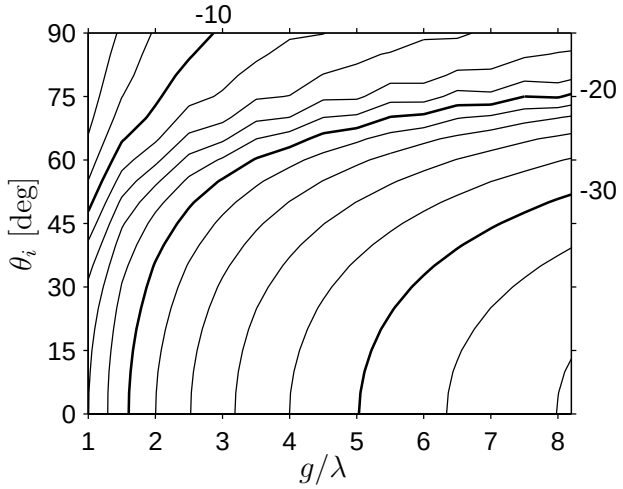

(b) Vertical polarization.

Figure 2-6: Relative RMS error [dB] at $z = 0$ for the tapered wave introduced in this thesis.

to (7), (8) in [29] it is found that the waves are different. In particular, the polarization vectors in [29] are unbounded as $|\overline{k}_\rho| \to k$ while being analytic throughout the k_x-k_y plane excluding the circle $|\overline{k}_\rho| = k$.

The tapered wave given previously by Tran and Maradudin [44] and for the case of vertical polarization employed in [7]–[9], when generalized to arbitrary azimuthal angle of incidence and cast into our formalism, turns out to be somewhat related. Their magnetic polarization vector for horizontal polarization is collinear to (2.19) when $E_v = 0$. However, it is normalized to unit length and the magnetic polarization vector for vertical polarization is then obtained by taking the vector product with $\hat{k}(\overline{k}_\rho)$. It is seen that this construction will not lead to an optimal approximation of (2.27) and thus to a different wave.

Finally, we point out that our tapered wave has been derived by optimizing the electric field with respect to an ideal field $\overline{\mathcal{E}}_i$. The magnetic field of the tapered wave then followed from the familiar relation between the electric and magnetic field of a plane wave (Faraday's law). It is clear that in a similar manner we could derive a dual tapered wave which is obtained by choosing the magnetic polarization vectors $\overline{h}$ with respect to a non-Maxwellian field $\overline{\mathcal{H}}_i$ and applying Ampere's law to find the electric field.

2.2.4 Issues in the application to 3-D scattering

The tapered wave introduced in this thesis can be used for the simulation of scattering from randomly rough surfaces with a planar mean surface. In a more complex scenario, objects are embedded in a layered background with rough interfaces. If the objects are at least partially situated in the half space where the sources of the incident wave reside, it is important also to pay attention to the distribution of the tapered wave for $z > 0$.

Fig. 2-7 and 2-8 illustrate the cases of oblique and grazing incidence, respectively. Fig. 2-7(a) shows how the tapered wave forms a slightly converging beam, approxi-

mating the prescribed footprint at $z = 0$ [Fig. 2-7(b)]. The non-zero intensity in the top-right corner of Fig. 2-7(a) is due to the periodic nature of the discretized versions of (2.1), (2.2) with respect to $\overline{\rho}$. This aliasing effect, which in the present case would have no effect on the illumination of objects situated relatively close to the surface at $z = 0$, can be reduced—as usual—by sampling finer with respect to $\overline{k}_\rho$. For footprints where $\psi(\overline{k}_\rho)$ is not given in closed form as in (2.13) but is computed by 2-D FFT this is achieved by applying zero padding before carrying out the transformation. The remarkable fact about Fig. 2-8 is that the inclusion and correct treatment of evanescent waves enables synthesis of the prescribed footprint even for $\theta_i = 90^\mathrm{o}$ [Fig. 2-8(b)]. Aliasing for $z > 0$ in this case is more severe [Fig. 2-8(a)].

In typical applications of the tapered wave concept, electromagnetic wave scattering from a conducting object over a conducting rough surface is simulated and Glisson's overlapping triangular flat vector basis functions [45]–[47] for the electric surface current on both object and rough surface are used in discretizing the electric field integral equation, applying a Galerkin-type method of moments. We compared the results of such a scattering code with those obtained by the hybrid method described in [11]–[15]. The major advantage of this hybrid method is that the decomposition into flat surface problems with impressed equivalent sources that are determined by lower order solutions allows introduction of the tensor Green function for layered media. This removes the need to solve for the surface currents on the rough surface and to truncate its physical dimensions. In the comparison, the same rough surface profile, the same patch model for the object, and the same tapered incident wave were used for solving the problem with the two independent codes; reasonable agreement was obtained. Discrepancies, however, occurred for near-grazing angles $\theta_i = 80 \ldots 90^\mathrm{o}$ where the pure MoM results suffer from edge effects due to the truncation of the rough surface. While the incident wave can be tapered to fall off exponentially towards the edges the scattered fields from the object decay only as $1/r$, giving rise to problems at very large polar angles where the object acts as a reflector that directs energy

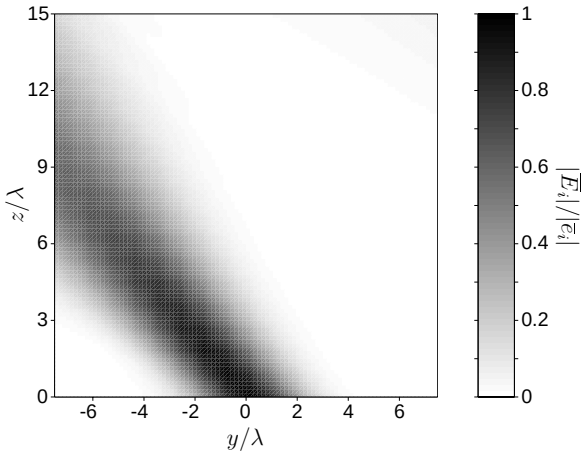

(a) Side view ($x = 0$).

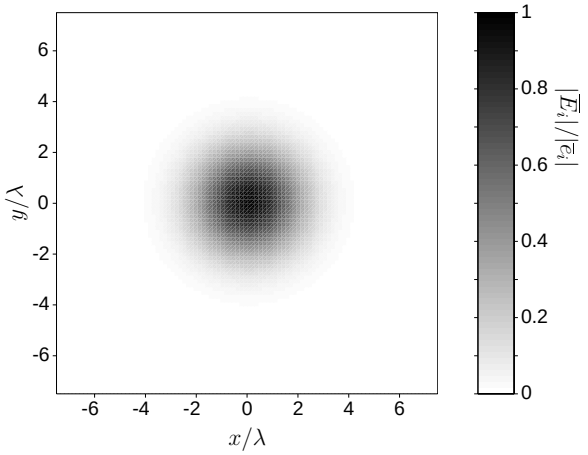

(b) Footprint.

Figure 2-7: Beam formation of the tapered wave at oblique incidence ($\theta_i = 40^{\text{o}}$, $\phi_i = 90^{\text{o}}$, $g = 2\,\lambda$, horizontal polarization).

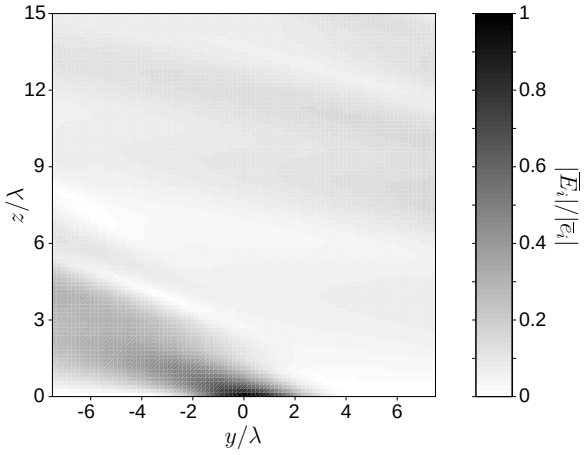

(a) Side view ($x = 0$).

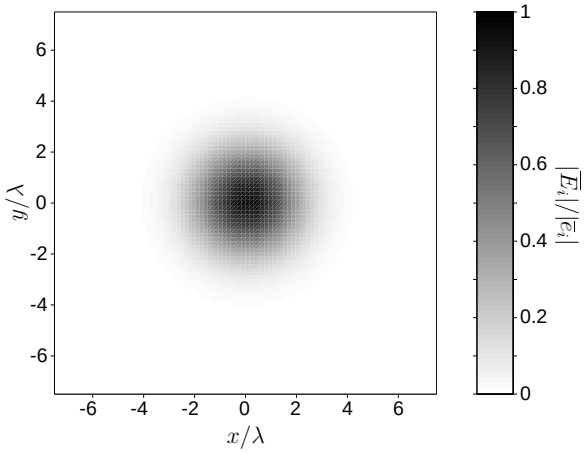

(b) Footprint.

Figure 2-8: Beam formation of the tapered wave at grazing incidence ($\theta_i = \phi_i = 90^{\text{o}}$, $g = 2\,\lambda$, horizontal polarization).

towards the edges. This indicates the increased difficulty of the low grazing angle rough surface scattering problem when an object is present. In the hybrid method, the correct behavior of the monostatic HH return is guaranteed at $\theta_i = 90^o$, where in the flat surface case the boundary condition on the perfectly conducting surface forces a zero. It should be remarked that, although the utilization of the tapered wave concept for the method in [11]–[15], which when implemented up to and including the first order can yield accurate results for slightly rough surfaces, is not imperative, it may still be useful there because only finite rough surface profiles can be processed.

2.3 Approximate 3-D tapered waves

A clear advantage of the original 2-D scalar Thorsos wave and a major reason for its popularity is the avoidance of numerical integrations in the evaluation of the incident field. The price paid is the non-Maxwellian nature of the approximation which, as reported in [40], can lead to anomalies in the computed results of simulations that require evaluation of the incident field not only on the rough surface as, e. g., in object-surface interaction problems. Also the breakdown of the approximation near grazing incidence causes serious problems in some applications. Keeping these limitations in mind and akin to the derivation of the Thorsos wave, in the 3-D case with the spectrum (2.13) we can argue, in a spirit similar to Laplace's method for the asymptotic expansion of integrals [48, 49], that for large g the main contribution to the superposition of plane waves comes from around $\overline{k}_\rho = \overline{k}_{i\rho}$ [Fig. 2-1(b)].

2.3.1 Scalar wave case

Using the truncated bivariate Taylor expansion in k_x, k_y

$$\sqrt{k^2 - \left|\overline{k}_{i\rho} + \overline{k}_\rho\right|^2} \;\approx\; k_{iz} - \frac{k_{ix}}{k_{iz}}\,k_x - \frac{k_{iy}}{k_{iz}}\,k_y$$

$$- \frac{k_{ix}\, k_{iy}}{k_{iz}^3}\, k_x\, k_y - \frac{k^2 - k_{iy}^2}{2\, k_{iz}^3}\, k_x^2 - \frac{k^2 - k_{ix}^2}{2\, k_{iz}^3}\, k_y^2 \qquad (2.38)$$

where

$$k_{iz} = k\, \cos\theta_i \qquad (2.39)$$

we can obtain from (2.12) by carrying out the integrations and symmetrizing the result with respect to x and y (without any further approximations)

$$\mathcal{E}_i(\overline{r}) \approx e_i\, \mathrm{e}^{\mathrm{i}\, \overline{k}_i \cdot \overline{r}}\, \frac{1}{u(z)}\, \exp\left[-\frac{s(\overline{r})}{g^2\, u^2(z)} \right] \qquad (2.40)$$

where

$$\overline{k}_i = \overline{k}_{i\rho} - \hat{z}\, k_{iz} \qquad (2.41)$$

and

$$\begin{aligned} s(\overline{r}) \;=\; & \left(1 - \frac{2\mathrm{i}}{g^2}\, \frac{k^2 - k_{ix}^2}{k_{iz}^3}\, z \right) \left(x + \frac{k_{ix}}{k_{iz}}\, z \right)^2 \\ & + \left(1 - \frac{2\mathrm{i}}{g^2}\, \frac{k^2 - k_{iy}^2}{k_{iz}^3}\, z \right) \left(y + \frac{k_{iy}}{k_{iz}}\, z \right)^2 \\ & + \frac{4\mathrm{i}}{g^2}\, \frac{k_{ix}\, k_{iy}}{k_{iz}^3}\, z \left(x + \frac{k_{ix}}{k_{iz}}\, z \right) \left(y + \frac{k_{iy}}{k_{iz}}\, z \right) \end{aligned} \qquad (2.42)$$

and

$$u(z) = \sqrt{\left(1 - \frac{2\mathrm{i}}{g^2}\, \frac{k^2}{k_{iz}^3}\, z \right) \left(1 - \frac{2\mathrm{i}}{g^2}\, \frac{1}{k_{iz}}\, z \right)} \qquad (2.43)$$

In deriving (2.38)–(2.43), the dispersion relation

$$k_{iz}^2 = k^2 - k_{ix}^2 - k_{iy}^2 \qquad (2.44)$$

has been used. As expected, (2.40) coincides with (2.12) exactly when $z = 0$. As $g \to \infty$ the plane wave case is recovered. It is remarked that (2.40) is not a direct generalization of the Thorsos wave to 3-D because of the different formulation of the

superposition integral used as starting point. However, using the following argument we arrive at a condition for the validity of (2.40) that is similar to the one given in the 2-D case [40]–[42], in particular the dependence on $(\frac{\pi}{2} - \theta_i)^2$ near grazing carries over to 3-D: The radius of convergence of the full Taylor series (2.38) is limited to $k - k_{i\rho}$ because of the branch point of the square root function encountered for $k_\rho = k$ [Fig. 2-1(b)]. Thus

$$kg\,(1 - \sin\theta_i) \gg 1 \tag{2.45}$$

is required for (2.40) to be an accurate representation of (2.12). In addition, the error of the truncated series (2.38) is multiplied by z with the consequence that the largest $|z|$ considered should be small relative to g, i. e.,

$$g \gg |z|_{\max} \tag{2.46}$$

2.3.2 Vector wave case

Approximations for the 3-D vector wave case are derived in a similar fashion by additionally expanding the polarization vectors. Substituting

$$\hat{h}(\overline{k}_\rho)\,\hat{h}(\overline{k}_\rho) = \frac{1}{k_\rho^2}\left[\hat{x}\,\hat{x}\,k_y^2 - (\hat{x}\,\hat{y} + \hat{y}\,\hat{x})\,k_x\,k_y + \hat{y}\,\hat{y}\,k_x^2\right] \tag{2.47}$$

$$\begin{aligned}\hat{v}(\overline{k}_\rho)\,\hat{v}(\overline{k}_\rho) &= \frac{k_z^2}{k^2\,k_\rho^2}\left[\hat{x}\,\hat{x}\,k_x^2 + (\hat{x}\,\hat{y} + \hat{y}\,\hat{x})\,k_x\,k_y + \hat{y}\,\hat{y}\,k_y^2\right] \\ &\quad + \frac{k_z}{k^2}\left[(\hat{x}\,\hat{z} + \hat{z}\,\hat{x})\,k_x + (\hat{y}\,\hat{z} + \hat{z}\,\hat{y})\,k_y\right] + \hat{z}\,\hat{z}\,\frac{k_\rho^2}{k^2}\end{aligned} \tag{2.48}$$

into (2.18), we find

$$\begin{aligned}\overline{e}(\overline{k}_\rho) &= \frac{\overline{e}_i}{k^2}\cdot\Big[\hat{x}\,\hat{x}\,(k^2 - k_x^2) + \hat{y}\,\hat{y}\,(k^2 - k_y^2) + \hat{z}\,\hat{z}\,k_\rho^2 \\ &\quad - (\hat{x}\,\hat{y} + \hat{y}\,\hat{x})\,k_x\,k_y + (\hat{x}\,\hat{z} + \hat{z}\,\hat{x})\,k_x\,k_z + (\hat{y}\,\hat{z} + \hat{z}\,\hat{y})\,k_y\,k_z\Big]\end{aligned} \tag{2.49}$$

Equation (2.49) also follows from

$$\hat{h}\,\hat{h} + \hat{v}\,\hat{v} = \overline{\overline{I}} - \hat{k}\,\hat{k} \tag{2.50}$$

with $\overline{\overline{I}}$ the identity tensor and $\hat{k}$ as in (2.32). Similarly, with the dyads

$$\begin{aligned}
\hat{v}(\overline{k}_\rho)\,\hat{h}(\overline{k}_\rho) &= \frac{k_z}{k\,k_\rho^2}\left[(\hat{x}\,\hat{x} - \hat{y}\,\hat{y})\,k_x\,k_y - \hat{x}\,\hat{y}\,k_x^2 + \hat{y}\,\hat{x}\,k_y^2\right] \\
&\quad + \frac{1}{k}\,(\hat{z}\,\hat{x}\,k_y - \hat{z}\,\hat{y}\,k_x) \qquad (2.51)\\
\hat{h}(\overline{k}_\rho)\,\hat{v}(\overline{k}_\rho) &= \frac{k_z}{k\,k_\rho^2}\left[(\hat{x}\,\hat{x} - \hat{y}\,\hat{y})\,k_x\,k_y + \hat{x}\,\hat{y}\,k_y^2 - \hat{y}\,\hat{x}\,k_x^2\right] \\
&\quad + \frac{1}{k}\,(\hat{x}\,\hat{z}\,k_y - \hat{y}\,\hat{z}\,k_x) \qquad (2.52)
\end{aligned}$$

we obtain from (2.19)

$$\overline{h}(\overline{k}_\rho) = -\frac{\overline{e}_i}{k}\cdot[(\hat{x}\,\hat{y} - \hat{y}\,\hat{x})\,k_z + (\hat{x}\,\hat{z} - \hat{z}\,\hat{x})\,k_y - (\hat{y}\,\hat{z} - \hat{z}\,\hat{y})\,k_x] \tag{2.53}$$

It is observed from (2.49), (2.53) that the tensors in (2.18), (2.19) are symmetric and anti-symmetric, respectively. More importantly here, it is evident from (2.49), (2.53) that both $\overline{e}(\overline{k}_\rho)$ and $\overline{h}(\overline{k}_\rho)$, viewed as functions of the two real variables k_x and k_y, are analytic throughout the k_x-k_y plane excluding the one-dimensional set of points forming the circle $|\overline{k}_\rho| = k$. (It is emphasized that the region of analyticity includes $\overline{k}_\rho = 0$, c. f., Section 2.2.3.) Thus, the Taylor series

$$\overline{e}(\overline{k}_{i\rho} + \overline{k}_\rho) = \sum_{m,n=0}^{\infty} \overline{a}_{mn}\,k_x^m\,k_y^n \tag{2.54}$$

where

$$\overline{a}_{mn} = \frac{1}{m!\,n!}\left[\frac{\partial^{m+n}}{\partial k_x^m\,\partial k_y^n}\,\overline{e}(\overline{k}_\rho)\right]_{\overline{k}_\rho = \overline{k}_{i\rho}} \tag{2.55}$$

converges in the disk

$$|\overline{k}_\rho| < k - k_{i\rho} \tag{2.56}$$

and similar expressions hold for $\overline{h}(\overline{k}_\rho)$. Applying the approximation (2.38) to (2.1) with the spectrum (2.13), inserting (2.54), and using twice the Fourier integral identity (as follows from 3.958.2 in [50])

$$\begin{aligned}\int\limits_{-\infty}^{\infty} \mathrm{d}x\, x^n \mathrm{e}^{\mathrm{i}qx-ax^2} &= \sqrt{\frac{\pi}{a}}\,\mathrm{i}^{-n}\,\frac{\mathrm{d}^n}{\mathrm{d}q^n}\,\mathrm{e}^{-\frac{q^2}{4a}} \\ &= \sqrt{\frac{\pi}{a}}\,n!\left(\frac{\mathrm{i}}{2a}\right)^n \mathrm{e}^{-\frac{q^2}{4a}} \sum_{m=0}^{[n/2]} \frac{(-a)^m}{(n-2m)!\,m!}\,q^{n-2m} \end{aligned} \tag{2.57}$$

where $[n/2]$ is the integral part of $n/2$, leads, again without further approximation, to an expression of the form

$$\overline{E}_i(\overline{r}) \approx \mathrm{e}^{\mathrm{i}\,\overline{k}_i\cdot\overline{r}}\,\frac{1}{u(z)}\,\exp\left[-\frac{s(\overline{r})}{g^2\,u^2(z)}\right]\sum_{m,n=0}^{\infty}\overline{a}_{mn}\,p_{mn}(\overline{r}) \tag{2.58}$$

where $s(\overline{r})$ and $u(z)$ are as in (2.42), (2.43), the $\overline{a}_{mn}$ are obtained from (2.49), and $p_{mn}(\overline{r})$ is polynomial in x, y, z up to z-dependent correction factors that, similar to (2.43), are unity for $z = 0$ or $g \to \infty$. Note that by dropping the summation in (2.58) the scalar wave (2.40) is formally recovered. It is remarked that, different from the scalar case, (2.58) for $z = 0$ is only an approximation of the superposition of plane waves that we started out with because of the finite radius of convergence of (2.54) and the fact that the spectrum (2.13) is not band-limited. The conditions on g for (2.58) to be a reasonable approximation are as stated above for the scalar case. We have

$$\overline{a}_{00} = \overline{e}_i \tag{2.59}$$

and

$$p_{00} = 1 \tag{2.60}$$

Thus the lowest-order electric field approximation following from (2.58) is the same as what is obtained by approximating k_z in (2.27) with the help of (2.38) or multiplying (2.40) by $\overline{e}_i/e_i$. The p_{mn} of higher order vanish as $g \to \infty$. The algebraic details for

the p_{mn} of any order (integrating over k_y first) are as follows:

$$\begin{aligned} p_{mn}(\overline{r}) &= n! \left[\frac{2\mathrm{i}}{g^2\, u_1^2(z)}\right]^n \sum_{k=0}^{[n/2]} \frac{\left[-g^2\, u_1^2(z)\right]^k}{4^k\, k!} \\ &\times \sum_{j=0}^{n-2k} \frac{(m+j)!}{j!\,(n-2k-j)!} \left(y + \frac{k_{iy}}{k_{iz}}\, z\right)^{n-2k-j} \left(\frac{k_{ix}\, k_{iy}}{k_{iz}^3}\, z\right)^j \left[\frac{2\mathrm{i}}{g^2\, u_2^2(z)}\right]^{m+j} \\ &\times \sum_{\ell=0}^{\left[\frac{m+j}{2}\right]} \frac{\left[-g^2\, u_2^2(z)\right]^\ell}{4^\ell\,(m+j-2\ell)!\,\ell!} \left[x + \frac{k_{ix}}{k_{iz}}\, z + w(y,z)\right]^{m+j-2\ell} \end{aligned} \tag{2.61}$$

where

$$u_1^2(z) = 1 - \frac{2\mathrm{i}}{g^2}\, \frac{k^2 - k_{ix}^2}{k_{iz}^3}\, z \tag{2.62}$$

$$u_2^2(z) = \frac{u^2(z)}{u_1^2(z)} \tag{2.63}$$

$$w(y,z) = \frac{2\mathrm{i}}{g^2\, u_1^2(z)}\, \frac{k_{ix} k_{iy}}{k_{iz}^3}\, z \left(y + \frac{k_{iy}}{k_{iz}}\, z\right) \tag{2.64}$$

When choosing the number of terms to be included in (2.58) one should be aware of the limited radius of convergence of (2.54) and the underlying approximation (2.38) which, however, has no effect for $z = 0$. The $\overline{a}_{mn}$ with $m + n < 3$ are given by

$$\overline{a}_{00} = \overline{e}_i \tag{2.65}$$

$$\begin{aligned} \overline{a}_{10} &= \frac{\overline{e}_i}{k^2\, k_{iz}} \cdot \Big[-2\,(\hat{x}\,\hat{x} - \hat{z}\,\hat{z})\, k_{ix}\, k_{iz} - (\hat{x}\,\hat{y} + \hat{y}\,\hat{x})\, k_{iy}\, k_{iz} \\ &\quad + (\hat{x}\,\hat{z} + \hat{z}\,\hat{x})\,(k_{iz}^2 - k_{ix}^2) - (\hat{y}\,\hat{z} + \hat{z}\,\hat{y})\, k_{ix}\, k_{iy} \Big] \end{aligned} \tag{2.66}$$

$$\begin{aligned} \overline{a}_{01} &= \frac{\overline{e}_i}{k^2\, k_{iz}} \cdot \Big[-2\,(\hat{y}\,\hat{y} - \hat{z}\,\hat{z})\, k_{iy}\, k_{iz} - (\hat{x}\,\hat{y} + \hat{y}\,\hat{x})\, k_{ix}\, k_{iz} \\ &\quad - (\hat{x}\,\hat{z} + \hat{z}\,\hat{x})\, k_{ix}\, k_{iy} + (\hat{y}\,\hat{z} + \hat{z}\,\hat{y})\,(k_{iz}^2 - k_{iy}^2) \Big] \end{aligned} \tag{2.67}$$

$$\begin{aligned} \overline{a}_{11} &= \frac{\overline{e}_i}{k^2\, k_{iz}^3} \cdot \Big[-(\hat{x}\,\hat{y} + \hat{y}\,\hat{x})\, k_{iz}^3 - (\hat{x}\,\hat{z} + \hat{z}\,\hat{x})\, k_{iy}\,(k_{ix}^2 + k_{iz}^2) \\ &\quad - (\hat{y}\,\hat{z} + \hat{z}\,\hat{y})\, k_{ix}\,(k_{iy}^2 + k_{iz}^2) \Big] \end{aligned} \tag{2.68}$$

$$\begin{aligned} \overline{a}_{20} &= \frac{\overline{e}_i}{2\,k^2\, k_{iz}^3} \cdot \Big[-2\,(\hat{x}\,\hat{x} - \hat{z}\,\hat{z})\, k_{iz}^3 - (\hat{x}\,\hat{z} + \hat{z}\,\hat{x})\, k_{ix}\,(k_{ix}^2 + 3\,k_{iz}^2) \\ &\quad - (\hat{y}\,\hat{z} + \hat{z}\,\hat{y})\, k_{iy}\,(k^2 - k_{iy}^2) \Big] \end{aligned} \tag{2.69}$$

$$\overline{a}_{02} = \frac{\overline{e}_i}{2\,k^2\,k_{iz}^3} \cdot \Big[-2\,(\hat{y}\,\hat{y} - \hat{z}\,\hat{z})\,k_{iz}^3 - (\hat{x}\,\hat{z} + \hat{z}\,\hat{x})\,k_{ix}\,(k^2 - k_{ix}^2) - (\hat{y}\,\hat{z} + \hat{z}\,\hat{y})\,k_{iy}\,(k_{iy}^2 + 3\,k_{iz}^2)\Big] \tag{2.70}$$

Following a similar procedure, approximations for the magnetic field and the dual tapered wave (Section 2.2.3) can be derived.

2.4 Conclusions

We considered the problem of constructing a 3-D tapered wave as a superposition of plane waves, taking into account both propagating and evanescent waves. The use of the simple Gaussian plane wave spectrum was recommended in order to avoid problems near the grazing incidence. The special choice introduced for the polarization vectors removed the problems of losing a dominant polarization state and degradation of tapering near the normal incidence. Mathematically speaking, the proposed polarization vectors are analytic at the origin of the 2-D wavenumber space. Moreover, the choice of polarization vectors was shown to lead to an exact solution of the Maxwell equations which is an optimal approximation of an ideal but non-Maxwellian tapered field that is constructed by multiplying a scalar tapered wave with a constant polarization vector. The result is a reliably tapered wave with a dominant polarization state that can be used uniformly for all angles of incidence. We discussed the application of the proposed tapered wave in simulating 3-D electromagnetic scattering from a conducting object over a conducting rough surface. Newly encountered problems near the grazing incidence were attributed to secondary edge effects which are unrelated to the tapered incident wave but indicate the difficulty of the rough surface scattering problem at low grazing angles of incidence when objects are present. It was pointed out that methods which avoid such edge effects could also benefit from the utilization of the tapered wave. In some situations it might be desirable to have an approximate 3-D tapered wave at one's disposal which does not require a 2-D numer-

ical integration (summation of plane waves), trading accuracy in satisfying Maxwell's equations for computational speed. We presented the derivation of approximations for both the 3-D scalar and vector case. The expansion of the polarization vectors is based on their analyticity. The local character of the technique employed forces the breakdown of the approximations at grazing incidence.

Chapter 3

Electromagnetic induction sensing of conducting and permeable objects

3.1 Introduction

Low-frequency electromagnetic induction methods are promising candidates for the development of advanced techniques for the detection and discrimination of subsurface objects, such as unexploded ordnance (UXO) and landmines buried in soil [51, 52]. Innovative broadband sensors are being engineered [53]. In the frequency range under consideration here (from about 30 Hz to 300 kHz) rough air-ground interfaces and most soil dielectric heterogeneities have an insignificant influence, a clear advantage relative to ground penetrating radar (GPR) [54]. The conductivity of metallic targets exceeds that of soil by many orders of magnitude so that secondary sources on and within the targets dominate. Also in this frequency range, displacement currents are negligible both within the target and its surroundings. These considerations motivate interest in solutions for the magnetoquasistatic response of conducting and permeable objects embedded in a homogeneous and insulating medium [55]. Note that in this

idealized model, the fields in the background medium obey Laplace's equation, while inside the target they are governed by magnetic diffusion, i. e., a Helmholtz equation with imaginary squared wavenumber. The frequency range of interest encompasses the scattering regimes from near magnetostatics up to the limiting case of vanishing skin depth, when the object can be replaced by an equivalent perfectly conducting boundary, still within the magnetoquasistatic regime.

Objects of general shape can be analyzed with help of a surface integral formulation and the method of moments (MoM). Results for conducting and permeable bodies of revolution were reported in [56]. The problem of a prohibitively fine discretization for skin depths that are small compared to the largest target dimension can be addressed by a special formulation taking into account the exponential decay of the fields inside the object [57]. Other numerical techniques under development include the method of auxiliary sources (MAS) [58].

Recent research in this area has increased the demand for analytical solutions for canonically shaped objects needed for testing of numerical codes, calibration of instruments, and the development of model-based inversion methods. Theoretical investigations can also aid in improving the understanding of some relatively counter-intuitive diffusion phenomena.

A benchmark solution is that for a conducting and permeable sphere, originally developed with focus on geophysical applications [59]–[63]. We consider here the problem of a conducting and permeable prolate spheroid (elongated ellipsoid of revolution) with the exciting uniform primary field along the major axis. The prolate spheroid is of fundamental interest because it includes the special cases of the sphere and, in the limit of infinite length, the circular cylinder. Furthermore, it is an example of an orientable object that exhibits a continuously varying surface curvature. The oblate spheroid (flattened ellipsoid of revolution) can be treated in a manner similar to what is presented in this thesis. For a prolate spheroid, the response to axial excitation field components is typically the strongest.

The key ingredients of one of the solutions advanced here (based on scalar spheroidal wavefunctions) are mentioned in [63, 64] but integral equation approaches to the boundary value problem are favored there. In [65] no numerical results were reported and the solution given appears not to satisfy the boundary conditions at the surface of the spheroid. The lack of a comprehensive treatment of the spheroidal magnetic diffusion problem in the open literature is the chief motivation of the present work which also aims at providing numerical reference data. The formally more complicated use of vector spheroidal wavefunctions for both axial and transverse primary fields is dealt with in [66, 67], from which our approach here is distinguished in that we rely on both the electric and magnetic fields to construct the ultimate magnetoquasistatic solution.

It should be noted that the problem of plane wave scattering from dielectric spheroids, the solution of which is highly developed [68]–[76], is quite different from the magnetic diffusion or electromagnetic induction problem considered here. Both phenomena are governed by a Helmholtz equation. However, the squared wavenumber inside a dielectric body is real, while inside a conducting and permeable object under magnetoquasistatic excitation it is imaginary. The elementary primary field in magnetic diffusion is not a plane wave but a spatially uniform, time-varying magnetic field. In the radar case, an important far-field quantity is the scattering cross-section while in electromagnetic induction we are interested in the induced magnetic dipole moment. Numerically, the exact solution of the diffusion problem requires the evaluation of the spheroidal wavefunctions with complex wavenumber parameter while Fortran and C routines are readily available only for the real case [77]–[79]. Similarities between the radar and the electromagnetic induction problems include the appearance of infinite systems of equations due to the non-orthogonality of the spheroidal wavefunctions for different wavenumbers. In principle, it might be possible to reduce the formal solution of the appropriate plane-wave scattering problem to that of the electromagnetic induction problem by considering the mathematical limit

as the wavenumber of the exterior space approaches zero and treating the imminent singularities correctly. However, this statement is of no immediate practical value. We have found it more convenient to solve the electromagnetic induction problem directly under the tailored and simplifying assumptions of magnetoquasistatics.

In what follows, Section 3.2.1 presents the formal solution of the boundary value problem. It is specialized in Section 3.2.1 to a succinct expression for the induced magnetic dipole moment of the scattering body. In Section 3.2.1 we determine an asymptotic high-frequency form, which in the limit provides the correct normalization value. A low-frequency form is obtained in Section 3.2.1, which provides a check and a simplified expression for the magnetic polarizability, $R^{\parallel}_{\mathrm{pro}}$, for high relative permeabilities, or gives a limiting $R^{\parallel}_{\mathrm{pro}}$ value under finite permeability but large elongation. In Section 3.2.1 the same expression for $R^{\parallel}_{\mathrm{pro}}$ is obtained for the general case with high permeability as was obtained for the low-frequency case in Section 3.2.1. The asymptotic high-frequency form of Section 3.2.1 is enhanced in Section 3.2.2 to provide an approximation for the general solution at high frequencies. An approximate solution for large elongations is developed in Section 3.2.3. Section 3.2.4 presents the numerical implementation of results. These reveal that evaluation of the spheroidal wavefunctions breaks down, rather suddenly, at and above intermediate frequencies. The problem is exacerbated for large permeabilities and elongations. However, using the above-mentioned enhanced high-frequency approximation, we succeed in obtaining values at the high-frequency end of the spectrum, leaving possibly a gap only at intermediate frequencies. This gap can be bridged by the use of a broadband rational approximation, explained in Section 3.2.5.

When employing electromagnetic induction methods to the detection and identification of UXO, one is in practice confronted with the problem of discriminating between UXO and clusters of metallic pieces. In Section 3.3 we develop a suitable formulation for collections of small objects and study simulation results for a theoretical model [80]. A qualitative comparison with an electromagnetic induction measurement

is made.

In Section 3.4 we derive useful forms for expressing and calculating the magnetic dipole moment of an arbitrarily shaped scattering body.

3.2 Magnetoquasistatic response of prolate spheroid under axial excitation

3.2.1 Solution of boundary value problem

We consider a prolate spheroid of conductivity σ_1 and permeability μ_1 with major axis or length

$$\ell = d\,\xi_0 \tag{3.1}$$

and minor axis

$$2a = d\sqrt{\xi_0^2 - 1} \tag{3.2}$$

as shown in Fig. 3-1. In other words, the interfocal distance of the spheroid is [81]

$$d = \sqrt{\ell^2 - 4a^2} \tag{3.3}$$

and ξ_0 is given by

$$\xi_0 = \frac{\ell}{\sqrt{\ell^2 - 4a^2}} \tag{3.4}$$

with $d \to 0$ and $\xi_0 \to \infty$ in the limiting case of a sphere, and $d \to \ell$ and $\xi_0 \to 1$ in the limiting case of a long circular cylinder with needle-like end caps (acicular limit). The spheroid is centered about the origin of a prolate spheroidal coordinate system (η, ξ, ϕ) with both the interfocal distance and the rotational axis coinciding with those of the spheroid so that $\xi = \xi_0$ describes the surface of the spheroid ($|\eta| \leq 1$ and $\xi \geq 1$). As mentioned above, the homogeneous background medium of permeability μ is considered to be non-conducting.

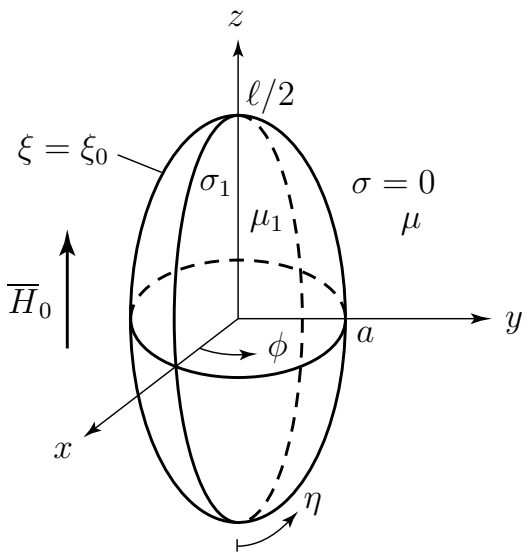

Figure 3-1: A conducting and permeable prolate spheroid in a time-varying, spatially uniform axial primary magnetic field. The background medium is homogeneous and non-conducting.

A uniform primary magnetic field in direction of the axis of rotation and alternating with angular frequency ω is given by

$$\overline{H}_0 = \hat{z}\, H_{0z} \tag{3.5}$$

In view of the rotational symmetry of the configuration, the total electric field is of the form

$$\overline{E} = \hat{\phi}\, E_\phi(\eta, \xi) \tag{3.6}$$

and thus immediately

$$\nabla \cdot \overline{E} = 0 \tag{3.7}$$

It is readily shown that in this case the vector wave equation

$$\nabla \times \nabla \times \overline{E} - k^2\, \overline{E} = 0 \tag{3.8}$$

is reduced by (3.7) to the vector Helmholtz equation

$$\nabla^2 \overline{E} + k^2 \overline{E} = 0 \tag{3.9}$$

and can be reduced further to the scalar Helmholtz equation

$$\nabla^2 \left(E_\phi \, \mathrm{e}^{\pm \mathrm{i}\phi} \right) + k^2 \, E_\phi \, \mathrm{e}^{\pm \mathrm{i}\phi} = 0 \tag{3.10}$$

The introduction of the auxiliary factor $\mathrm{e}^{\pm \mathrm{i}\phi}$ in (3.10) is strictly a mathematical convenience, and the product field $E_\phi \, \mathrm{e}^{\pm \mathrm{i}\phi}$ has no direct physical meaning.

Expansion into scalar spheroidal wavefunctions

In view of (3.10), inside the spheroid (in region 1) the electric field $E_\phi = E_{1\phi}$ is expanded in terms of angular and radial spheroidal wavefunctions of the first kind of order $m = 1$ as [81]

$$E_{1\phi}(\eta, \xi) = H_{0z} \, \mathrm{i}\omega\mu_1 \, \frac{d}{2} \sum_{n=1}^{\infty} A_n \, \mathrm{R}_{1n}^{(1)}(c_1, \xi) \, \mathrm{S}_{1n}(c_1, \eta) \tag{3.11}$$

where the spheroidal wavenumber parameter

$$c_1 = k_1 \, \frac{d}{2} = \frac{d}{2} \sqrt{\mathrm{i}\omega\mu_1\sigma_1} \tag{3.12}$$

is complex with argument $\pi/4$ (provided that the product $\omega\mu_1\sigma_1$ is positive real which is the case in all the numerical examples considered). In region 2 outside the spheroid, $k^2 = 0$ so that (3.10) becomes Laplace's equation, and we may express the electric field in terms of associated Legendre functions of the first and second kind as [82]

$$E_{2\phi}(\eta, \xi) = H_{0z} \, \mathrm{i}\omega\mu \, \frac{d}{2} \left[\frac{1}{2} \sqrt{\xi^2 - 1} \, \mathrm{P}_1^1(\eta) + \sum_{n=1}^{\infty} B_n \, \mathrm{Q}_n^1(\xi) \, \mathrm{P}_n^1(\eta) \right] \tag{3.13}$$

where we follow Flammer [81] in defining P_n^m in terms of Legendre polynomials by

$$\mathrm{P}_n^m(\eta) = \left(1-\eta^2\right)^{\frac{m}{2}} \frac{\mathrm{d}^m}{\mathrm{d}\eta^m}\mathrm{P}_n(\eta) \tag{3.14}$$

which is different by a factor of $(-1)^m$ from the standard definition [83].

In (3.13), the infinite series represents the exterior secondary or scattered field that vanishes as $\xi \to \infty$. The first term is induced by the uniform primary magnetic field in the absence of the scatterer and can also be written as

$$E_{0\phi} = H_{0z}\,\mathrm{i}\omega\mu\,\frac{\rho}{2} \tag{3.15}$$

where we refer to cylindrical coordinates (z, ρ, ϕ). If the scattered field is made vanishingly weak, the electric field (3.6) reduces to

$$\overline{E}_0 = \hat{\phi}\,E_{0\phi}(\rho, z) \tag{3.16}$$

By integrating Faraday's law

$$\nabla \times \overline{E}_0 = \mathrm{i}\omega\mu\,\overline{H}_0 \tag{3.17}$$

or, equivalently,

$$-\frac{\partial}{\partial z}\,E_{0\phi} = 0 \tag{3.18}$$

and

$$\frac{1}{\rho}\,\frac{\partial}{\partial \rho}\,(\rho\,E_{0\phi}) = H_{0z}\,\mathrm{i}\omega\mu \tag{3.19}$$

we find that (3.16) with $E_{0\phi}$ given by (3.15) is the only possible electric field $\overline{E}_0$ produced by (3.5) and complying with (3.6). The presence of the spheroid imposes, via the boundary condition for the tangential electric field, a symmetry on the exterior electric field that otherwise would be determined only up to an additive irrotational field, due to the assumed absence of any currents in the exterior space.

The non-zero components of the total magnetic field follow from (3.11), (3.13) and Faraday's law, applying the curl operator in prolate spheroidal coordinates. They are given, in region 1, by

$$H_{1\eta}(\eta,\xi) = \frac{H_{0z}}{\sqrt{\xi^2-\eta^2}} \sum_{n=1}^{\infty} A_n \, T_{1n}(c_1,\xi) \, \mathrm{S}_{1n}(c_1,\eta) \tag{3.20}$$

$$H_{1\xi}(\eta,\xi) = -\frac{H_{0z}}{\sqrt{\xi^2-\eta^2}} \sum_{n=1}^{\infty} A_n \, \mathrm{R}^{(1)}_{1n}(c_1,\xi) \, \frac{\mathrm{d}}{\mathrm{d}\eta} \left[\left(1-\eta^2\right) \mathrm{S}_{1n}(c_1,\eta) \right] \tag{3.21}$$

with the derivative

$$T_{mn}(c_1,\xi) = \frac{\mathrm{d}}{\mathrm{d}\xi} \left[\sqrt{\xi^2-1} \, \mathrm{R}^{(1)}_{mn}(c_1,\xi) \right] \tag{3.22}$$

and, in region 2, by

$$H_{2\eta}(\eta,\xi) = \frac{H_{0z}}{\sqrt{\xi^2-\eta^2}} \left[\xi \, \mathrm{P}^1_1(\eta) + \sum_{n=1}^{\infty} B_n \, U_{1n}(\xi) \, \mathrm{P}^1_n(\eta) \right] \tag{3.23}$$

$$H_{2\xi}(\eta,\xi) = -\frac{H_{0z}}{\sqrt{\xi^2-\eta^2}} \left[\frac{1}{2} \sqrt{\xi^2-1} \, V_{11}(\eta) + \sum_{n=1}^{\infty} B_n \, \mathrm{Q}^1_n(\xi) \, V_{1n}(\eta) \right] \tag{3.24}$$

where

$$U_{mn}(\xi) = \frac{\mathrm{d}}{\mathrm{d}\xi} \left[\sqrt{\xi^2-1} \, \mathrm{Q}^m_n(\xi) \right] \tag{3.25}$$

$$V_{mn}(\eta) = \frac{\mathrm{d}}{\mathrm{d}\eta} \left[\sqrt{1-\eta^2} \, \mathrm{P}^m_n(\eta) \right] \tag{3.26}$$

The boundary conditions of continuous tangential electric and magnetic field require, respectively,

$$\sum_{n=1}^{\infty} \left[A_n \, \mu_1 \, \mathrm{R}^{(1)}_{1n}(c_1,\xi_0) \, \mathrm{S}_{1n}(c_1,\eta) - B_n \, \mu \, \mathrm{Q}^1_n(\xi_0) \, \mathrm{P}^1_n(\eta) \right] = \frac{\mu}{2} \sqrt{\xi_0^2-1} \, \mathrm{P}^1_1(\eta) \tag{3.27}$$

$$\sum_{n=1}^{\infty} \left[A_n \, T_{1n}(c_1,\xi_0) \, \mathrm{S}_{1n}(c_1,\eta) - B_n \, U_{1n}(\xi_0) \, \mathrm{P}^1_n(\eta) \right] = \xi_0 \, \mathrm{P}^1_1(\eta) \tag{3.28}$$

In a crucial step, the angle functions are now expanded as [81]

$$\mathrm{S}_{mn}(c_1,\eta) = \sum_{r=0,1}^{\infty}{}' \, \mathrm{d}_r^{mn}(c_1)\, \mathrm{P}_{m+r}^{m}(\eta) \tag{3.29}$$

where the summation starts with $r = 0$ for $n - m$ even and with $r = 1$ when $n - m$ odd, and the prime means that, beginning with the first, only every second term in the summation is kept, e. g., for an odd n,

$$\mathrm{S}_{1n}(c_1,\eta) = \mathrm{d}_0^{1n}(c_1)\, \mathrm{P}_1^1(\eta) + \mathrm{d}_2^{1n}(c_1)\, \mathrm{P}_3^1(\eta) + \mathrm{d}_4^{1n}(c_1)\, \mathrm{P}_5^1(\eta) + \ldots \tag{3.30}$$

and, if n even,

$$\mathrm{S}_{1n}(c_1,\eta) = \mathrm{d}_1^{1n}(c_1)\, \mathrm{P}_2^1(\eta) + \mathrm{d}_3^{1n}(c_1)\, \mathrm{P}_4^1(\eta) + \mathrm{d}_5^{1n}(c_1)\, \mathrm{P}_6^1(\eta) + \ldots \tag{3.31}$$

The numerical evaluation of the spheroidal expansion coefficients d_r^{mn}, which will also be utilized in the computation of the radial wavefunctions $\mathrm{R}_{mn}^{(1)}$ [based on the expansion (3.57) below], is discussed in Section 3.2.4. Inserting (3.29) in (3.27), (3.28) gives

$$\sum_{n,r=1}^{\infty} \Big[A_{2n-1}\, \mu_1\, \mathrm{R}_{1(2n-1)}^{(1)}(c_1,\xi_0)\, \mathrm{d}_{2r-2}^{1(2n-1)}(c_1)\, \mathrm{P}_{2r-1}^1(\eta)$$

$$+ A_{2n}\, \mu_1\, \mathrm{R}_{1(2n)}^{(1)}(c_1,\xi_0)\, \mathrm{d}_{2r-1}^{1(2n)}(c_1)\, \mathrm{P}_{2r}^1(\eta) - B_n\, \mu\, \mathrm{Q}_n^1(\xi_0)\, \mathrm{P}_n^1(\eta)\, \delta_{nr} \Big] = \frac{\mu}{2}\, \sqrt{\xi_0^2 - 1}\, \mathrm{P}_1^1(\eta) \tag{3.32}$$

$$\sum_{n,r=1}^{\infty} \Big[A_{2n-1}\, T_{1(2n-1)}(c_1,\xi_0)\, \mathrm{d}_{2r-2}^{1(2n-1)}(c_1)\, \mathrm{P}_{2r-1}^1(\eta)$$

$$+ A_{2n}\, T_{1(2n)}(c_1,\xi_0)\, \mathrm{d}_{2r-1}^{1(2n)}(c_1)\, \mathrm{P}_{2r}^1(\eta) - B_n\, U_{1n}(\xi_0)\, \mathrm{P}_n^1(\eta)\, \delta_{nr} \Big] = \xi_0\, \mathrm{P}_1^1(\eta) \tag{3.33}$$

where δ_{nr} is the Kronecker delta. Using the orthogonality of the associated Legendre

functions [83]

$$\int_{-1}^{1} \mathrm{d}\eta \, \mathrm{P}_m^1(\eta) \, \mathrm{P}_n^1(\eta) = \frac{2m\,(m+1)}{2m+1} \, \delta_{mn} \tag{3.34}$$

we find from multiplying (3.32), (3.33) by $\mathrm{P}_{2m-1}^1(\eta)$ and integrating for $m = 1, 2, \ldots$

$$\sum_{n=1}^{\infty} A_{2n-1} \, \mu_1 \, \mathrm{R}_{1(2n-1)}^{(1)}(c_1, \xi_0) \, \mathrm{d}_{2m-2}^{1(2n-1)}(c_1) - B_{2m-1} \, \mu \, \mathrm{Q}_{2m-1}^1(\xi_0) \; = \frac{\mu}{2} \sqrt{\xi_0^2 - 1} \, \delta_{(2m-1)1} \tag{3.35}$$

$$\sum_{n=1}^{\infty} A_{2n-1} \, T_{1(2n-1)}(c_1, \xi_0) \, \mathrm{d}_{2m-2}^{1(2n-1)}(c_1) - B_{2m-1} \, U_{1(2m-1)}(\xi_0) = \xi_0 \, \delta_{(2m-1)1} \tag{3.36}$$

and from testing with $\mathrm{P}_{2m}^1(\eta)$

$$\sum_{n=1}^{\infty} A_{2n} \, \mu_1 \, \mathrm{R}_{1(2n)}^{(1)}(c_1, \xi_0) \, \mathrm{d}_{2m-1}^{1(2n)}(c_1) - B_{2m} \, \mu \, \mathrm{Q}_{2m}^1(\xi_0) = 0 \tag{3.37}$$

$$\sum_{n=1}^{\infty} A_{2n} \, T_{1(2n)}(c_1, \xi_0) \, \mathrm{d}_{2m-1}^{1(2n)}(c_1) - B_{2m} \, U_{1(2m)}(\xi_0) = 0 \tag{3.38}$$

Thus we conclude that all harmonics with even index vanish, i. e.,

$$A_{2n} = B_{2n} = 0 \tag{3.39}$$

This is expected from the symmetry of the problem which implies

$$E_\phi(\xi, \eta) = E_\phi(\xi, -\eta) \tag{3.40}$$

Eliminating the B_{2m-1} from (3.35), (3.36) we arrive at the infinite system of linear equations given by

$$\sum_{n=1}^{\infty} A_{2n-1} \, \mathrm{d}_{2m-2}^{1(2n-1)}(c_1) \left[\mu_1 \, U_{1(2m-1)}(\xi_0) \, \mathrm{R}_{1(2n-1)}^{(1)}(c_1, \xi_0) - \mu \, \mathrm{Q}_{2m-1}^1(\xi_0) \, T_{1(2n-1)}(c_1, \xi_0) \right]$$

$$= \mu \left[\frac{1}{2} \sqrt{\xi_0^2 - 1}\, U_{1(2m-1)}(\xi_0) - \xi_0\, \mathrm{Q}^1_{2m-1}(\xi_0) \right] \delta_{(2m-1)1} \tag{3.41}$$

After solving (3.41), the B_{2m-1} can be obtained directly from

$$B_{2m-1} = \frac{1}{\mu\, \mathrm{Q}^1_{2m-1}(\xi_0)} \left[\mu_1 \sum_{n=1}^{\infty} A_{2n-1}\, \mathrm{R}^{(1)}_{1(2n-1)}(c_1, \xi_0)\, \mathrm{d}^{1(2n-1)}_{2m-2}(c_1) - \frac{\mu}{2} \sqrt{\xi_0^2 - 1}\, \delta_{(2m-1)1} \right] \tag{3.42}$$

which concludes the formal solution of the boundary value problem. In the following we discuss the induced magnetic dipole moment and various limiting cases of the theory. The numerical implementation of (3.41), (3.42) is described in Section 3.2.4.

Induced magnetic dipole moment

The secondary magnetic field due to an induced magnetic dipole of moment $\overline{m}$ at $\overline{r} = \overline{r}_0$ is given by [51, 56, 84]

$$\overline{H}_s(\overline{r}) = \frac{3\,\hat{r}'\hat{r}' - \overline{\overline{I}}}{4\pi r'^3} \cdot \overline{m} \tag{3.43}$$

where $\overline{\overline{I}}$ denotes the identity tensor and

$$\hat{r}' = \frac{\overline{r} - \overline{r}_0}{|\overline{r} - \overline{r}_0|}\,, \quad r' = |\overline{r} - \overline{r}_0| \tag{3.44}$$

Due to the rapid decay of the higher-order multipole fields, $\overline{m}$ is a quantity of primary practical interest in electromagnetic induction methods.

For our spheroid problem, the induced dipole moment is found from (3.23), (3.24) where the secondary field is represented by the infinite series involving the coefficients B_n. As $\xi \to \infty$, the term for $n = 1$ dominates. This is evident from the representation of Q^1_n as (8.1.3 in [83])

$$\mathrm{Q}^1_n(\xi) = -\frac{2^n\,(n+1)!\,n!}{(2n+1)\,(2n)!}\, \frac{\sqrt{\xi^2 - 1}}{\xi^{n+2}}\, \mathrm{F}\left(\frac{n+3}{2}, \frac{n+2}{2}; \frac{2n+3}{2}; \frac{1}{\xi^2} \right) \tag{3.45}$$

where the hypergeometric function F is given by the specialized Gauss hypergeometric series (15.1.1 and 6.1.15 in [83])

$$\mathrm{F}\left(\frac{n+3}{2},\frac{n+2}{2};\frac{2n+3}{2};\frac{1}{\xi^2}\right)=1+\frac{(n+2)\,(n+3)}{2\,(2n+3)}\,\xi^{-2}+\mathcal{O}(\xi^{-4}) \tag{3.46}$$

Note that (3.46) is a Taylor expansion about $\xi=\infty$. Thus, using

$$\sqrt{\xi^2-1}=\xi-\frac{1}{2}\,\xi^{-1}+\mathcal{O}(\xi^{-3}) \tag{3.47}$$

we have

$$\mathrm{Q}_n^1(\xi)=-\frac{2^n\,n!\,(n+1)!}{(2n+1)\,(2n)!}\left\{\xi^{-(n+1)}+\frac{n^2+3n+3}{2\,(2n+3)}\,\xi^{-(n+3)}+\mathcal{O}\Big[\xi^{-(n+5)}\Big]\right\} \tag{3.48}$$

$$U_{1n}(\xi)=\frac{n\,2^n\,n!\,(n+1)!}{(2n+1)\,(2n)!}\left\{\xi^{-(n+1)}+\frac{(n+1)\,(n+2)}{2\,(2n+3)}\,\xi^{-(n+3)}+\mathcal{O}\Big[\xi^{-(n+5)}\Big]\right\} \tag{3.49}$$

By using the leading order terms of the resulting expansions

$$\mathrm{Q}_1^1(\xi)=-\frac{2}{3}\,\xi^{-2}-\frac{7}{15}\,\xi^{-4}+\mathcal{O}(\xi^{-6}) \tag{3.50}$$

$$U_{11}(\xi)=\frac{2}{3}\,\xi^{-2}+\frac{2}{5}\,\xi^{-4}+\mathcal{O}(\xi^{-6}) \tag{3.51}$$

and noting that, as $\xi\to\infty$, the surfaces $\xi=$ const. become spherical and [81]

$$\frac{d}{2}\,\xi\to r\ ,\quad \eta\to\cos\theta \tag{3.52}$$

where r and θ are spherical coordinates, we find

$$\overline{m}=\hat{z}\,H_{0z}\,\frac{\pi d^3}{6}\,\frac{\sqrt{\xi_0^2-1}}{\mathrm{Q}_1^1(\xi_0)}\,R_{\mathrm{pro}}^{\parallel} \tag{3.53}$$

with the polarizability factor for prolate spheroids under axial excitation

$$R^{\parallel}_{\rm pro} = -\frac{2\,\mathrm{Q}^1_1(\xi_0)}{\sqrt{\xi_0^2-1}}\,B_1 \tag{3.54}$$

As shown below, the normalization of $R^{\parallel}_{\rm pro}$ is such that

$$R^{\parallel}_{\rm pro} \to 1 \tag{3.55}$$

in the high-frequency limit. Because in (3.53), (3.54) frequency only enters implicitly through B_1, (3.53) is also a statement of the induced dipole moment in this limit. The value of the associated Legendre function $\mathrm{Q}^1_1(\xi_0) < 0$ required in the normalization is given in terms of elementary functions by

$$\mathrm{Q}^1_1(\xi_0) = -\frac{1}{2}\sqrt{\xi_0^2-1}\left(\frac{2\,\xi_0}{\xi_0^2-1} - \ln\frac{\xi_0+1}{\xi_0-1}\right) \tag{3.56}$$

High-frequency limit

The limit (3.55) is most conveniently verified by setting $E_{2\phi}$ according to (3.13) to zero at $\xi = \xi_0$ (equivalence of perfectly conducting spheroid and spheroid with vanishing skin depth) and noting that all B_n other than B_1 are zero.

Obtaining the high-frequency limit directly from (3.41), (3.42) requires an investigation of the asymptotic behavior of the radial spheroidal wavefunction and its derivative. Consider the expansion [81]

$$\begin{aligned}\mathrm{R}^{(1)}_{mn}(c_1,\xi) &= \left(\frac{\xi^2-1}{\xi^2}\right)^m \left[\sum_{r=0,1}^{\infty\,\prime} \frac{(2m+r)!}{r!}\,\mathrm{d}^{mn}_r(c_1)\right]^{-1} \\ &\quad\times \sum_{r=0,1}^{\infty\,\prime} \mathrm{i}^{r+m-n}\,\frac{(2m+r)!}{r!}\,\mathrm{d}^{mn}_r(c_1)\,\mathrm{j}_{m+r}(c_1\,\xi)\end{aligned} \tag{3.57}$$

where the summation convention is the same as for (3.29) and the j_n are the spherical

Bessel functions of the first kind [83]. As $\mathrm{Im}\{c_1\} \to \infty$, the right-hand side of

$$\mathrm{i}^{r+m-n}\, \mathrm{j}_{m+r}(c_1\,\xi) \sim \frac{\mathrm{i}^{n+1}}{2}\, \frac{\mathrm{e}^{-\mathrm{i}\,c_1\,\xi}}{c_1\,\xi} \tag{3.58}$$

is in fact independent of the summation index r. Thus (3.57) becomes asymptotically, for a finite ξ,

$$\mathrm{R}^{(1)}_{mn}(c_1,\xi) \sim \frac{\mathrm{i}^{n+1}}{2}\, \left(\frac{\xi^2-1}{\xi^2}\right)^m\, \frac{\mathrm{e}^{-\mathrm{i}\,c_1\,\xi}}{c_1\,\xi} \tag{3.59}$$

and we find, inserting (3.59) in the definition (3.22) and dividing by (3.59),

$$\frac{T_{mn}(c_1,\xi)}{\mathrm{R}^{(1)}_{mn}(c_1,\xi)} \sim -\mathrm{i}\,c_1\sqrt{\xi^2-1} \tag{3.60}$$

With the help of (3.60) we now obtain from (3.41)

$$\sum_{n=1}^{\infty} A_{2n-1}\, \mathrm{R}^{(1)}_{1(2n-1)}(c_1,\xi_0)\, \mathrm{d}^{1(2n-1)}_{2m-2}(c_1)$$

$$\sim \frac{\mu}{2}\, \frac{\sqrt{\xi_0^2-1}\, U_{1(2m-1)}(\xi_0) - 2\,\xi_0\, \mathrm{Q}^1_{2m-1}(\xi_0)}{\mu_1\, U_{1(2m-1)}(\xi_0) + \mathrm{i}\mu\, c_1\, \sqrt{\xi_0^2-1}\, \mathrm{Q}^1_{2m-1}(\xi_0)}\, \delta_{(2m-1)1} \tag{3.61}$$

This shows that in the high-frequency limit the infinite series in (3.42) can be summed up in closed form. This observation saves ourselves specifying the asymptotic behavior of the angular expansion coefficients $\mathrm{d}^r_{mn}(c_1)$ and we find

$$B_{2m-1} \sim -\frac{1}{2}\, \frac{2\,\mu_1\,\xi_0 + \mathrm{i}\mu\, c_1\, (\xi_0^2-1)}{\mu_1\, U_{1(2m-1)}(\xi_0) + \mathrm{i}\mu\, c_1\, \sqrt{\xi_0^2-1}\, \mathrm{Q}^1_{2m-1}(\xi_0)}\, \delta_{(2m-1)1} \tag{3.62}$$

indicating that as expected the B_n other than B_1 vanish to leading order, and, with (3.62) from (3.54),

$$R^{\parallel}_{\mathrm{pro}} \sim \frac{\mathrm{Q}^1_1(\xi_0)}{\sqrt{\xi_0^2-1}}\, \frac{2\,\mu_1\,\xi_0 + \mathrm{i}\mu\, c_1\, (\xi_0^2-1)}{\mu_1\, U_{11}(\xi_0) + \mathrm{i}\mu\, c_1\, \sqrt{\xi_0^2-1}\, \mathrm{Q}^1_1(\xi_0)} \tag{3.63}$$

As c_1 increases with frequency, the terms containing μ_1 become negligible, so that

(3.63) reduces to (3.55). We return to (3.63) in Section 3.2.2.

Low-frequency limit

In the low-frequency limit we observe that, because the spheroidal angle functions S_{mn} reduce to the associated Legendre functions of the first kind [81], or

$$\mathrm{d}_r^{mn}(c_1) \to \delta_{(n-m)r} \tag{3.64}$$

in (3.29), the equations (3.41) for the A_n decouple and only A_1 and B_1 in (3.42) are non-zero. Obtaining B_1 by eliminating A_1 and making use of the asymptotic relations

$$\mathrm{R}_{11}^{(1)}(c_1,\xi_0) \sim c_1 \,\frac{\mathrm{j}_1(c_1\,\xi_0)}{c_1\,\xi_0}\,\sqrt{\xi_0^2-1} \sim \frac{c_1}{3}\,\sqrt{\xi_0^2-1} \tag{3.65}$$

and thus

$$T_{11}(c_1,\xi_0) \sim \frac{2}{3}\,c_1\,\xi_0 \tag{3.66}$$

we find from (3.54)

$$R_{\mathrm{pro}}^{\parallel} \to \frac{2\,(\mu_1-\mu)\,\xi_0\,\mathrm{Q}_1^1(\xi_0)}{\mu_1\,\sqrt{\xi_0^2-1}\,U_{11}(\xi_0) - 2\mu\,\xi_0\,\mathrm{Q}_1^1(\xi_0)} \tag{3.67}$$

where

$$U_{11}(\xi_0) = \xi_0\,\ln\frac{\xi_0+1}{\xi_0-1} - 2 \tag{3.68}$$

[for the evaluation of $\mathrm{Q}_1^1(\xi_0)$ refer to (3.56)]. The limit (3.67) can be shown to be in agreement with the corresponding result in magnetostatics given, e. g., in [85]. If in addition to the low-frequency limit we consider the acicular limit, $\ell/2a \to \infty$, then (3.67) reduces to

$$R_{\mathrm{pro}}^{\parallel} \to -\frac{\mu_1-\mu}{\mu} \tag{3.69}$$

which is the negative magnetic susceptibility of the spheroid. If the elongation of the spheroid is fixed but the relative permeability goes to infinity, $\mu_1/\mu \to \infty$, (3.67)

simplifies to

$$R^{\parallel}_{\mathrm{pro}} \to \frac{2\,\xi_0\,\mathrm{Q}^1_1(\xi_0)}{\sqrt{\xi_0^2-1}\,U_{11}(\xi_0)} \tag{3.70}$$

Limiting case of large relative permeability

Another interesting limiting case of (3.41), (3.42) is that of large relative permeability, $\mu_1/\mu \to \infty$, but with c_1 fixed [note that c_1 depends implicitly on μ_1, c. f., (3.12) and that a fixed c_1 can be achieved by letting $\omega \to 0$ as $\mu_1/\mu \to \infty$]. More direct than in the high-frequency limit, (3.41) in this case yields again a closed-form expression for the infinite sum in (3.42), given by

$$\sum_{n=1}^{\infty} A_{2n-1}\,\mathrm{R}^{(1)}_{1(2n-1)}(c_1,\xi_0)\,\mathrm{d}^{1(2n-1)}_{2m-2}(c_1) \sim \frac{\mu}{\mu_1}\left[\frac{1}{2}\sqrt{\xi_0^2-1} - \frac{\xi_0\,\mathrm{Q}^1_{2m-1}(\xi_0)}{U_{1(2m-1)}(\xi_0)}\right]\delta_{(2m-1)1} \tag{3.71}$$

which, however, does not depend on frequency. Substituting (3.71) into (3.42) we find

$$B_{2m-1} \sim -\frac{\xi_0}{U_{1(2m-1)}(\xi_0)}\,\delta_{(2m-1)1} \tag{3.72}$$

and, using (3.72) in (3.54), we again arrive at the specialized low-frequency limit (3.70).

3.2.2 Approximate solution for high frequencies

As we will see in Section 3.2.4, while our frequency range of interest spans several orders of magnitude, the practical solution of (3.41), (3.42) is possible only for low to intermediate frequencies. The breakdown of this otherwise exact formulation, which is found to be a sudden one, is due to the expansion of the spheroidal wavefunctions into spherical harmonics (3.29), (3.57) which is usable only for sufficiently small magnitude of c_1 [81]. It is therefore important to develop an alternative formulation tractable at high frequencies; or to develop at least approximate or asymptotic solutions that, ideally, would have a range of validity that at the low-frequency end overlaps the

highest frequencies at which the evaluation based on the expansion into spherical harmonics is still possible.

In Section 3.2.1 we derived (3.63) using the leading-order high-frequency asymptotic behavior of the radial spheroidal wavefunction of the first kind and its derivative. We note that this formula still depends on c_1 which makes it a possible candidate for the purposes of this section. Attractive, beside the simple functional form of (3.63) [for the evaluation of $\mathrm{Q}_1^1(\xi_0)$ and $U_{11}(\xi_0)$ see (3.56) and (3.68), respectively], is the fact that, as $\mu_1/\mu \to \infty$ with c_1 fixed, (3.63) simplifies to (3.70), see also Section 3.2.1. Thus, for large relative permeability, a case of practical importance, (3.63) might in fact be a good broadband approximation since it approaches the correct asymptotic values at both the low-frequency and the high-frequency end. However, numerical tests showed that this is true only for the nearly spherical case, $\ell/2a \approx 1$ (Section 3.2.4). In general, the extremum of the imaginary part of (3.63) occurs at a frequency that is too high and, consequently, the real part fails to connect with the exact solution computable at low frequencies. This undesirable behavior makes the formula less useful in practice.

However, an alternative derivation of (3.63) paves our way to an approximation that does work. For this purpose, partially inspired by the starting point of the numerical approach for small skin depths advanced in [57], let us consider a special separable form of the electric field inside the spheroid for high frequencies,

$$E_{1\phi}(\eta,\xi) \approx E_{2\phi}(\eta,\xi_0)\ \mathrm{e}^{\gamma_1\,(\xi-\xi_0)} \tag{3.73}$$

where γ_1 is a dimensionless propagation constant yet to be determined. With (3.73) the boundary condition on the tangential electric field is satisfied automatically, by construction. Inserting (3.73) into (3.10), we quickly discover that if we are to satisfy the wave equation at least approximately we have to set $\gamma_1 = -\mathrm{i}\,c_1$, where the negative sign is chosen based on the physical reasoning that the field inside the spheroid

propagates inward and decays exponentially away from the surface. Then, from Faraday's law with the curl operator in prolate spheroidal coordinates, we can find the $H_{1\eta}$ corresponding to (3.73). By matching with (3.23), satisfying the remaining boundary condition on the tangential magnetic field, and using (3.13), we are led back to (3.62) and what follows there.

Thus, reconsidering (3.73), we conclude that this approximation contains a basic problem, namely, it ignores the variation of the radius of curvature along the surface of the spheroid (a problem that disappears in the spherical limit). Thus, if we are trying to implement the picture of a wave locally one-dimensional in the coordinate normal to the boundary and with complex wavenumber k_1, we have to take into account the metric of the spheroidal coordinate system, motivating the expression

$$E_{1\phi}(\eta,\xi) \approx E_{2\phi}(\eta,\xi_0)\ \mathrm{e}^{-\mathrm{i}\,k_1 \int_{\xi_0}^{\xi} \mathrm{d}\xi'\, h_\xi(\eta,\xi')} \tag{3.74}$$

with the metrical coefficient [81]

$$h_\xi(\eta,\xi) = \frac{d}{2}\sqrt{\frac{\xi^2-\eta^2}{\xi^2-1}} \tag{3.75}$$

Before proceeding we note that near the tips or poles of the spheroid where $|\eta| \approx 1$, (3.73) and (3.74) in fact coincide [specialize (3.75) and recall (3.12)]. Because of the smaller radius of curvature there, this offers an explanation for the erroneous shift of the extremum of the imaginary part of (3.63) to higher frequencies. Furthermore, according to (3.4), in the spherical limit we have $\xi_0 \to \infty$ and thus $\xi \gg 1$ in the thin surface layer where (3.74) again reduces to (3.73). Also, the original derivation leading to (3.63) used an asymptotic formula for the radial wavefunction only but not for the angular wavefunction or its expansion coefficients d_r^{mn}. Neglecting the angular aspect of the spheroidal problem, which was convenient for deriving the high-frequency limit, appears now to be related to the shortcomings of (3.63) as a high-frequency approximation. (Even though we reviewed some of the literature on the

asymptotics of the angular spheroidal wavefunction [86]–[92], so far we have not been led to any alternative formulation for the high-frequency case.)

Using (3.74), in Faraday's law, without further approximation, yields

$$H_{1\eta}(\eta,\xi) \approx \frac{2}{\mathrm{i}\omega\mu_1 d}\,\frac{E_{2\phi}(\eta,\xi_0)}{\sqrt{\xi^2-\eta^2}}\,\frac{\partial}{\partial\xi}\left[\sqrt{\xi^2-1}\,\mathrm{e}^{-\mathrm{i}\,k_1\int_{\xi_0}^{\xi}\mathrm{d}\xi'\,h_\xi(\eta,\xi')}\right] \tag{3.76}$$

$$\approx \frac{2}{\mathrm{i}\omega\mu_1 d}\left(\frac{\xi}{\sqrt{\xi^2-1}}-\mathrm{i}\,c_1\sqrt{\xi^2-\eta^2}\right)\frac{E_{1\phi}(\eta,\xi)}{\sqrt{\xi^2-\eta^2}} \tag{3.77}$$

Matching the remaining boundary condition on the tangential magnetic field we obtain from (3.77), (3.74), (3.13), and (3.23)

$$\sum_{n=1}^{\infty} B_n\left[\frac{\mu_1}{\mu}\,U_{1n}(\xi_0)-\frac{\xi_0}{\sqrt{\xi_0^2-1}}\,\mathrm{Q}_n^1(\xi_0)+\mathrm{i}\,c_1\sqrt{\xi_0^2-\eta^2}\,\mathrm{Q}_n^1(\xi_0)\right]\mathrm{P}_n^1(\eta)$$

$$=\left[-\xi_0\,\frac{2\,\mu_1-\mu}{2\mu}-\frac{\mathrm{i}\,c_1}{2}\sqrt{(\xi_0^2-\eta^2)\,(\xi_0^2-1)}\right]\mathrm{P}_1^1(\eta) \tag{3.78}$$

to be enforced for all η. Introducing the auxiliary function

$$\Pi_{mn}(\xi)=\frac{2m+1}{2m\,(m+1)}\int_{-1}^{1}\mathrm{d}\eta\,\sqrt{\xi^2-\eta^2}\,\mathrm{P}_m^1(\eta)\,\mathrm{P}_n^1(\eta) \tag{3.79}$$

and using (3.34), we get from (3.78) by testing with $\mathrm{P}_m^1(\eta)$ for $m=1,2,\ldots$

$$B_m\left[\frac{\mu_1}{\mu}\,U_{1m}(\xi_0)-\frac{\xi_0}{\sqrt{\xi_0^2-1}}\,\mathrm{Q}_m^1(\xi_0)\right]+\mathrm{i}\,c_1\sum_{n=1}^{\infty}B_n\,\mathrm{Q}_n^1(\xi_0)\,\Pi_{mn}(\xi_0)$$

$$=-\xi_0\,\frac{2\,\mu_1-\mu}{2\mu}\,\delta_{m1}-\frac{\mathrm{i}\,c_1}{2}\sqrt{\xi_0^2-1}\,\Pi_{m1}(\xi_0) \tag{3.80}$$

Since, according to the definition (3.79) and the parity of the associated Legendre functions, $\Pi_{mn}(\xi)=0$ whenever $m-n$ odd, the structure of (3.80) is such that all

the B_m with m even vanish as expected. Thus we arrive at

$$B_{2m-1}\left[\frac{\mu_1}{\mu}\,U_{1(2m-1)}(\xi_0)-\frac{\xi_0}{\sqrt{\xi_0^2-1}}\,\mathrm{Q}^1_{2m-1}(\xi_0)\right]$$

$$+\,\mathrm{i}\,c_1\sum_{n=1}^{\infty}B_{2n-1}\,\mathrm{Q}^1_{2n-1}(\xi_0)\,\Pi_{(2m-1)(2n-1)}(\xi_0)$$

$$=-\xi_0\,\frac{2\,\mu_1-\mu}{2\mu}\,\delta_{(2m-1)1}-\frac{\mathrm{i}\,c_1}{2}\,\sqrt{\xi_0^2-1}\,\Pi_{(2m-1)1}(\xi_0) \tag{3.81}$$

Once the B_m have been obtained from the infinite system of equations (3.81) the high-frequency approximation for the response in the far field represented by $R^{\parallel}_{\mathrm{pro}}$ follows from (3.54). We will follow this procedure numerically in Section 3.2.4 and 3.2.5 where a straightforward Gauss-Legendre quadrature of (3.79) is employed. Finally, we observe that, as $\mu_1/\mu \to \infty$ with c_1 fixed, (3.81) again simplifies to (3.70), indicating that the approximation introduced here can be expected to extend to lower frequencies when the relative permeability is large.

3.2.3 Approximate solution for large elongations

To obtain an approximation of the magnetic polarizability factor $R^{\parallel}_{\mathrm{pro}}$ of a long conducting and permeable prolate spheroid, we note that, as $\ell/2a$ becomes large, the spheroid fills the interior of a circular cylinder while its needle-like poles retreat to infinity. Thus, we can expect the responses of a long spheroid and a long circular cylinder to be similar.

For a circular cylinder with radius a, length ℓ, permeability μ_1, and conductivity σ_1, where $\ell \gg 2a$, we estimate the current distribution and magnetic field internal to the cylinder by those found for an infinitely long cylinder of the same radius, permeability, conductivity, and orientation. This methodology is similar to using an infinite-cylinder approximation for plane-wave scattering from finite-length dielectric cylinders employed in remote sensing applications [93]–[102]. We then obtain the

approximation for the induced magnetic dipole moment of the finite-length cylinder based on the exact functional

$$\overline{m}\left[\overline{J}(\overline{r}),\overline{H}(\overline{r})\right]=\frac{1}{2}\int\limits_{V}\mathrm{d}V\,\overline{r}\times\overline{J}(\overline{r})+\chi_m\int\limits_{V}\mathrm{d}V\,\overline{H}(\overline{r}) \tag{3.82}$$

where V is the region occupied by the cylinder and χ_m is the magnetic susceptibility with respect to the background, defined as

$$\chi_m=\frac{\mu_1}{\mu}-1 \tag{3.83}$$

The first term in (3.82) vanishes as $\omega\to 0$ or $\sigma_1\to 0$, while the second term becomes zero as $\omega\to\infty$ or $\mu_1\to\mu$. A rigorous derivation of (3.82) starting from the equivalence principle is given in Section 3.4.

The solution for the problem of a conducting and permeable *infinite* cylinder in an alternating spatially uniform magnetic field is outlined in [62]. For a cylinder centered at $\rho=0$, with its axis along $\hat{z}$, and a longitudinal primary magnetic field as given by (3.5), the induced currents are

$$\overline{J}(\overline{r})=\hat{\phi}\,H_{0z}\,\frac{k_1\,\mathrm{J}_1(k_1\rho)}{\mathrm{J}_0(k_1a)} \tag{3.84}$$

and the internal magnetic field is

$$\overline{H}(\overline{r})=\hat{z}\,H_{0z}\,\frac{\mathrm{J}_0(k_1\rho)}{\mathrm{J}_0(k_1a)} \tag{3.85}$$

both given in terms of Bessel functions of the first kind with complex argument.

Inserting (3.84), (3.85) into (3.82) and carrying out the integrations leads to the following expression for the magnetic dipole moment of the long cylinder under axial excitation:

$$\overline{m}\approx-\hat{z}\,\pi a^2\ell\,R^{\parallel}_{\mathrm{cyl}} \tag{3.86}$$

with

$$R_{\rm cyl}^{\parallel} = -\frac{k_1 a\, \mathrm{J}_2(k_1 a) + 2\,\chi_m\, \mathrm{J}_1(k_1 a)}{k_1 a\, \mathrm{J}_0(k_1 a)} \tag{3.87}$$

independent of ℓ. For $\omega \to \infty$, we have the normalization

$$R_{\rm cyl}^{\parallel} \to 1 \tag{3.88}$$

and, as $\omega \to 0$, we find

$$R_{\rm cyl}^{\parallel} \to -\chi_m \tag{3.89}$$

which coincides with the acicular low-frequency limit for the prolate spheroid, (3.69). This suggests that the approximation introduced for long but finite-length cylinders can indeed be used to obtain an approximation of the magnetic dipole moment induced in long prolate spheroids under axial excitation, by replacing $R_{\rm pro}^{\parallel}$ in (3.53) with $R_{\rm cyl}^{\parallel}$ given by (3.87). The use of (3.53) rather than (3.86) pays tribute to the fact that the volumes of spheroid and cylinder of the same length ℓ are different, and guarantees the exact dipole moment for the spheroid as $\omega \to \infty$.

3.2.4 Numerical implementation and results

For the numerical results below, the infinite systems of equations (3.41) and (3.81) are truncated so that $m, n \leq 35$. The same truncation is used in the evaluation of the infinite series in (3.42). The problem is then solved by performing a singular-value decomposition of the resulting square system matrix [103], in order to guard ourselves against possible ill conditioning. For the associated Legendre functions with real argument and their first derivatives we use the routines published in [77]. The auxiliary function (3.79) is evaluated using a Gauss-Legendre quadrature [104] with 50 points on the interval $0 < \eta < 1$.

It is of advantage to solve (3.41) for the product $A_{2n-1}\, \mathrm{R}_{1(2n-1)}^{(1)}$ rather than for A_{2n-1} [note that knowing the product is sufficient for evaluating (3.42)]. This helps

prevent overflows as c_1 grows larger, by balancing the exponential growth of $T_{1(2n-1)}$ with that of $\mathrm{R}^{(1)}_{1(2n-1)}$ [see also (3.59) and (3.60)]. The growing exponentials can be canceled explicitly by making use of exponential scaling when computing the spherical Bessel functions with complex argument [105] that are required in the expansion (3.57). A similar expansion is used for the derivative of the radial wavefunction with respect to ξ where the derivative of the Bessel function is eliminated by using the appropriate recurrence relation [83]. [Note that similar growing exponentials can and should be canceled also from (3.87).] We keep 35 terms of both infinite series in (3.57). The expansion coefficients $\mathrm{d}^{1(2n-1)}_{2m-2}$ are obtained with the help of a complex version of the corresponding real routine in [77] where we compute sequences of length 45; note that the normalization of the coefficients requires another truncation of an infinite series [81]. The complex spheroidal eigenvalues required for the computation of the expansion coefficients, finally, are obtained using Hodge's method [106] where the characteristic values of a tridiagonal, complex symmetric matrix of size 40×40, ordered as a sequence with increasing real parts, are computed using a standard high-performance linear algebra routine [103]. One advantage of this approach is that no initial estimates of the eigenvalues are required [107, 108].

The numerical results are plotted vs. induction number

$$|k_1|a = \frac{2a}{d}\,|c_1| \tag{3.90}$$

that, when the product $\omega\,\mu_1\,\sigma_1$ in (3.12) is real, is given by

$$|k_1|a = a\sqrt{\omega\,\mu_1\,\sigma_1} \tag{3.91}$$

in which case

$$c_1 = \frac{d\sqrt{\mathrm{i}}}{2a}\,|k_1|a \tag{3.92}$$

The induction number $|k_1|a$ is related to the skin depth δ_{skin} by

$$|k_1|a = \frac{a\sqrt{2}}{\delta_{\text{skin}}} \tag{3.93}$$

In Fig. 3-2 to 3-7 the computed real and imaginary parts of the polarizability factor $R^{\parallel}_{\text{pro}}$ are shown separately, as a function of $|k_1|a$ and with the elongation $\ell/2a$ as parameter. Fig. 3-2 and 3-3 are for a relative permeability μ_1/μ of 1 and 10, respectively. Fig. 3-4 and 3-6 are for $\mu_1/\mu = 100$, while in Fig. 3-5 and 3-7 we have $\mu_1/\mu = 1000$.

The solid curves in Fig. 3-2 to 3-7 were obtained from (3.41), (3.42). These curves are truncated at that point where the numerical implementation of the expansion of the spheroidal wavefunctions into spherical harmonics is found to break down abruptly. The breakdown point occurs at a smaller induction number $|k_1|a$ for a larger elongation $\ell/2a$ (the curves shown are for $\ell/2a$ =1, 1.5, 2, 4, 6, 8, and 10, respectively) but depends little on relative permeability μ_1/μ (note the extended range of induction numbers in Fig. 3-5 and 3-7). In the spherical limit, $\ell/2a \to 1$, no such breakdown occurs and the results can be shown to be in agreement with the magnetic polarizability factor R_{sph} for conducting and permeable spheres of radius a, given by [59]–[63]

$$R_{\text{sph}} = -\frac{(2\mu_1 + \mu)\,(1 - k_1 a\,\cot k_1 a) - \mu\,(k_1 a)^2}{(\mu_1 - \mu)\,(1 - k_1 a\,\cot k_1 a) + \mu\,(k_1 a)^2} \tag{3.94}$$

The real and imaginary parts of the polarizability factor R_{sph} are illustrated in Fig. 3-8, as a function of $|k_1|a$ and with the relative permeability μ_1/μ as parameter.

The dash-dotted curves in Fig. 3-2 to 3-7 were computed from (3.87) and can be considered as an approximation of $R^{\parallel}_{\text{pro}}$ as $\ell/2a \to \infty$. They provide an important check of the behavior of the results as $\ell/2a$ grows larger.

Since the low-frequency limit (3.67) extends to larger induction numbers as μ_1/μ increases (Section 3.2.1), the solid curves in Fig. 3-4 to 3-7 break off earlier than desirable and were complemented with results from two approximate solutions of the

boundary value problem, shown as dashed curves. The results from the asymptotic closed-form solution (3.63) used for Fig. 3-4 and 3-5 exhibit the unacceptable behavior mentioned in Section 3.2.2; these plots are intended only as an illustration of what is described there. The dashed curves in Fig. 3-6 and 3-7 were obtained from (3.81). We can see that here the low-frequency results (solid curves) are indeed extended to the high-frequency regime. The match in the overlap region is better for smaller $\ell/2a$ and larger μ_1/μ. In contrast to the results in Fig. 3-4(b) and 3-5(b), as $\ell/2a$ increases, the minimum of the imaginary part of $R_{\text{pro}}^{\parallel}$ in Fig. 3-6(b) and 3-7(b) moves down into and towards the center of the trough representing the case $\ell/2a \to \infty$ (dash-dotted lines). Evidently, for highly permeable spheroids, (3.81) provides a *broadband* approximation of the induced magnetic dipole moment, computable without resorting to numerical implementations of the spheroidal wavefunctions and related quantities (expansion coefficients, eigenvalues). In general, independent of permeability, we expect (3.81) to yield accurate results when the skin depth is small compared to the radius of curvature everywhere along the surface of the spheroid, i. e.,

$$\delta_{\text{skin}} < \epsilon\, r_{\min} \tag{3.95}$$

where

$$r_{\min} = a\,\frac{2a}{\ell} \tag{3.96}$$

is the radius of curvature at the poles of the spheroid and, e. g., $\epsilon = 1/10$. Thus

$$|k_1|a > \frac{\sqrt{2}}{\epsilon}\,\frac{\ell}{2a} \tag{3.97}$$

is required.

All curves plotted exhibit the expected general behavior of the real part of $R_{\text{pro}}^{\parallel}$ that transits monotonically from the non-positive low-frequency limit (3.67) to the positive high-frequency limit (3.55); the low-frequency limit decreases and approaches

$-\chi_m = -(\mu_1/\mu - 1)$ as $\ell/2a$ increases. The imaginary part of $R^{\parallel}_{\text{pro}}$ vanishes as $\omega \to 0, \infty$ and passes through a single minimum in between. The location of the minimum moves to smaller induction numbers as $\ell/2a$ increases and its absolute value increases, with a rate that is greater for larger permeability of the spheroid. The results show that the bandwidth of this minimum, for a permeable spheroid, decreases as the elongation $\ell/2a$ increases, with practical consequences pointed out in Section 3.3.3.

Since $R^{\parallel}_{\text{pro}}$ for $\mu_1/\mu = 1$ (Fig. 3-2) is found to be a relatively weak function of the elongation $\ell/2a$, in this case we can obtain a closed-form approximation of the induced magnetic dipole moment by replacing $R^{\parallel}_{\text{pro}}$ in (3.53) by R_{sph} given by (3.94). Note that the normalizing factor in (3.53) depends on $\ell/2a$ but is frequency-independent and given in terms of elementary functions.

In addition to observing the reasonable behavior of the above results under variation of the parameters $\ell/2a$ and μ_1/μ, we validated the numerical implementation of our analytical solutions by comparing with results from MAS [58] (body-of-revolution code) and the approaches described in [57, 66, 67]. The evaluation of the spheroidal wavefunctions and related quantities was verified against tabulated data in [77, 107, 109].

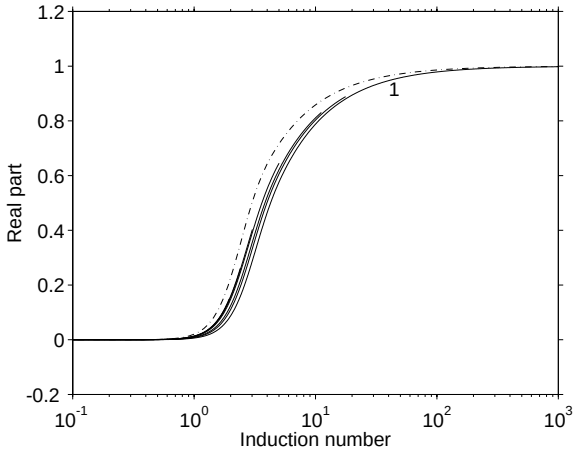

(a) Real part.

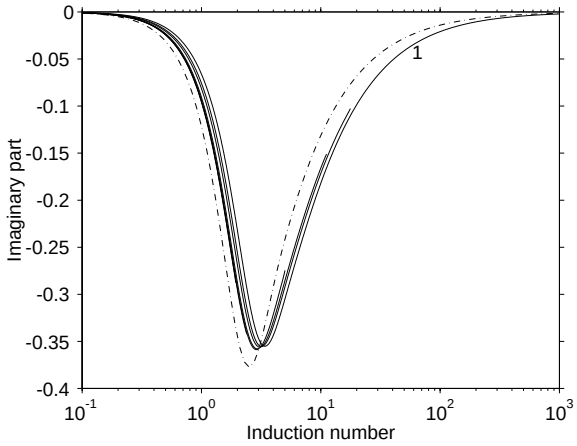

(b) Imaginary part.

Figure 3-2: The magnetic polarizability factor $R^{\parallel}_{\rm pro}$ for conducting and permeable prolate spheroids under axial excitation as a function of the induction number $|k_1|a$ for various elongations $\ell/2a$ and fixed relative permeability $\mu_1/\mu = 1$, shown as solid curves where the evaluation based on the formulation with expanded spheroidal wavefunctions is possible. The dash-dotted curves represent the corresponding $R^{\parallel}_{\rm cyl}$ for long circular cylinders given in terms of Bessel functions. The solid curves are for $\ell/2a = 1$, 1.5, 2, 4, 6, 8, 10 and break off the earlier the more elongated the spheroid.

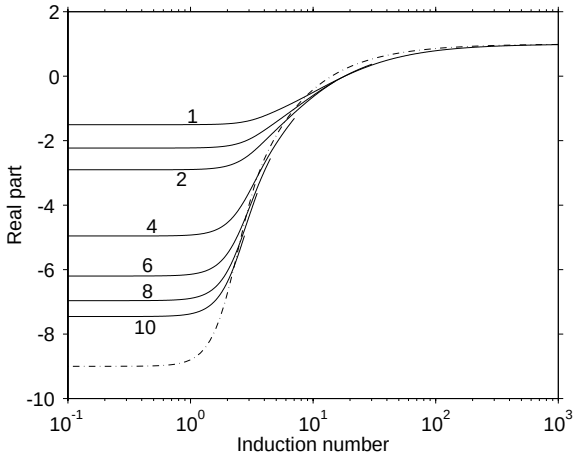

(a) Real part.

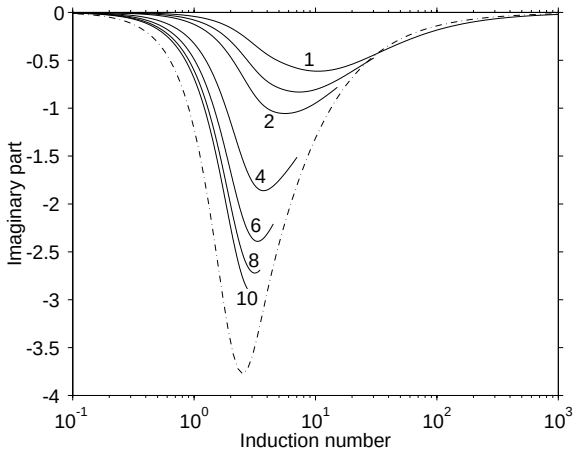

(b) Imaginary part.

Figure 3-3: Similar to Fig. 3-2 but for a relative permeability of $\mu_1/\mu = 10$.

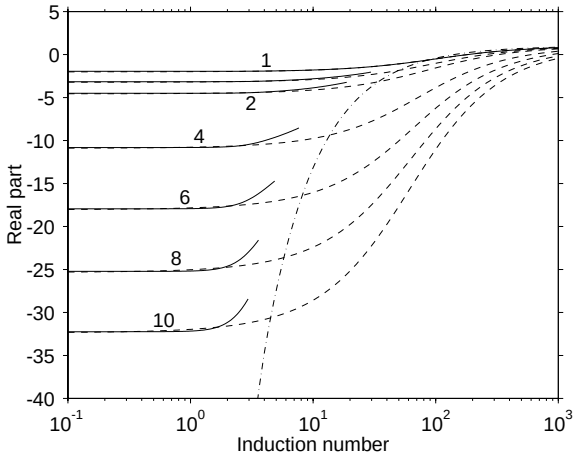

(a) Real part.

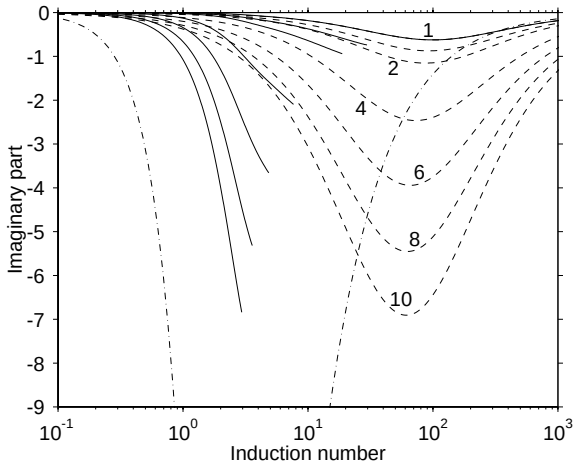

(b) Imaginary part.

Figure 3-4: The solid and dash-dotted curves are similar to those in Fig. 3-2 but for a relative permeability of $\mu_1/\mu = 100$. The dashed curves are obtained from an asymptotic solution to the boundary value problem, equation (3.63), and are shown for the same elongations as the solid curves, i. e., $\ell/2a = 1$, 1.5, 2, 4, 6, 8, 10. It is seen that, in general, this asymptotic solution does not provide a satisfactory broadband approximation.

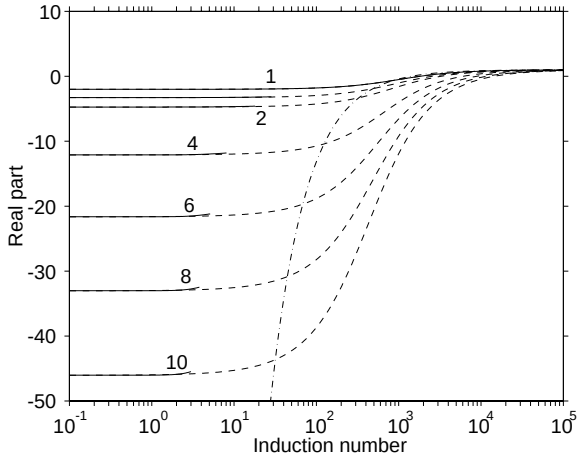

(a) Real part.

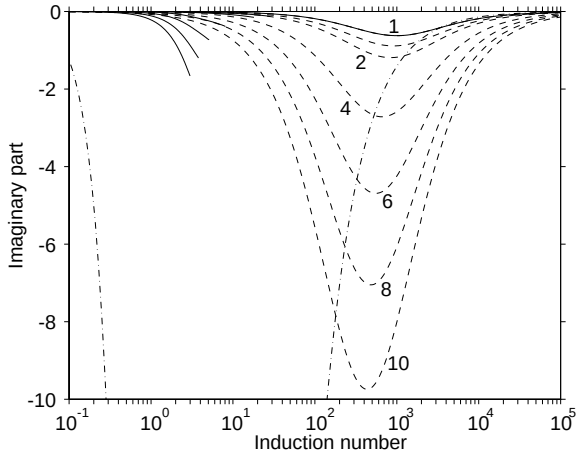

(b) Imaginary part.

Figure 3-5: Similar to Fig. 3-4 but for a relative permeability of $\mu_1/\mu = 1000$.

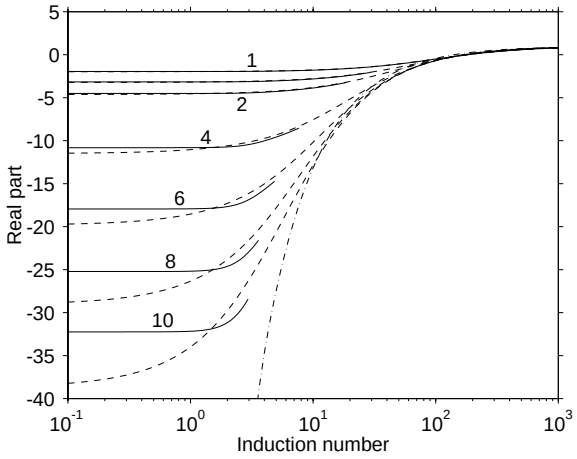

(a) Real part.

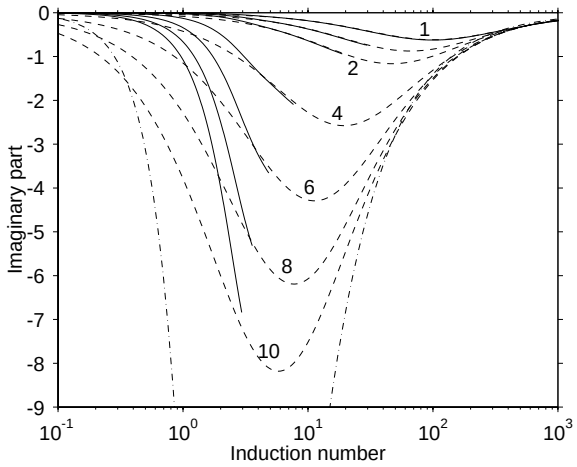

(b) Imaginary part.

Figure 3-6: Similar to Fig. 3-4 but for an improved, approximate solution to the boundary value problem obtained from the infinite system of equations (3.81).

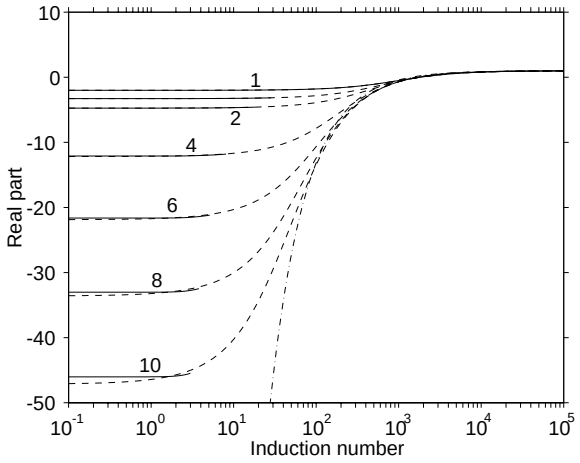

(a) Real part.

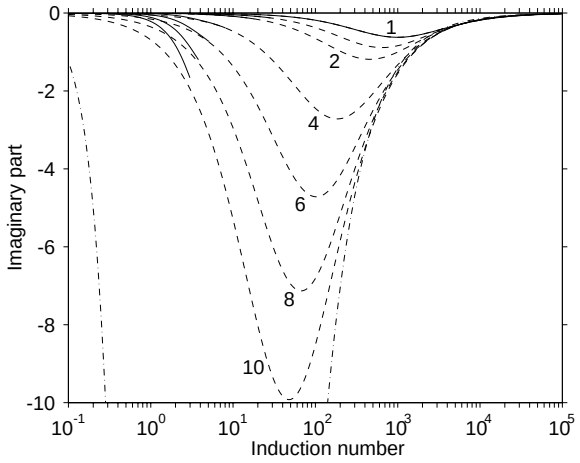

(b) Imaginary part.

Figure 3-7: Similar to Fig. 3-6 but for a relative permeability of $\mu_1/\mu = 1000$.

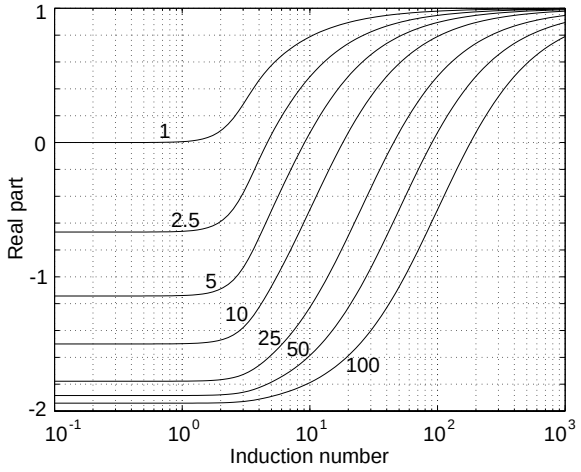

(a) Real part.

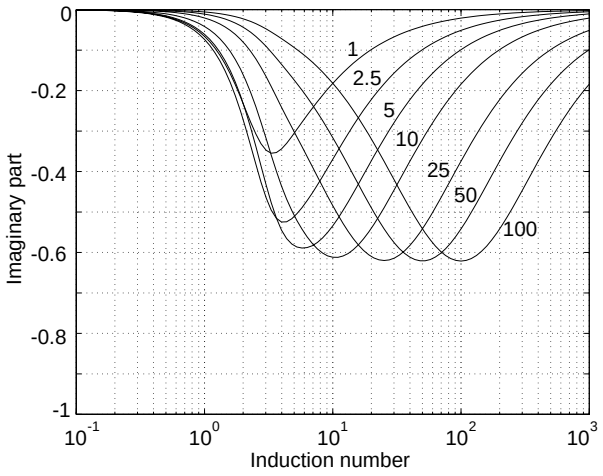

(b) Imaginary part.

Figure 3-8: The magnetic polarizability factor R_{sph} for conducting and permeable spheres as a function of the induction number $|k_1|a$ for various relative permeabilities $\mu_1/\mu = 1$.

3.2.5 Broadband rational function approximation

We have seen above that it is possible to obtain numerical results for $R^{\parallel}_{\mathrm{pro}}$ from $\omega = 0$ up to a certain frequency ω_L and from some ω_H up to arbitrarily high frequencies. If $\omega_L < \omega_H$ the two data sets do not overlap and a gap for $\omega_L < \omega < \omega_H$ remains. To address this issue, we approximate an arbitrary polarizability factor by a rational function R with M simple poles and in the form of partial fractions, given by

$$R = 1 - \sum_{m=1}^{M} \frac{r_m}{1 - \mathrm{i}\omega/\omega_m} \tag{3.98}$$

where the ω_m are corner frequencies to be determined. The residues r_m satisfy

$$\sum_{m=1}^{M} r_m = 1 - R_0 \tag{3.99}$$

where the low-frequency limit R_0 may be known in closed form from the corresponding magnetostatic problem, c. f., (3.67). Note that automatically $R \to 1$ as $\omega \to \infty$ and the model is forced-stable if $\omega_m > 0$. Once available, R lends itself to rapid evaluation in the frequency domain. Furthermore, simulations in the time domain can be carried out using recursive convolution [110, 111].

A general physical justification of the model (3.98) is given by the singular expansion method (SEM) for the representation of magnetic polarizability tensors [51]. For the example of conducting and permeable spheres, (3.94) can be cast into the form of (3.98) with $M \to \infty$. For a sphere with $\mu_1/\mu = 1$ we have explicitly

$$r_m = \frac{6}{m^2\pi^2} \tag{3.100}$$

and

$$\omega_m = \frac{m^2\pi^2}{a^2\mu_1\sigma_1} \tag{3.101}$$

For given discrete data $R(\omega)$ and a fixed M, we can find the ω_m and r_m from the

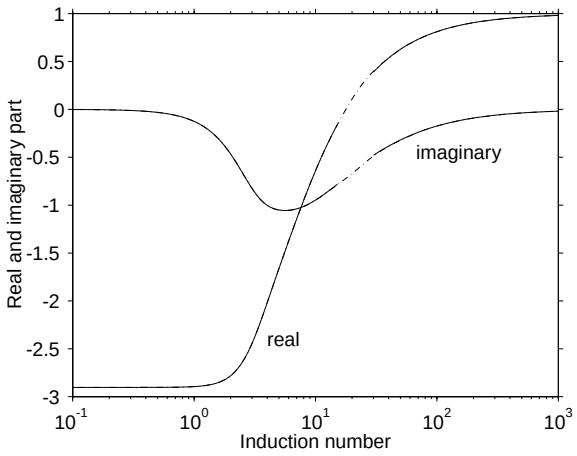

Figure 3-9: Bridging the gap: The dash-dotted curves are obtained from a broadband rational function approximation that matches the solution based on the formulation with expanded spheroidal wavefunctions at the low-frequency end and connects to an approximate solution to the boundary value problem, obtained from the infinite system of equations (3.81), at the high-frequency end (relative permeability $\mu_1/\mu = 10$, elongation $\ell/2a = 2$).

solution of the nonlinear least-squares problem corresponding to (3.98) and with the linear constraint (3.99), employing standard numerical optimization procedures [112]. The elements of the Jacobian are found from (3.98) and given analytically by

$$\frac{\partial R}{\partial r_m} = -\frac{1}{1 - \mathrm{i}\omega/\omega_m} \tag{3.102}$$

and

$$\frac{\partial R}{\partial \omega_m} = \frac{\mathrm{i}\omega}{\omega_m^2} \frac{r_m}{(1 - \mathrm{i}\omega/\omega_m)^2} \tag{3.103}$$

For simplicity, we suggest using a large model order, e. g., $M = 20$, and, as initial guess, distributing the ω_m uniformly on logarithmic scale. This will lead to an accurate fit. If necessary for computational efficiency later, model-order reduction techniques can be employed subsequently.

For the example of a spheroid with $\ell/2a = 2$ and $\mu_1/\mu = 10$, the broadband approximation technique is demonstrated in Fig. 3-9. The data and the computed fit

Ω_m	r_m
0.57336775	0.00893504
0.68717870	−0.01765579
1.08104558	0.55242835
1.09597193	0.62921047
1.52262472	0.61281997
1.86128484	0.59985085
2.15075227	0.38267186
2.59394897	0.57777318
2.95175855	0.03483243
3.30652352	0.24768079
3.68787442	0.06261377
4.05133138	0.09210828
4.42138568	0.02847170
4.78941051	0.04177010
5.15788079	0.00760386
5.52634515	0.02505605
5.89476708	−0.00674325
6.26318930	0.02343928
6.63162237	−0.01539648
7.00012805	0.01558614

Table 3.1: Normalized corner frequencies and residues for the least-squares fit in Fig. 3-9.

are plotted as solid and dash-dotted curves, respectively, overlying each other. The low-frequency portion of the data is as in Fig. 3-3. The high-frequency part was computed from (3.81) and here (3.97) with $\epsilon = 1/10$ holds. The $M = 20$ corner frequencies ω_m and residues r_m are listed in Table 3.1 where

$$\Omega_m = \log_{10}(a^2 \mu_1 \sigma_1 \, \omega_m) \tag{3.104}$$

The largest absolute mismatches of the fit shown in Fig. 3-9 occur at the low-frequency end of the high-frequency approximation and are less than 8×10^{-3} (0.8 % of the high-frequency limit) for both real and imaginary part, as can be seen from the plot of the mismatch vs. induction number in Fig. 3-10.

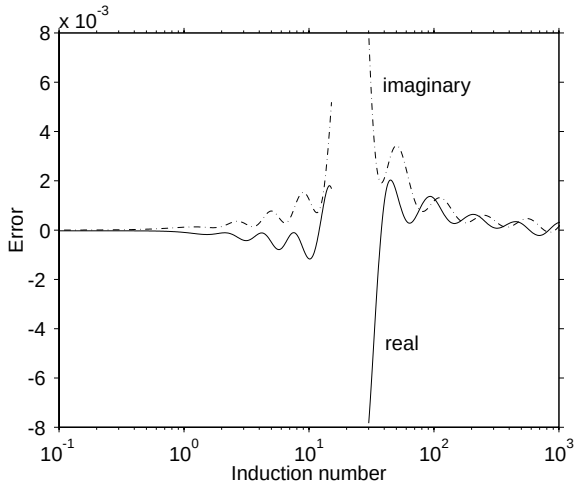

Figure 3-10: The mismatch of the fit in Fig. 3-9.

3.3 Magnetoquasistatic response of a distribution of small objects

The development in Section 3.2 above is concerned with the characterization of the magnetoquasistatic response of a single conducting and permeable object of a particular canonical shape. In this section we turn to the question of modeling the broadband response of a collection of objects where the characterization of each individual body is assumed to be given via its frequency-dependent, complex magnetic polarizability tensor. The restriction to small objects leads to a simple many-body theory that is somewhat analogous to a possible treatment of multiple scattering effects in composite dielectric media that consist of particles immersed in a homogeneous background medium (keyword "mixing formulas"). One practical motivation for the investigation of the magnetoquasistatic N-body problem is that areas contaminated with UXO are naturally very rich in metallic pieces from *exploded* ordance. The discriminating capabilities of wideband electromagnetic induction methods could help reducing false alarm rates during field surveying. The basic idea is very simple; smaller pieces

(clutter) lead to a response with larger natural frequency while the electromagnetic induction activity of larger objects (potential targets) is shifted towards lower frequencies. Thus, there is need for a theoretical and numerical model for the total magnetoquasistatic response of a collection of conducting and permeable objects.

3.3.1 Formulation

As in Section 3.2, it is assumed that the frequency is low enough so that displacement currents can be neglected everywhere (magnetoquasistatics). The background medium with homogeneous permeability μ is a poor electric conductor so that the sources for the secondary magnetic fields are located on or within the objects. The fields within the objects are governed by magnetic diffusion. The objects are small enough so that their excitation can be considered as locally uniform. The distances between the objects and between the observation point and the objects are large enough so that only dipolar secondary fields need to be taken into account. Within these approximations, multiple interaction between the objects is included.

The secondary field at $\overline{r} = \overline{r}_m$ due to the n-th small object located at $\overline{r} = \overline{r}_n$ $(m, n = 1, 2, \ldots, N;\, m \neq n)$ and with unknown induced magnetic dipole moment $\overline{m}_n$ is given by [51, 56, 84]

$$\overline{H}_{sn}(\overline{r}_m) = \frac{3\,\hat{r}_{mn}\hat{r}_{mn} - \overline{\overline{I}}}{4\pi\, r_{mn}^3} \cdot \overline{m}_n \tag{3.105}$$

where

$$\hat{r}_{mn} = \frac{\overline{r}_m - \overline{r}_n}{r_{mn}} \tag{3.106}$$

with $r_{mn} = |\overline{r}_m - \overline{r}_n|$ and $\overline{\overline{I}}$ is the identity tensor. The n-th object is characterized by its magnetic polarizability tensor $\overline{\overline{M}}_n$ and we have, with $\overline{H}_0$ the primary magnetic field,

$$\overline{m}_n = \overline{\overline{M}}_n \cdot \left[\overline{H}_0(\overline{r}_n) + \sum_{\substack{k=1 \\ k\neq n}}^{N} \frac{3\,\hat{r}_{nk}\,\hat{r}_{nk} - \overline{\overline{I}}}{4\pi\, r_{nk}^3} \cdot \overline{m}_k\right] \tag{3.107}$$

In words, the response of the n-th object is excited by the superposition of the primary

field and the secondary fields of all the other objects. The exciting field at the location of the object—the effective primary field seen by the scatterer—is projected onto the induced magnetic dipole moment by its characteristic magnetic polarizability tensor. Thus, we find

$$\overline{m}_n - \overline{\overline{M}}_n \cdot \sum_{\substack{k=1 \\ k\neq n}}^{N} \frac{3\,\hat{r}_{nk}\,\hat{r}_{nk} - \overline{\overline{I}}}{4\pi\, r_{nk}^3} \cdot \overline{m}_k = \overline{\overline{M}}_n \cdot \overline{H}_0(\overline{r}_n) \tag{3.108}$$

which represents a $3N \times 3N$ system of scalar linear equations for the components of $\overline{m}_n$. The coefficients involving $\overline{\overline{M}}_n$ are in general complex due to the magnetic diffusion effects in the objects. Leaving out the sum in (3.108) corresponds to neglecting any interaction between the objects, i. e.,

$$\overline{m}_n \approx \overline{\overline{M}}_n \cdot \overline{H}_0(\overline{r}_n) \tag{3.109}$$

It is seen that this is justified if the r_{nk} are much larger than the largest characteristic object dimension.

Given the $\overline{m}_n$, the total magnetic field is found from

$$\overline{H}(\overline{r}) = \overline{H}_0(\overline{r}) + \sum_{k=1}^{N} \frac{3\,\hat{r}_{0k}\hat{r}_{0k} - \overline{\overline{I}}}{4\pi\, r_{0k}^3} \cdot \overline{m}_k \tag{3.110}$$

where

$$\hat{r}_{0k} = \frac{\overline{r} - \overline{r}_k}{r_{0k}} \tag{3.111}$$

with $r_{0k} = |\overline{r} - \overline{r}_k|$.

The similarity of this formulation with the Foldy-Lax theory of multiple wave scattering is pointed out [27].

The magnetic polarizability tensor for a sphere with radius a, permeability μ_1, and conductivity σ_1 is given by

$$\overline{\overline{M}}_{\text{sph}} = -2\pi a^3 R_{\text{sph}}\, \overline{\overline{I}} \tag{3.112}$$

where the classical solution for $R_{\rm sph}$ is as in (3.94) and plotted vs. induction number $|k_1|a$ in Fig. 3-8 above.

3.3.2 Simulation

As an example we consider the configuration in Fig. 3-11 with measures and material parameters as indicated. A larger sphere is surrounded by five vertically stacked rings of a total of 125 smaller spheres with a collective volume equal to that of the large sphere. Although the radii of the spheres are in general not much smaller than the inter-object spacings, in the sense of our dipole formulation all objects, including the large sphere, are considered to be small. The primary field

$$\overline{H}_0 = \hat{z}\, H_{0z} \tag{3.113}$$

is in the direction of the rotational symmetry axis and assumed to be uniform. For all results in this simulation, the observation point is on the rotational symmetry axis at a distance of 1 m from the center of the configuration and the secondary magnetic field component in direction of the primary field is obtained, divided by the primary field amplitude H_{0z}, and shown decomposed into real and imaginary parts (in-phase and quadrature components).

The purpose of the simulation is to investigate if a measurement of the secondary magnetic field for various frequencies could provide information helping in the decision if a larger target (UXO) is present among the smaller objects (clutter). Note that a simple metal detector indicating, say, total metal volume could not be used to discriminate the target from the collective clutter even if the two were encountered in absence of each other.

Fig. 3-12 shows the response of the large sphere in the absence of the small spheres in the non-magnetic case, $\mu_1/\mu = 1$, and for $\mu_1/\mu = 100$. The effect of the larger permeability is, beside producing a positive DC secondary field, to spread out the

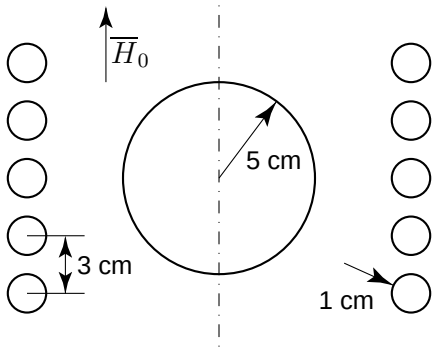

(a) Side view.

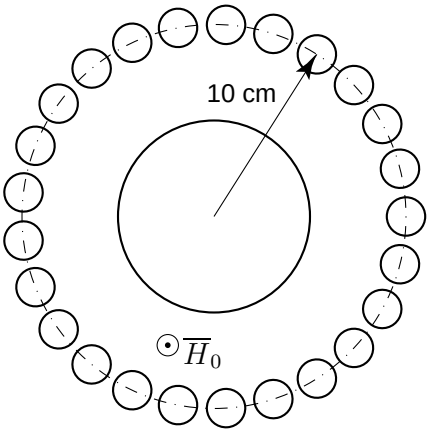

(b) Top view.

Figure 3-11: Collection of conducting and permeable objects: a central large sphere and vertically stacked rings of small spheres. The conductivity of all objects is $\sigma_1 = 10^7\,\mathrm{S/m}$ and the relative permeability μ_1/μ either 1 or 100.

frequency response and shift the maximum of the imaginary part (natural frequency) to higher frequencies. A similar observation is made in Fig. 3-13 for the collection of 125 small spheres as in Fig. 3-11, but without the central large sphere. Due to the smaller dimension of the individual objects in this case the general activity is shifted to higher frequencies. From the comparison of the solid and dash-dotted lines it is seen that the interaction between the small spheres is weak. Note that a horizontal or vertical alignment of objects has an opposite effect in reinforcing or weakening the primary field so that in the present case a partial compensation of the secondary fields at the locations of the small spheres is expected.

Fig. 3-14 shows the result when all objects in Fig. 3-11 are present simultaneously. We find that in the non-magnetic case [Fig. 3-14(a)] two maxima in the imaginary part and three turning points in the real part are visible. Clearly, this set of curves indicates the existence of two distinct length scales in the ensemble of objects. The target (the larger sphere) stands out from the wideband frequency response and is not obscured by the presence of the clutter. For the practically important magnetic case as shown in Fig. 3-14(b), however, the situation is quite different. The result obtained is qualitatively similar to Fig. 3-12(b) and 3-13(b), with only one maximum in the imaginary part. The two different length scales produce a featureless, broad collective response, making it more difficult to identify the sizes of the individual objects that contribute to the total response.

3.3.3 Measurement

In a spirit similar to the simulation in Section 3.3.2 above, an electromagnetic induction measurement was set up. However, here we consider non-spherical, real-life objects that could be encountered in the field. As before, a larger target is surrounded by a number of smaller, identical objects that collectively produce a response which is comparable in maximum amplitude to that of the central target.

Specifically, the configuration consists of a 20 mm diameter deactivated UXO

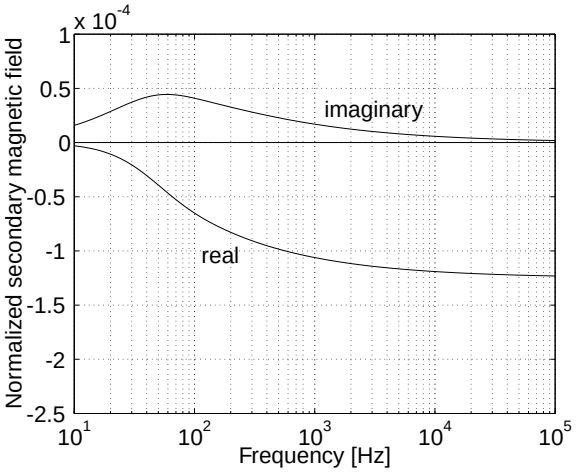

(a) $\mu_1/\mu = 1$.

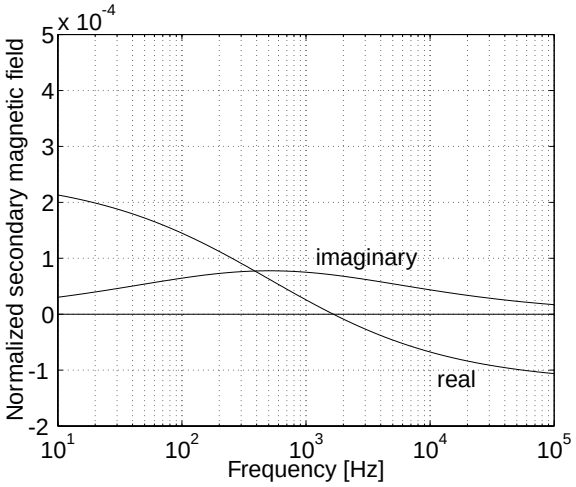

(b) $\mu_1/\mu = 100$.

Figure 3-12: Secondary magnetic field due to the central large sphere in the absence of the small spheres.

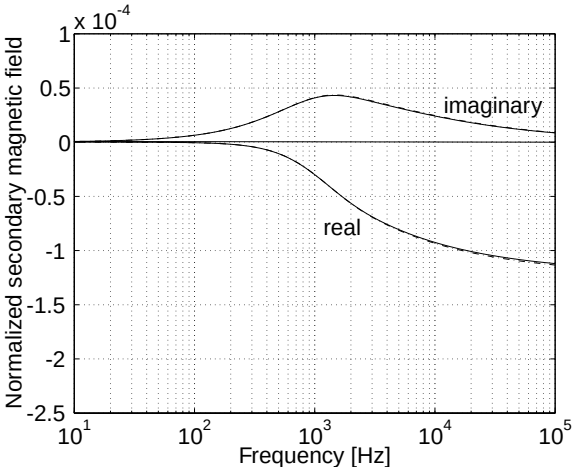

(a) $\mu_1/\mu = 1$.

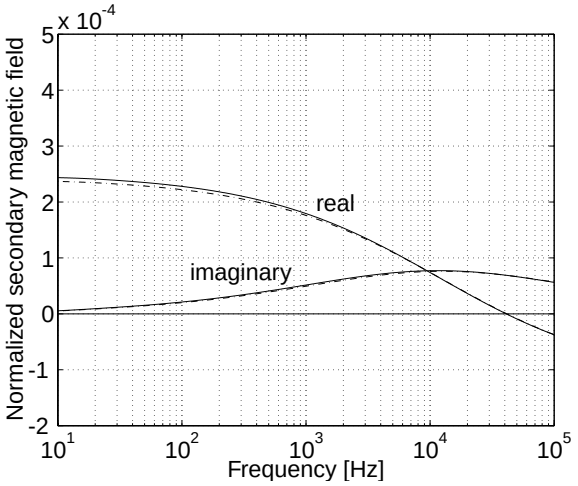

(b) $\mu_1/\mu = 100$.

Figure 3-13: Secondary magnetic field due to the vertically stacked rings of small spheres in the absence of the central large sphere (interaction neglected for the dash-dotted lines).

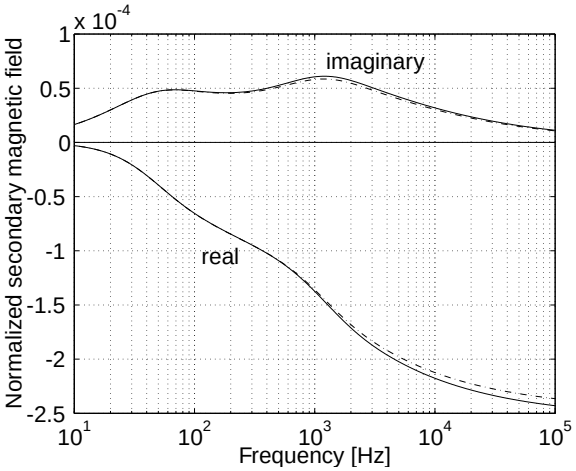

(a) $\mu_1/\mu = 1$.

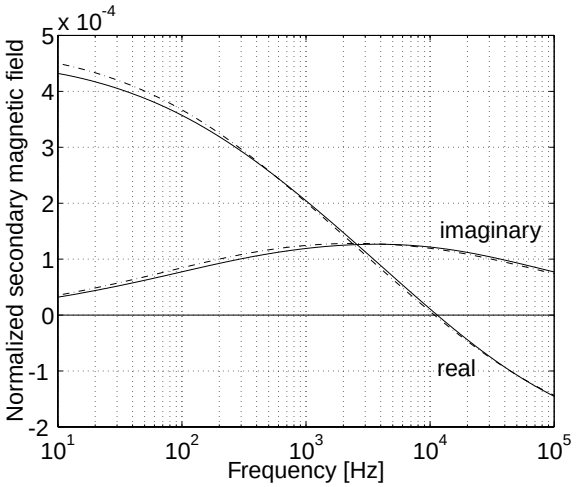

(b) $\mu_1/\mu = 100$.

Figure 3-14: Secondary magnetic field due to central large sphere surrounded by vertically stacked rings of small spheres (interaction neglected for the dash-dotted lines).

(length 7.62 cm) in an upright position (nose down), surrounded by 57 commercial finishing nails (steel, diameter 0.182 cm, length 3.81 cm). The nails were approximately aligned with the primary field and the axis of the shell. They were arranged roughly equally spaced throughout a disk of 5.6 cm diameter with the shell at its center. Although not entirely randomly distributed, the clutter in the corresponding situation in the field could be present because once "somebody dropped a box of nails."

In order to minimize interference from nearby metallic objects, the experiment was performed outdoors using a wooden rig and styrofoam to hold the sensor and objects. Averaged measurements of the background secondary field were subtracted from averaged measurements with the objects in place.

For a description of the sensor itself reference is made to [53]. We just mention here that coils producing the primary field are arranged in such a way that the primary field at the center of the coils inside the sensor is weak. This is where the secondary field is measured with maximized sensitivity. Outside the sensor, in a limited region far enough from the coils, the primary field is nearly uniform as desired.

The data shown in Fig. 3-15 are for the shell without any nails and for the nails in absence of the shell, respectively. It is seen that the shell produces a broad low-frequency response (with the maximum imaginary part at a frequency lower than the lowest frequency measured) while the collection of nails exhibits a maximum in the imaginary part at about 7 kHz. Due to the rapid decay of the quadrature response of the nails towards low frequencies, when the shell and nails are present at the same time (see the results in Fig. 3-16) two maxima in the imaginary part of the response are formed, similar to the situation in Fig. 3-14(a) which, however, is for non-magnetic objects.

Thus, different from the simulation with permeable spherical objects with the total response shown in Fig. 3-14(b), here the target is not obscured by the clutter, although all objects are ferrous. It appears then that the large elongation of the nails in the experiment ($\ell/2a \approx 20.9$) could be responsible for this effect. In Section 3.2.4, we

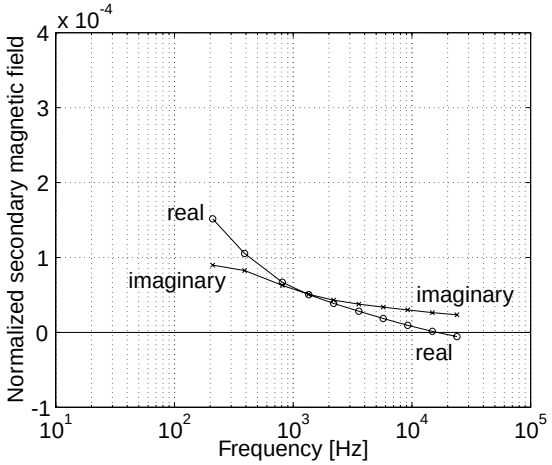

(a) 20 mm shell.

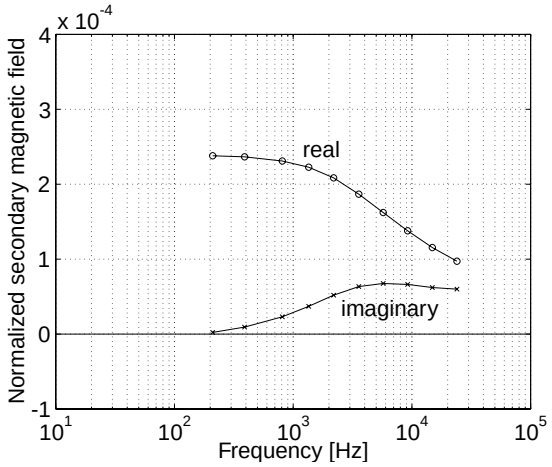

(b) Nails.

Figure 3-15: Measured secondary magnetic field due to 20 mm shell and finishing nails, each in absence of the other.

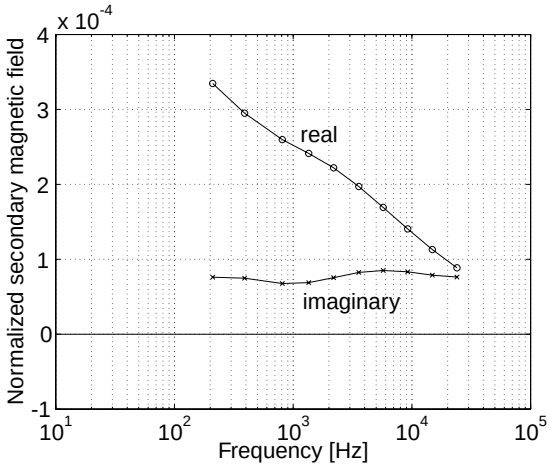

Figure 3-16: Measured secondary magnetic field due to 20 mm shell surrounded by finishing nails.

have verified the more narrow-band character of the response of elongated permeable objects with the help of the numerical implementation of our analytical solutions for prolate spheroids under axial excitation. This is an interesting, simple example of how these solutions can assist the understanding and interpretation of practical broadband electromagnetic induction measurements. The theory and methods of Section 3.2 could further be used in an attempt to model the measurement described here quantitatively, provided the shell and nails can be represented accurately enough by prolate spheroids. Difficulties could arise from the uncertainty about the values of the permeabilities of the objects and from the nonlinear character of ferromagnetic materials such as steel [51].

3.4 Magnetoquasistatic response of objects of arbitrary shape

We derive here equivalent surface-surface, volume-surface, and volume-volume formulations for the magnetic dipole moment of conducting and permeable objects of

arbitrary shape. The results can be used for reference in a variety of derivations, both with theoretical and numerical goal (for an example see Section 3.2.3).

Consider a homogeneous and isotropic body of a certain conductivity and permeability μ_1 in a homogeneous, isotropic, and non-conducting medium of permeability μ. The body occupies the region V_1 with surface S_1 and $\hat{n}$ denotes the unit normal vector on S_1 pointing into the background medium, region V_2. The total fields everywhere are assumed to be known.

According to the equivalence principle [28], the secondary fields in V_2 can be thought of being due to the fictitious electric surface current $\hat{n} \times \overline{H}$ and the fictitious magnetic surface current $-\hat{n} \times \overline{E}$, both on S_1 across which these quantities are continuous. Electric loop currents and magnetic currents with non-zero divergence, the latter leading to magnetic charge accumulations, both contribute to the dipole moment [84] of the body, expressed as

$$\overline{m} = \frac{1}{2} \int\limits_{S_1} \mathrm{d}S\, \overline{r} \times (\hat{n} \times \overline{H}_2) + \frac{1}{\mathrm{i}\omega\mu} \int\limits_{S_1} \mathrm{d}S\, \overline{r}\, \nabla_s \cdot (-\hat{n} \times \overline{E}_2) \tag{3.114}$$

For relations involving the surface nabla operator ∇_s see Appendix 2 in [61]. Noting that

$$\begin{aligned}
\mathrm{i}\omega\mu\, \hat{n} \cdot \overline{H}_2 &= \hat{n} \cdot (\nabla \times \overline{E}_2) && (3.115)\\
&= \hat{n} \cdot \left[\left(\nabla_s + \hat{n} \frac{\partial}{\partial n} \right) \times \overline{E}_2 \right] && (3.116)\\
&= \hat{n} \cdot (\nabla_s \times \overline{E}_2) && (3.117)\\
&= \nabla_s \cdot (\overline{E}_2 \times \hat{n}) + \overline{E}_2 \cdot (\nabla_s \times \hat{n}) && (3.118)\\
&= \nabla_s \cdot (-\hat{n} \times \overline{E}_2) && (3.119)
\end{aligned}$$

we find from (3.114)

$$\overline{m} = \frac{1}{2} \int\limits_{S_1} \mathrm{d}S\, \overline{r} \times (\hat{n} \times \overline{H}_2) + \int\limits_{S_1} \mathrm{d}S\, \overline{r}\, \hat{n} \cdot \overline{H}_2 \tag{3.120}$$

Considering the Maxwell equations $\nabla \times \overline{H} = \overline{J}$ and $\nabla \cdot \overline{H} = -\overline{H} \cdot (\nabla\mu)/\mu$, we can alternatively view the dipole moment as being produced by the physical electric volume currents circulating in the body and fictitious magnetic surface charges at the surface of discontinuity of μ, i. e., S_1. In this picture we write

$$\overline{m} = \frac{1}{2} \int\limits_{V_1} \mathrm{d}V\, \overline{r} \times \overline{J}_1 + \int\limits_{S_1} \mathrm{d}S\, \overline{r}\, \hat{n} \cdot (\overline{H}_2 - \overline{H}_1) \tag{3.121}$$

In the following we show that (3.121) and (3.120) are indeed equivalent. Using

$$\begin{aligned}
\nabla(\overline{r} \cdot \overline{H}_1) &= (\overline{r} \cdot \nabla)\, \overline{H}_1 + (\overline{H}_1 \cdot \nabla)\, \overline{r} \\
&\quad + \overline{r} \times (\nabla \times \overline{H}_1) + \overline{H}_1 \times (\nabla \times \overline{r}) && (3.122)\\
&= \overline{r} \cdot \nabla\, \overline{H}_1 + \overline{H}_1 + \overline{r} \times \overline{J}_1 && (3.123)\\
&= \nabla \cdot (\overline{r}\, \overline{H}_1) - 2\, \overline{H}_1 + \overline{r} \times \overline{J}_1 && (3.124)\\
&= \nabla \cdot (\overline{r}\, \overline{H}_1) - 2\, \nabla \cdot (\overline{H}_1\, \overline{r}) + \overline{r} \times \overline{J}_1 && (3.125)
\end{aligned}$$

and two Gauss-type integral identities, (3.121) becomes

$$\overline{m} = \frac{1}{2} \int\limits_{S_1} \mathrm{d}S\, \hat{n}\, \overline{r} \cdot \overline{H}_1 - \frac{1}{2} \int\limits_{S_1} \mathrm{d}S\, \hat{n} \cdot \overline{r}\, \overline{H}_1 + \int\limits_{S_1} \mathrm{d}S\, \hat{n} \cdot \overline{H}_1\, \overline{r} + \int\limits_{S_1} \mathrm{d}S\, \overline{r}\, \hat{n} \cdot (\overline{H}_2 - \overline{H}_1) \tag{3.126}$$

which, after combining the third and fourth term, is seen to be same as (3.120).

Through (3.120) one obtains $\overline{m}$ from surface integration while (3.121) is the sum of a volume and a surface integral. With χ_m as in (3.83), we can rewrite (3.121) as

$$\begin{aligned}
\overline{m} &= \frac{1}{2} \int\limits_{V_1} \mathrm{d}V\, \overline{r} \times \overline{J}_1 + \chi_m \int\limits_{S_1} \mathrm{d}S\, \overline{r}\, \hat{n} \cdot \overline{H}_1 && (3.127)\\
&= \frac{1}{2} \int\limits_{V_1} \mathrm{d}V\, \overline{r} \times \overline{J}_1 + \chi_m \int\limits_{V_1} \mathrm{d}V\, \nabla \cdot (\overline{H}_1\, \overline{r}) && (3.128)
\end{aligned}$$

which gives the pure volume integral formulation

$$\overline{m} = \frac{1}{2} \int_{V_1} \mathrm{d}V\, \overline{r} \times \overline{J}_1 + \chi_m \int_{V_1} \mathrm{d}V\, \overline{H}_1 \tag{3.129}$$

The second term in (3.129), adding to the dipole moment of the physical eddy currents, can be viewed as arising from the presence of volumetric magnetic "contrast sources."

3.5 Conclusions

By studying the approaches, solutions, and results described above one can gain much insight into the nature of magnetic diffusion into, and low-frequency scattering from, conducting and permeable objects.

In the treatment of the problem of a prolate spheroid under axial excitation, a canonical problem of fundamental importance due to its non-spherical character, we have seen that the exact solution of the boundary value problem based on spheroidal wavefunctions that are expanded in terms of spherical harmonics is directly usable numerically for small to intermediate induction numbers. A fundamental difficulty in this type of magnetoquasistatic problems, however, lies in the complex wavenumbers inside the object that vary over many orders of magnitude. For example, the truncation of the system matrix in Hodge's method for determining the spheroidal eigenvalues (Section 3.2.4) requires that the dimension of the matrix be much larger than $|c_1|$ in (3.90). This limits the applicability of the solution as $|c_1|$ grows exponentially. Furthermore, c_1 grows with equal real and imaginary parts. Thus we engage a much less well-known domain of the spheroidal wavefunctions that may well be freighted with mathematical questions we have not touched upon in the course of our pragmatic development [109, 113]. Obtaining an approximate solution for high frequencies that avoids the necessity of evaluating the spheroidal wavefunctions al-

together teaches the lesson that solving the Helmholtz equation with a reasonable degree of accuracy defies simplification beyond a certain point. The first such asymptotic solution, given in closed form and referring only to functions associated with solutions of Laplace's equation, was found to be inaccurate for the frequencies of interest. However, based on a special thin-skin approximation we were able to construct an infinite system of equations that yields satisfactory results. From the derivation it is apparent that the complexity here stems from the varying local geometry of the boundary. This complication disappears in the limit of a long spheroid and we gave an approximate closed-form solution that relies on Bessel functions rather than spheroidal wavefunctions. For practical purposes, it is important to join low-frequency and high-frequency results together in order to find the broadband response of the spheroid. We realized this by using a straightforward numerical fitting procedure based on rational functions with simple real poles. The partial fractions obtained can also readily be employed in time-domain analyses.

In our study of the magnetoquasistatic response of a collection of small conducting and permeable objects, each individual object is characterized by its complex magnetic polarizability tensor. This complex-valued tensor gives the dipolar response of the object to a locally uniform exciting magnetic field including diffusion effects. Taking mutual interactions into account, a linear system of equations is solved for the vector dipole moments induced in the objects. Thus, the total electromagnetic induction response of the collection of objects is obtained, and the significance of mutual interaction and the influence of spatial distribution and varying parameters of the objects can be studied. With the help of a simulation and a measurement we demonstrated the discriminating capability of broadband electromagnetic induction methods. The results indicate the importance of size, permeability, and elongation of the individual objects in influencing the total response. The effect of the mutual interaction between the objects was found to be numerically small but not necessarily negligible. The interaction between conducting and permeable objects in the magne-

toquasistatic regime is naturally limited due to the rapid $1/r^3$ decay of the secondary dipole fields. Note that an electrodynamic Hertzian dipole produces fields that decay as slowly as $1/r$.

Finally, we derived rigorous expressions of the magnetic dipole moment induced in permeable and conducting objects of arbitrary shape in terms of volume and surface integrals over the total magnetoquasistatic fields. One of the representations forms the basis for a closed-form approximation of the response of a circular cylinder of finite length given in Section 3.2.3 above. These formulas should prove useful in many situations when dealing with problems belonging to the class considered in this chapter.

Chapter 4

An alternative to Tikhonov regularization for deblurring and inverse diffraction

4.1 Introduction

Fields and waves carry information on the distribution of the sources producing them. This phenomenon can be used for "imaging" structures (in a very general sense) that are otherwise inaccessible. However, the nature of field evolution and wave propagation leads to a gradual smearing or blurring of the information and thus to a loss of resolution when moving away from the sources. For practical reasons, it is often impossible to measure the fields as closely to the sources as desired or necessary. It is therefore of interest and importance to study methods that allow us to reverse the blurring process, i. e., to perform deblurring.

We consider a special, convolutional blurring process which depends on a parameter [114, 115]. This parameter is assumed to describe the severity of the smoothing of the data. In an application, it will typically be related to the distance from the sources. As shown in Section 4.2, the restriction to additive blurring implies a class

of kernels which lead to an inherently unstable inverse blurring process. As a possible remedy, in Section 4.3.1 the output least-squares formulation with Tikhonov regularization is described (for references see below). In Section 4.3.2 we introduce a local extrapolation scheme which offers an alternative solution of the deblurring problem.

We then focus in Section 4.4 on various applications of the theory. A glance through the references relating to this chapter shows the highly interdisciplinary nature of the problem. We discuss applications relating to magnetostatics, electrostatics, gravity, and scalar wave diffraction. In numerical examples we compare results based on Tikhonov regularization and the local extrapolation scheme quantitatively.

4.2 Statement of the problem

We assume that the blurring process is described by the convolution

$$\tilde{f}(\overline{\rho},\zeta) = \int_{-\infty}^{\infty} \mathrm{d}\overline{\rho}'\, g(\overline{\rho}-\overline{\rho}',\zeta)\, f(\overline{\rho}') \tag{4.1}$$

with f the undistorted deterministic data, g a blurring kernel, and $\zeta \geq 0$ a parameter describing the degree of distortion. In some applications, $\overline{\rho}$ is usually two-dimensional (as suggested by the notation similar to that often employed when dealing with cylindrical geometries) but this is not required. Irrespective of the actual dimension of $\overline{\rho}$ we will occasionally refer to f and $\tilde{f}$ as "images".

Without loss of generality we choose $\zeta = 0$ to correspond to no distortion such that

$$\tilde{f}(\overline{\rho},0) = f(\overline{\rho}) \tag{4.2}$$

and hence

$$g(\overline{\rho},0) = \delta(\overline{\rho}) \tag{4.3}$$

where δ is the Dirac-delta function.

Further, we require the blurring to be additive in the sense that for any ζ_i, ζ_j with $\zeta_j \geq \zeta_i$

$$\tilde{f}(\overline{\rho}, \zeta_j) = \int_{-\infty}^{\infty} \mathrm{d}\overline{\rho}'\, g(\overline{\rho} - \overline{\rho}', \zeta_j - \zeta_i)\, \tilde{f}(\overline{\rho}', \zeta_i) \tag{4.4}$$

The problem is then to determine $f(\overline{\rho})$ from a given $\tilde{f}(\overline{\rho}, \zeta_0)$ where the actual data may be corrupted by noise. In a typical physical problem, f will be a field distribution of interest which cannot be measured directly but only after having been propagated a distance ζ_0 through space (Section 4.4). The kernel or "propagator" g is assumed to be known and depends on the specific physical situation.

Let $G(\overline{k}_\rho, \zeta)$ denote the Fourier transform of $g(\overline{\rho}, \zeta)$ with respect to $\overline{\rho}$,

$$G(\overline{k}_\rho, \zeta) = \int_{-\infty}^{\infty} \mathrm{d}\overline{\rho}\, \mathrm{e}^{-\mathrm{i}\,\overline{k}_\rho \cdot \overline{\rho}}\, g(\overline{\rho}, \zeta) \tag{4.5}$$

We will use a similar notation for other transformed quantities as well and assume that all Fourier transforms exist.

One is tempted to invert (4.1) by simply considering its equivalent in the frequency domain

$$\tilde{F}(\overline{k}_\rho, \zeta) = G(\overline{k}_\rho, \zeta)\, F(\overline{k}_\rho) \tag{4.6}$$

However, dividing (4.6) by $G(\overline{k}_\rho, \zeta)$ and computing the inverse Fourier transform is an unstable process which can be seen from the following argument.

Taking (4.4) to the frequency domain and inserting (4.6) gives

$$G(\overline{k}_\rho, \zeta_j) = G(\overline{k}_\rho, \zeta_j - \zeta_i)\, G(\overline{k}_\rho, \zeta_i) \tag{4.7}$$

or, equivalently,

$$G(\overline{k}_\rho, \zeta + \Delta\zeta) = G(\overline{k}_\rho, \Delta\zeta)\, G(\overline{k}_\rho, \zeta) \tag{4.8}$$

Subtracting $G(\overline{k}_\rho, \zeta)$ from (4.8), dividing by $\Delta\zeta$, taking the limit as $\Delta\zeta \to 0$, and

noting that (4.3) means

$$G(\overline{k}_\rho, 0) = 1 \tag{4.9}$$

leads to the differential equation

$$\frac{\partial}{\partial \zeta} G(\overline{k}_\rho, \zeta) + G_0'(\overline{k}_\rho)\, G(\overline{k}_\rho, \zeta) = 0 \tag{4.10}$$

where

$$G_0'(\overline{k}_\rho) = -\left[\frac{\partial}{\partial \zeta} G(\overline{k}_\rho, \zeta)\right]_{\zeta=0} \tag{4.11}$$

The obvious solution to (4.10) with the initial condition (4.9) is

$$G(\overline{k}_\rho, \zeta) = \mathrm{e}^{-G_0'(\overline{k}_\rho)\,\zeta} \tag{4.12}$$

Since (4.12) is expected to have low-pass character, $\mathrm{Re}\, G_0'(\overline{k}_\rho)$ can be assumed to be positive and growing for increasingly large $k_\rho = |\overline{k}_\rho|$. Hence the blurring suppresses high-frequency components exponentially. For the inverse problem this means that only for the case of synthetic, noise-free data the above inversion procedure would work, otherwise, the inversion would be unstable due to exponential amplification of noise.

4.3 Methods of solution

4.3.1 Tikhonov regularization

The usual way to circumvent the difficulty associated with a kernel of the form (4.12) is to replace the deconvolution filter $1/G(\overline{k}_\rho, \zeta)$ by one that has a built-in safeguarding against division by exponentially small numbers.

To derive such a filter a cost functional (for a fixed $\zeta = \zeta_0$)

$$C\Big[\hat{F}(\overline{k}_\rho)\Big] = \beta \left[\int\limits_{-\infty}^{\infty} \mathrm{d}\overline{k}_\rho \left| G(\overline{k}_\rho, \zeta_0)\, \hat{F}(\overline{k}_\rho) - \tilde{F}(\overline{k}_\rho, \zeta_0) \right|^2 - \tilde{N} \right] + \int\limits_{-\infty}^{\infty} \mathrm{d}\overline{k}_\rho \left| \hat{F}(\overline{k}_\rho) \right|^2 \quad (4.13)$$

is considered where $\alpha = 1/\beta > 0$ serves as a regularization parameter which weighs closeness of matching the data [first term in (4.13)] against finiteness of energy or smoothness (second term) for any approximation $\hat{F}$ to F, and $\tilde{N}$ is the energy of the noise corrupting the data representing $\tilde{F}$.

Functionals similar to (4.13) were first introduced in 1963 by A. N. Tikhonov for the regularization of solutions to general Fredholm integral equations of the first kind [116]–[119]. Since then Tikhonov regularization has penetrated into many sectors of technology and applied sciences and is often the method of choice in approaching a variety of linear and nonlinear inverse problems numerically.

To minimize C, the right-hand side of (4.13) is rewritten as

$$\int\limits_{-\infty}^{\infty} \mathrm{d}\overline{k}_\rho \left(1 + \beta\,|G|^2\right) \left[\left| \hat{F} - \frac{G^*\,\tilde{F}}{|G|^2 + \alpha} \right|^2 + \frac{\alpha\,|\tilde{F}|^2}{\left(|G|^2 + \alpha\right)^2} \right] - \beta\,\tilde{N} \quad (4.14)$$

where G^* is the complex-conjugate of G.

Hence, for any chosen α, the optimal deconvolution filter in this output least-squares formulation with Tikhonov regularization is represented by the transfer function

$$\Gamma_T(\overline{k}_\rho) = \frac{G^*(\overline{k}_\rho, \zeta_0)}{\left| G(\overline{k}_\rho, \zeta_0) \right|^2 + \alpha} \quad (4.15)$$

For $\alpha \ll \left| G(\overline{k}_\rho, \zeta_0) \right|^2$ we essentially have $1/G(\overline{k}_\rho, \zeta_0)$ but if the inequality is reversed the low-pass filter $G^*(\overline{k}_\rho, \zeta_0)/\alpha$ dominates. In both extreme cases unsatisfactory reconstruction results would be expected (in the first case due to instability, in the second due to loss of resolution). The optimal choice of α will in general depend on the selected optimality criterion, the noise in the data, and the spectrum of the object

function f.

Simultaneous minimization of (4.13) with respect to the regularization parameter β, i. e., consideration of

$$\frac{\partial C}{\partial \beta} = 0 \tag{4.16}$$

leads to

$$\int_{-\infty}^{\infty} \mathrm{d}\overline{k}_\rho \left| G(\overline{k}_\rho, \zeta_0)\, \hat{F}(\overline{k}_\rho) - \tilde{F}(\overline{k}_\rho, \zeta_0) \right|^2 = \tilde{N} \tag{4.17}$$

which is known as the discrepancy principle [120]–[122]. Inserting $\hat{F} = \Gamma_T \, \tilde{F}$ into (4.17) gives the following nonlinear equation for α:

$$\alpha^2 \int_{-\infty}^{\infty} \mathrm{d}\overline{k}_\rho \, \frac{|\tilde{F}(\overline{k}_\rho, \zeta_0)|^2}{\left(\left| G(\overline{k}_\rho, \zeta_0) \right|^2 + \alpha \right)^2} = \tilde{N} \tag{4.18}$$

For additive white noise, high-pass filtering of the data representing $\tilde{f}$ with subsequent estimation of $\tilde{N}$ would be an option to make the right-hand side of (4.18) available. A more sophisticated alternative is given by wavelet denoising [123]. The issue of estimating the noise level directly from the data is also addressed in [124].

A regularization parameter choice method that does not explicitly depend on an estimate of $\tilde{N}$ is given by generalized cross-validation (GCV) [125]–[127]. It is remarked that GCV is based on a discrete formulation. For comparisons between methods see [128].

Tikhonov himself described algorithms derived from his regularization method simply as “practical aids for solving incorrectly posed [ill-posed] problems” [117]. It is this practicability that still feeds a flurry of research activity, especially in the area of parameter choice strategies [124], [128]–[130]. This in turn reflects the somewhat artificial character of the introduction of the regularization parameter in (4.13) [131]. In this light, any viable alternative to Tikhonov regularization is of interest.

4.3.2 Local extrapolation

In the following, for our problem here, we give a method that is fundamentally different from what is described in Section 4.3.1. It is inspired by simple insight into the geometry and nature of propagation in physical applications of the theory (Section 4.4). In this sense, we can call the approach described in this section a physics-based signal processing technique.

For a fixed $\overline{\rho}$, $\tilde{f}(\overline{\rho},\zeta)$ is analytic with respect to ζ. This follows from (4.1) in connection with the assumption of additive blurring (4.4) which leads to the representation of the kernel (4.12). Thus we can construct the Taylor series

$$\tilde{f}(\overline{\rho},\zeta) = \sum_{m=0}^{\infty} \frac{1}{m!} \left[\frac{\partial^m}{\partial \zeta^m} \tilde{f}(\overline{\rho},\zeta) \right]_{\zeta=\zeta_0} (\zeta-\zeta_0)^m \tag{4.19}$$

and obtain in particular

$$f(\overline{\rho}) = \sum_{m=0}^{\infty} \frac{(-\zeta_0)^m}{m!} \left[\frac{\partial^m}{\partial \zeta^m} \tilde{f}(\overline{\rho},\zeta) \right]_{\zeta=\zeta_0} \tag{4.20}$$

While the derivatives in (4.20) are not at hand, (4.4) can be employed to determine $\tilde{f}(\overline{\rho},\zeta)$ from $\tilde{f}(\overline{\rho},\zeta_0)$ for any $\zeta > \zeta_0$ in a stable manner. Thus the deconvolution problem (4.1) is reduced to an extrapolation problem for each $\overline{\rho}$ to which standard methods can be applied.

Consider for example polynomial extrapolation. Choose an integer $M > 1$ and ζ_1, ζ_2, ..., ζ_M such that

$$\zeta_0 < \zeta_1 < \zeta_2 < \ldots < \zeta_M \tag{4.21}$$

Lagrange's formula gives [83]

$$f(\overline{\rho}) \approx \sum_{m=1}^{M} a_m \, \tilde{f}(\overline{\rho},\zeta_m) \tag{4.22}$$

with weights

$$a_m = \prod_{\substack{k=1 \\ k\neq m}}^{M} (-\zeta_k) \Bigg/ \prod_{\substack{k=1 \\ k\neq m}}^{M} (\zeta_m - \zeta_k) = \prod_{\substack{k=1 \\ k\neq m}}^{M} \frac{1}{1-\zeta_m/\zeta_k} \tag{4.23}$$

Inserting (4.4) into (4.22) yields the estimate

$$\hat{f}_L(\overline{\rho}) = \sum_{m=1}^{M} a_m \int_{-\infty}^{\infty} \mathrm{d}\overline{\rho}'\, g(\overline{\rho}-\overline{\rho}', \zeta_m - \zeta_0)\, \tilde{f}(\overline{\rho}', \zeta_0) \tag{4.24}$$

The M convolutions in this local extrapolation scheme can be carried out numerically in the frequency domain, applying the fast Fourier transform (FFT) algorithm. Note that we exclude the given image from the extrapolation, thus suppressing noise in the data through the smoothing character of the blurring process.

The local character of $\hat{f}_L$ is most obvious from (4.22). If the $\tilde{f}(\overline{\rho}, \zeta_m)$ were measured instead of calculated from $\tilde{f}(\overline{\rho}, \zeta_0)$ the result of the extrapolation for any particular $\overline{\rho}$ would be completely independent of the others. But the convolutions in (4.24) are localized operations as well since the main contribution to the integral comes from around $\overline{\rho}' = \overline{\rho}$. This is because (4.7) implies that $g(\overline{\rho}, \zeta)$ is a blurred version of $g(\overline{\rho}, 0) = \delta(\overline{\rho})$, the latter being perfectly localized, and thus the largest values of $g(\overline{\rho}, \zeta)$ are expected near $\overline{\rho} = 0$.

The operation (4.24) is also a linear, shift-invariant filtering of the data. One might therefore ask how the corresponding transfer function looks like, in order to compare with (4.15). Transforming (4.24) to the frequency domain and inserting (4.12) gives the following:

$$\Gamma_L(\overline{k}_\rho) = \sum_{m=1}^{M} a_m\, G(\overline{k}_\rho, \zeta_m - \zeta_0) = \sum_{m=1}^{M} a_m\, \mathrm{e}^{-G_0'(\overline{k}_\rho)\,(\zeta_m - \zeta_0)} \tag{4.25}$$

The last expression displays explicitly the idea of how local extrapolation stabilizes the solution of the inverse problem: Since $\zeta_m > \zeta_0$ it is seen that Γ_L is in terms of decaying exponentials whenever $1/G(\overline{k}_\rho, \zeta_0) = \exp[G_0'(\overline{k}_\rho)\,\zeta_0]$ is a growing exponential. This,

however, does not imply that the extrapolation might not cause a large error for poorly chosen a_m.

An alternative representation of Γ_L is given by

$$\Gamma_L(\overline{k}_\rho) = \hat{G}(\overline{k}_\rho)/G(\overline{k}_\rho, \zeta_0) \tag{4.26}$$

where

$$\hat{G}(\overline{k}_\rho) = \sum_{m=1}^{M} a_m\, G(\overline{k}_\rho, \zeta_m) \tag{4.27}$$

which is an approximation of $G(\overline{k}_\rho, 0) = 1$ based on an extrapolation of $G(\overline{k}_\rho, \zeta_m)$, $m = 1, 2, \ldots, M$. Representing the noise in the measurement of $\tilde{F}(\overline{k}_\rho, \zeta_0)$ explicitly by $N(\overline{k}_\rho)$ we have

$$\begin{aligned} \hat{F}_L(\overline{k}_\rho) &= \Gamma_L(\overline{k}_\rho)\, \Big[G(\overline{k}_\rho, \zeta_0)\, F(\overline{k}_\rho) + N(\overline{k}_\rho)\Big] && (4.28)\\ &= \hat{G}(\overline{k}_\rho)\, F(\overline{k}_\rho) + \Gamma_L(\overline{k}_\rho)\, N(\overline{k}_\rho) && (4.29) \end{aligned}$$

In the absence of noise, (4.29) reduces to $\hat{F}_L = \hat{G}\, F$ which suggests the identification of $\hat{G}$ as the model resolution kernel. It represents a measure of how well the image is reconstructed. If the model resolution kernel is unity, i. e., its corresponding spatial representation is a delta function, then the resolution is perfect and the reconstructed image is identical to the original image. If, on the other hand, the model resolution kernel is different from unity, then the reconstructed image will in general be a smoothed version of the original image.

From (4.29), the image reconstruction error is given by

$$\begin{aligned} \hat{F}_L(\overline{k}_\rho) - F(\overline{k}_\rho) &= \Big[\hat{G}(\overline{k}_\rho) - 1\Big]\, F(\overline{k}_\rho) + \Gamma_L(\overline{k}_\rho)\, N(\overline{k}_\rho) && (4.30)\\ &= \Big[\hat{G}(\overline{k}_\rho) - G(\overline{k}_\rho, \zeta = 0)\Big]\, F(\overline{k}_\rho) + \Gamma_L(\overline{k}_\rho)\, N(\overline{k}_\rho) && (4.31) \end{aligned}$$

Hence, the error in reconstructing the image depends on how well $\hat{G}(\overline{k}_\rho)$ approximates

$G(\overline{k}_\rho, \zeta = 0)$ and how effective is the exponential decay introduced by the transfer function Γ_L in suppressing the noise in the data. These two objectives are in conflict and hence a compromise has to be achieved for optimally reconstructing the image and maximally suppressing the data noise. This will depend on the choice of the ζ_m and the total number of sampling points M.

By choosing the sampling points of (4.21) to be equidistant, the number of parameters in the local extrapolation scheme can be reduced to two, namely M and the spacing of the grid $\Delta\zeta$. We then have for polynomial extrapolation

$$a_m = \prod_{\substack{k=1 \\ k\neq m}}^{M} \frac{k + \zeta_0/\Delta\zeta}{k - m} = \frac{(-1)^{m-1}}{(m-1)!\,(M-m)!} \prod_{\substack{k=1 \\ k\neq m}}^{M} \left(k + \frac{\zeta_0}{\Delta\zeta}\right) \tag{4.32}$$

which is a polynomial in $\zeta_0/\Delta\zeta$ of degree $M-1$. The representation of Γ_L as given in (4.25) becomes

$$\Gamma_L(\overline{k}_\rho) = \sum_{m=1}^{M} a_m \, \mathrm{e}^{-G_0'(\overline{k}_\rho)\, m\, \Delta\zeta} \tag{4.33}$$

For a fixed and finite M, and as $\Delta\zeta \to 0$, the transfer function (4.33) with the coefficients (4.32) can be shown to reduce to

$$\Gamma_L(\overline{k}_\rho) = \sum_{k=0}^{M-1} \frac{1}{k!} \left[G_0'(\overline{k}_\rho)\, \zeta_0\right]^k \tag{4.34}$$

which is a truncated power series expansion of

$$\frac{1}{G(\overline{k}_\rho, \zeta_0)} = \mathrm{e}^{G_0'(\overline{k}_\rho)\, \zeta_0} \tag{4.35}$$

Hence, even though (4.33) is in terms of decaying exponentials, in this limit $\Gamma_L(\overline{k}_\rho)$ will be growing with $\overline{k}_\rho$, with faster growth for larger M (approaching the expected mathematical limit of $\exp[G_0'(\overline{k}_\rho)\, \zeta_0]$ as $M \to \infty$). This will cause a large reconstruction error due to the amplification of the noise in (4.31) [see Fig. 4-6(b) and 4-9(b) where the error grows as $\Delta\zeta \to 0$, increasingly with M, and note the similar but

different behavior of (4.15) as $\alpha \to 0$]. Furthermore, in the same limit (fixed and finite M, and $\Delta\zeta \to 0$), the extrapolated $\tilde{f}$ in (4.22) and G in (4.27) are oversampled and under-represented (since $M\Delta\zeta \to 0$). In this case, one would be attempting to extrapolate a function from its value at one point, introducing an error in representing f by $\hat{f}_L$ and $G(\overline{k}_\rho, 0)$ by $\hat{G}(\overline{k}_\rho)$. Numerically, as $\Delta\zeta \to 0$, the derivatives required in the extrapolation and which are replaced by finite differences (note that an interpolating polynomial can be rewritten in terms of divided differences [83]) will exhibit a large round-off error which may actually cause the result to diverge as $1/(\Delta\zeta)^{M-1}$ [not visible in Fig. 4-6(b) and 4-9(b) where a linear scale for $\Delta\zeta$ is used, and where the error was computed for $\Delta\zeta$ down to only a moderately small value and is not shown when exceeding 100 %].

On the other hand, and as $\Delta\zeta \to \infty$, the transfer function (4.33) becomes exponentially small whenever $\mathrm{Re}\, G_0'(\overline{k}_\rho) > 0$, hence suppressing the data noise. In this case the error in the reconstructed image will be dominated by the error of $\hat{G}$ in approximating unity. As $\Delta\zeta \to \infty$, the extrapolated function $G(\overline{k}_\rho, \zeta)$ will be undersampled and $\hat{G}(\overline{k}_\rho)$ will not be an accurate representation of $G(\overline{k}_\rho, \zeta = 0)$. This effect can be expected to be more severe at the higher frequencies, thus leading to a smoothed image.

From the above discussion, one may conclude that for a certain number of sampling points M there is an optimum $\Delta\zeta$ which minimizes the error in the reconstructed image [Fig. 4-6(b) and Fig. 4-9(b)].

If we consider a particular M then a possible criterion for choosing $\Delta\zeta$ can again be based on the discrepancy principle (4.17), solving for $\Delta\zeta$ from the following equation:

$$\int_{-\infty}^{\infty} \mathrm{d}\overline{k}_\rho \left| 1 - \sum_{m=1}^{M} a_m(\Delta\zeta)\, G(\overline{k}_\rho, \zeta_0 + m\Delta\zeta) \right|^2 \left| \tilde{F}(\overline{k}_\rho, \zeta_0) \right|^2 = \tilde{N} \tag{4.36}$$

Here the spectral integral could also be replaced by its spatial counterpart, using Parseval's relation and introducing a convolution in the integrand. It is pointed

out that this is not an option for (4.18) because of its more complicated algebraic structure.

An alternative extrapolation technique that gives an estimate of $f(\overline{\rho})$, which depends nonlinearly on the data $\tilde{f}(\overline{\rho}, \zeta_m)$ [c. f., (4.22)] and which therefore does not lead to a linear filter as in (4.24), uses, e. g., Padé approximation [104, 132]. The idea behind employing such a nonlinear method is that, in principle, it can lead to deblurred data with spectral contents at frequencies which were completely suppressed by the forward smoothing process, and therefore it may possibly lead to sharper images. However, high sensitivity to noise will require additional low-pass filtering. In all the numerical experiments conducted, we did not find any superior results with this nonlinear method, which led us to return to the simpler polynomial extrapolation.

4.4 Applications and numerical examples

4.4.1 Magnetostatic imaging

Here we consider the problem of imaging geometrical imperfections of the otherwise flat interface between free space and a magnetic medium with permeability μ_1. This is illustrated in Fig. 4-1 where $\mu_1 \gg \mu_0$ is assumed (this is not necessary for what follows). Only pit-like defects are considered, i. e., for $\zeta > 0$ we always have free space. We assume that the imaging system is supposed to be based on inducing a tangential magnetic flux in the medium (in such a way that the normal component of the background field, i. e., the magnetic field for the case of a perfectly planar interface, vanishes) and measuring the normal component of the magnetic flux density, $B_\zeta(\overline{k}_\rho)$, in free space due to the defect. For example, a Hall detector could be used to scan the two-dimensional planar distribution $B_\zeta(\overline{\rho}, \zeta_0)$ for a fixed ζ_0. Due to mechanical constraints always $\zeta_0 > 0$. However, we might be interested in $B_\zeta(\overline{\rho}, 0)$ because this distribution can give us a first idea of the general shape of the defect to be analyzed. This could be useful in deriving an initial guess for an algorithm that inverts for the

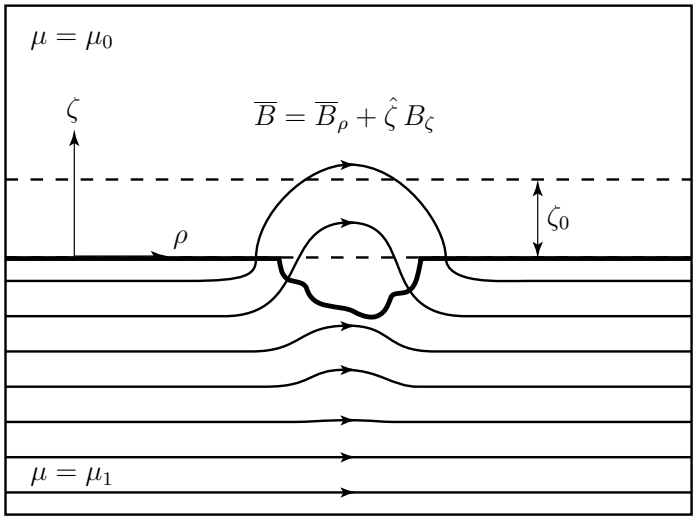

Figure 4-1: Leakage of the magnetic flux density due to a defect ($\mu_1 \gg \mu_0$).

three-dimensional features of the imperfection.

The problem of obtaining $B_\zeta(\overline{\rho}, 0)$ from $B_\zeta(\overline{\rho}, \zeta_0)$ is equivalent [28] to deducing the distribution of a magnetic surface charge distribution $\rho_{ms}(\overline{\rho}) = B_\zeta(\overline{\rho}, 0)$, impressed onto a perfectly planar perfect electric conductor occupying the half space $\zeta < 0$, from a similar measurement. Alternatively, $B_\zeta(\overline{\rho}, \zeta_0)$ can be thought of as being produced by a magnetic surface charge distribution $\rho'_{ms}(\overline{\rho}) = 2\, B_\zeta(\overline{\rho}, 0)$ located at $\zeta = 0$ in free space. Consideration of above equivalent problems shows that the task of retrieving $B_\zeta(\overline{\rho}, 0)$ from $B_\zeta(\overline{\rho}, \zeta_0)$ can also be viewed as a source inversion problem.

The second equivalent problem mentioned, with a planar charge distribution in free space, sometimes called "equivalent stratum" [133], leads directly to an integral equation relating $B_\zeta(\overline{\rho}, \zeta_0)$ and $B_\zeta(\overline{\rho}, 0)$:

$$B_\zeta(\overline{\rho}, \zeta_0) = \mu_0 \left[-\frac{\partial}{\partial \zeta} \int_{-\infty}^{\infty} \mathrm{d}\overline{\rho}' \, \frac{\rho'_{ms}(\overline{\rho}')}{4\pi\, \mu_0 \sqrt{|\overline{\rho} - \overline{\rho}'|^2 + \zeta^2}} \right]_{\zeta = \zeta_0} \tag{4.37}$$

or

$$B_\zeta(\overline{\rho},\zeta_0) = \int_{-\infty}^{\infty} \mathrm{d}\overline{\rho}'\, g(\overline{\rho}-\overline{\rho}',\zeta_0)\, B_\zeta(\overline{\rho}',0) \tag{4.38}$$

with the planar Poisson kernel

$$g(\overline{\rho},\zeta) = \frac{\zeta}{2\pi\,(\overline{\rho}^2+\zeta^2)^{3/2}} \tag{4.39}$$

Apparently (4.38) can also be interpreted as solution to Dirichlet's problem for Laplace's equation in the half space $\zeta > 0$ [134]. The reason for this is that $B_\zeta(\overline{r})$ being proportional to a derivative of a harmonic potential is itself harmonic.

Equation (4.38) is of the form (4.1) with $\tilde{f}(\overline{\rho},\zeta) = B_\zeta(\overline{\rho},\zeta)$ and $f(\overline{\rho}) = B_\zeta(\overline{\rho},0)$. Equation (4.4) follows directly from the space invariance of the physical configuration considered (propagation in free space), i. e.,

$$B_\zeta(\overline{\rho},\zeta+\Delta\zeta) = \int_{-\infty}^{\infty} \mathrm{d}\overline{\rho}'\, g(\overline{\rho}-\overline{\rho}',\Delta\zeta)\, B_\zeta(\overline{\rho}',\zeta) \tag{4.40}$$

Thus, the magnetostatic imaging problem described here falls exactly into the class of inverse additive blurring problems solved by the methods in Section 4.3.

As an illustration of the application of the local extrapolation scheme of Section 4.3.2, consider Fig. 4-2. The data in the plane $\zeta = \zeta_0$ are continued upward onto planes at $\zeta > \zeta_0$, by virtue of (4.40). All the data points at $\zeta = \zeta_0$ contribute to a single point located at $\zeta > \zeta_0$. $B_\zeta(\overline{\rho},0)$ is then extrapolated locally, for each $\overline{\rho}$, from the generated data at $\zeta > \zeta_0$ along the vertical lines $\overline{\rho} = \text{const}$.

Application of the Tikhonov regularization method of Section 4.3.1 and a computationally efficient implementation of the local extrapolation scheme via the FFT algorithm require a transition to the spatial frequency domain with respect to the transverse dimensions described by $\overline{\rho}$. The kernel (4.39) corresponds to its Fourier transform

$$G(\overline{k}_\rho,\zeta) = \mathrm{e}^{-k_\rho\,\zeta} \tag{4.41}$$

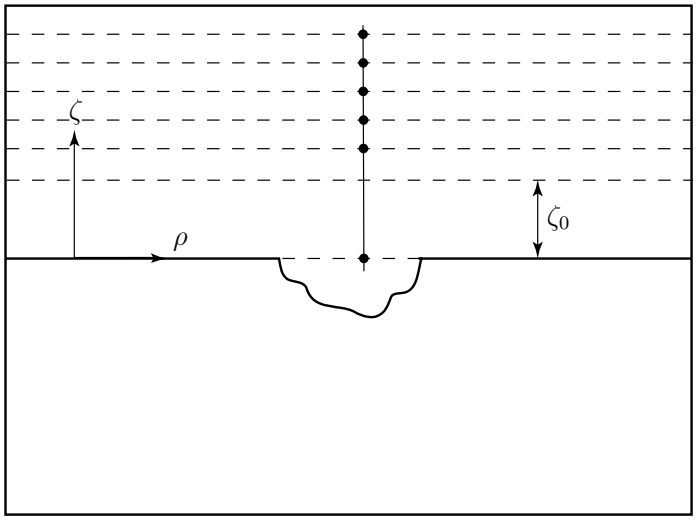

Figure 4-2: Schematic representation of the basic idea of local extrapolation applied to the magnetostatic imaging configuration of Fig. 4-1.

The correspondence (4.39)/(4.41) follows from another Fourier pair, namely

$$\frac{1}{2\pi\sqrt{\rho^2+\zeta^2}} = \mathcal{F}^{-1}\left\{\frac{\mathrm{e}^{-k_\rho\,\zeta}}{k_\rho}\right\} \tag{4.42}$$

by differentiating with respect to ζ. Equation (4.42) in turn can be shown by evaluating the inverse Fourier transform in polar coordinates, doing the angular integral first, and applying an identity [50] to the remaining Fourier-Bessel transform [31] involving the Bessel function of zeroth order J_0. Alternatively, (4.39) can be obtained directly from (4.41) in a similar fashion, applying a different identity [50]. Clearly, (4.41) is in the form (4.12). Equation (4.3) follows from (4.39) as the generalized limit $\zeta \to 0$.

Formulas for the continuation of the tangential (secondary or scattered) components $B_{x,y}$ can be obtained as well. They are the same as (4.38), with the same kernel. $B_{x,y}(\overline{\rho},\zeta)$ for $\zeta > 0$ can also be computed from $B_\zeta(\overline{\rho},0)$. The governing equations are derived from (4.37) by replacing the derivative with respect to ζ by the derivative

with respect to x or y. The resulting kernels are given by

$$g(\overline{\rho},\zeta) = \frac{\hat{a}\cdot\overline{\rho}}{2\pi\left(\rho^2+\zeta^2\right)^{3/2}} \qquad \hat{a} = \hat{x},\hat{y} \tag{4.43}$$

with corresponding Fourier transforms

$$G(\overline{k}_\rho,\zeta) = \frac{\hat{a}\cdot\overline{k}_\rho}{\mathrm{i}\,k_\rho}\,\mathrm{e}^{-k_\rho\,\zeta} \tag{4.44}$$

However, the continuation from $\zeta = 0$ to B_ζ at $\zeta > 0$ is the most important case because this component is orthogonal and hence insensitive to the background field (see the introduction to this section). It is interesting to note that an estimate for $B_{x,y}(\overline{\rho},0)$ can be obtained from $B_\zeta(\overline{\rho},\zeta_0)$ with help of the local extrapolation scheme by using the kernels (4.43) for the continuation from B_ζ to $B_{x,y}$. However, the kernels for continuation from $B_{x,y}$ to B_ζ are found to correspond to

$$G(\overline{k}_\rho,\zeta) = \frac{\mathrm{i}\,k_\rho}{\hat{a}\cdot\overline{k}_\rho}\,\mathrm{e}^{-k_\rho\,\zeta} \tag{4.45}$$

Note that (4.44) is bounded whereas (4.45) is not.

It is seen that the consideration of "cross-continuation", i. e., from one component of $\overline{B}$ to a different one, leads to convolution kernels such as (4.43) which do not fit directly into the general framework of Section 4.2. However, (4.44) and (4.45) show that the continuation process here consists of the cascade of a linear, shift-invariant transformation, which is independent of ζ, and a blurring process in the sense of Section 4.2 that is the same in all cases considered.

While we considered magnetostatic imaging in this section, similar ideas apply to electrostatics. In a typical application one may attempt to image the induced electric charges on a buried metallic pipe where it is assumed that the pipe is excited by an electric field perpendicular to its longitudinal axis.

4.4.2 Downward continuation of gravity data

Earth's gravity is the sum of gravitational and centrifugal force. Since it is irrotational it can be derived from a scalar gravity potential. It is useful to introduce a reference potential called normal potential due to a rotating ellipsoid, and the corresponding normal gravity field [135]–[137]. The gravity disturbance δg and the gravity anomaly Δg are defined as the difference of the magnitudes, or as the magnitude of the difference [137], of the actual gravity vector and the normal gravity vector. The important difference between the two quantities is that for the gravity disturbance δg the comparison is made at one and the same point, while for the gravity anomaly Δg to be defined at a point P the normal gravity is taken at a corresponding point Q on that level surface of the normal gravity field which has the same potential as the actual gravity field at P, where Q is situated on the orthogonal projection line of P onto the reference ellipsoid. Despite this complication which is due to practical limitations of classical terrestrial geodesy, with r_0 denoting the distance to the geocenter, $r_0\,\delta g$ and $r_0\,\Delta g$ outside the Earth are commonly treated as harmonic functions (for the rigorous justification of this simplification see the literature cited above). It is the quantities δg and Δg that are measured by means of gravimetry.

The problem of determining δg or Δg from a measured distribution at locations towards the disturbing masses is referred to as downward continuation [133], [138]–[141]; it is of great importance in the Earth sciences. Note that this problem was mentioned by Tikhonov as an illustrative example in an early paper [117].

In a typical application airborne gravimetry is used to measure two-dimensional distributions of the gravity disturbance or anomaly at some altitude while the actual interest is in the distribution at a lower altitude or at the Earth's surface. A similar problem arises in shipborne gravimetry with the goal to obtain gravity data at the ocean bottom (for an interesting example of how people try to overcome the loss of resolution when measurements are made at the sea surface refer to [142]). In many cases, such as mapping of the gravity field, a successful downward continuation is the

ultimate numerical objective. However, the capability of enhancing the resolution of the measured data might also prove helpful in the solution of other geophysical inverse problems [143].

Making the assumption that the geocenter is very far away from the region of interest and considering the continuation of the gravity disturbance or anomaly from one plane to another leads again to the kernel given by (4.39) corresponding to (4.41). At this point it is appropriate to remark that the basic idea of the local extrapolation scheme in the context of geophysical interpretation of planar gravity and also magnetic data—downward continuation by means of upward continuation followed by polynomial extrapolation—was brought forward already in 1960 by R. G. Henderson [133, 144].

However, the nowadays achievable high accuracy of gravimetry in conjunction with the global positioning system also calls for more accurate downward continuation schemes. The problem of continuation of harmonic functions from one spherical surface to another leads to the non-convolutional spherical Poisson kernel so that the methods of this paper cannot be applied without modification. The essential idea of the local extrapolation scheme, however, can also be employed in this case, carrying out the extrapolation along radial lines towards the center of the sphere. Bláha *et al.* demonstrate how a convolutional approximation of the spherical Poisson kernel can be obtained [145] so that the upward continuation could be performed in a numerically efficient manner with use of the FFT algorithm.

4.4.3 Inverse diffraction of scalar waves

The applications discussed in the previous subsections were based on static potential theories, i. e., we considered the blurring of solutions to Laplace's equation. In the following we generalize these ideas to the dynamic case.

In the temporal frequency domain, scalar waves in a homogeneous, source-free region characterized by a real wavenumber $k = 2\pi/\lambda$ where λ is the wavelength in

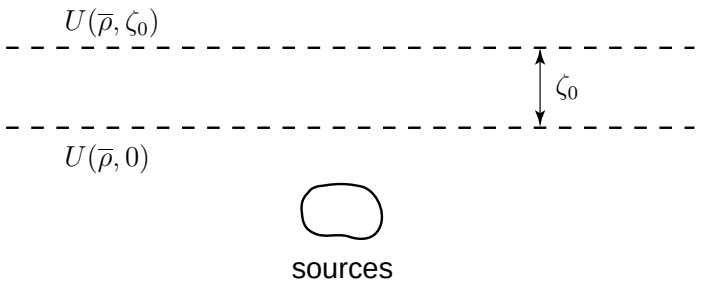

Figure 4-3: Plane-to-plane continuation of scalar wave fields away from the sources.

the medium are solutions to the Helmholtz equation

$$\left(\nabla^2 + k^2\right) U(\overline{r}) = 0 \tag{4.46}$$

which for $k = 0$ specializes to Laplace's equation.

For the propagation of the planar distribution of a disturbance $U(\overline{\rho},0)$ away from the sources to a parallel plane at a distance ζ_0 (Fig. 4-3) again an equation of the form (4.1) holds:

$$U(\overline{\rho},\zeta_0) = \int_{-\infty}^{\infty} \mathrm{d}\overline{\rho}'\, g(\overline{\rho}-\overline{\rho}',\zeta_0)\, U(\overline{\rho}',0) \tag{4.47}$$

The propagator g in this expression of Huygens' principle for the plane (also referred to as Rayleigh diffraction formula of the first kind) is most conveniently found by the application of Green's theorem in conjunction with the method of images [146], leading to

$$g(\overline{\rho},\zeta) = \frac{1}{4\pi}\left[\frac{\partial}{\partial\zeta'}\left(\frac{\mathrm{e}^{\mathrm{i}k\sqrt{\rho^2+(\zeta-\zeta')^2}}}{\sqrt{\rho^2+(\zeta-\zeta')^2}} - \frac{\mathrm{e}^{\mathrm{i}k\sqrt{\rho^2+(\zeta+\zeta')^2}}}{\sqrt{\rho^2+(\zeta+\zeta')^2}}\right)\right]_{\zeta'=0} \tag{4.48}$$

After some algebra, this yields in generalization of (4.39) and for arbitrary $\zeta > 0$

$$g(\overline{\rho},\zeta) = \frac{\zeta}{2\pi\left(\rho^2+\zeta^2\right)^{3/2}}\left(1 - \mathrm{i}k\sqrt{\rho^2+\zeta^2}\right)\mathrm{e}^{\mathrm{i}k\sqrt{\rho^2+\zeta^2}} \tag{4.49}$$

Note that as $\zeta \to 0$, significant values of g are found only for $k\rho \ll 1$ in which case

$$1 - \mathrm{i}k\sqrt{\rho^2 + \zeta^2} \approx \mathrm{e}^{-\mathrm{i}k\sqrt{\rho^2+\zeta^2}} \tag{4.50}$$

which cancels the third term in (4.49). Thus the singular behavior of the kernel (4.49) is the same as that of (4.39), and (4.3) follows as before.

While obtaining $G(\overline{k}_\rho, \zeta)$ corresponding to (4.49) by direct Fourier transformation appears difficult, this task is achieved by taking the point of view of scalar diffraction theory [31]. By interpreting the Fourier transform of $U(\overline{\rho}, 0)$ as an "angular spectrum" of plane waves whose wavevectors satisfy all the same dispersion relation we arrive at

$$G(\overline{k}_\rho, \zeta) = \begin{cases} \mathrm{e}^{\mathrm{i}\zeta\sqrt{k^2-k_\rho^2}} & k_\rho \le k \\ \mathrm{e}^{-\zeta\sqrt{k_\rho^2-k^2}} & k_\rho > k \end{cases} \tag{4.51}$$

Observe how this complies with (4.12) and how (4.51) simplifies to (4.41) in the case $k = 0$.

The application of Tikhonov regularization to this dynamic deblurring problem, which is also known as inverse diffraction problem for the plane [147]–[151], is discussed in [152].

It is clear that direct application of the local extrapolation scheme would lead to poor results (unless $k\,\zeta_0 \ll 1$) due to the oscillatory behavior of (4.49) with respect to ζ. We therefore devised a method that separates the deblurring process into two subsequent problems, one of which is well-posed and the other solvable by local extrapolation. The key is to treat propagating waves ($k_\rho \le k$) and evanescent waves ($k_\rho > k$) separately. More specifically, let

$$G(\overline{k}_\rho, \zeta) = G_p(\overline{k}_\rho, \zeta)\, G_e(\overline{k}_\rho, \zeta) \tag{4.52}$$

where

$$G_p(\overline{k}_\rho, \zeta) = \left\{ \begin{array}{ll} \mathrm{e}^{\mathrm{i}\zeta\sqrt{k^2-k_\rho^2}} & k_\rho \leq k \\ 1 & k_\rho > k \end{array} \right\} = \mathrm{e}^{\mathrm{i}\zeta\,\mathrm{Re}\sqrt{k^2-k_\rho^2}} \tag{4.53}$$

and

$$G_e(\overline{k}_\rho, \zeta) = \left\{ \begin{array}{ll} 1 & k_\rho \leq k \\ \mathrm{e}^{-\zeta\sqrt{k_\rho^2-k^2}} & k_\rho > k \end{array} \right\} = \mathrm{e}^{-\zeta\,\mathrm{Im}\sqrt{k^2-k_\rho^2}} \tag{4.54}$$

Note that $|G_p| = 1$ for all k_ρ and that the effect of G_p can hence be removed in a stable manner by correcting the phases of the Fourier transform of $U(\overline{\rho}, \zeta_0)$. The blurring due to G_e can then be elevated by applying the local extrapolation scheme. Note that $G_e(\overline{k}_\rho, \zeta)$ is real and even in $\overline{k}_\rho$, thus $g_e(\overline{\rho}, \zeta)$ will be real and even in $\overline{\rho}$.

One potential application of the procedure outlined above is in diffraction tomography [153]. In this (originally but not necessarily) ultrasonic imaging technique an inhomogeneity is illuminated by an incident wave and reconstructed from the measured scattered waves originating from the secondary sources induced in the object. Deblurring could be applied to gather preliminary information on extent and shape of the object which would be useful in deriving an initial guess for the reconstruction algorithm.

Another application is object field reconstruction in scanning near-field optical microscopy, an imaging technology that has generated a lot of interest recently [154]–[156].

For inverse diffraction of *vector* waves and for the planar geometry, the theory of this section can be applied to each of the components of the vector field individually and without modification. This is permissible because the vector Helmholtz equation in Cartesian coordinates separates into three scalar Helmholtz equations (4.46). Equation (4.47) also follows from Huygens' principle for electromagnetic waves, expressed as the Kirchhoff vector formula for diffraction [28] and using the Green function (4.49).

4.4.4 Numerical examples

In this section we compare results of the application of the local extrapolation scheme as introduced in Section 4.3.2 with the Tikhonov regularization of Section 4.3.1. For simplicity, (4.21) is taken to be equidistant which leaves M and the grid spacing $\Delta\zeta$ as parameters in the local extrapolation scheme [c. f., (4.32)]. The Tikhonov regularization approach depends on the single parameter α.

For the first example, the blurring kernel considered is given by (4.39), i. e., this case study applies to the plane-to-plane continuation of solutions to Laplace's equation as encountered in, e. g., electrostatics, magnetostatics, and gravitational theory (Section 4.4.1, 4.4.2). Two-dimensional $\overline{\rho}$ is represented by Cartesian coordinates x and y. The length unit mm was arbitrarily chosen while the problem is actually scale-invariant. Each of the five images in Fig. 4-4 and 4-5 consists of 64 by 64 pixels and is shown by two plots: On the left-hand side the data are plotted with linear greylevels where white corresponds to the smallest value in the particular image and black to the largest. On the right-hand side the data are displayed along the 64 traces $x = \text{const}$.

Fig. 4-4 demonstrates the forward blurring process. An undistorted image $f(\overline{\rho})$ which is equal to one inside a square with sides of 15 mm length and zero elsewhere is assumed as shown in Fig. 4-4(a). Blurring with $\zeta = \zeta_0 = 2.5\,\text{mm}$ leads to the data $\tilde{f}(\overline{\rho}, \zeta_0)$ in Fig. 4-4(b) where the decrease in maximum amplitude should be noted. The 2-D convolution is implemented using the FFT algorithm. Addition of pseudorandom white Gaussian noise $n(\overline{\rho})$ generates the corrupted data set displayed in Fig. 4-4(c). The noise level is adjusted to $N/S = 10\,\%$ where for in general complex data (see the second example)

$$\frac{N}{S} = \sqrt{\sum_{\text{pixels}} |n^2(\overline{\rho})| \Big/ \sum_{\text{pixels}} |\tilde{f}(\overline{\rho}, \zeta_0)|^2} \tag{4.55}$$

Using the data of Fig. 4-4(c) as input, the two deblurring methods of Section 4.3

are applied, leading to the results shown in Fig. 4-5. For both approaches the parameters are chosen for optimal performance (see below): $\alpha = 8 \times 10^{-3}$ for Tikhonov regularization [Fig. 4-5(a)] and $M = 5$, $\Delta\zeta = 1.3\,\text{mm}$ for the local extrapolation scheme [Fig. 4-5(b)]. The results show that deblurring is capable of enhancing the resolution of noisy data. In both cases a reasonable approximation $\hat{f}(\overline{\rho})$ to the assumed ideal image $f(\overline{\rho})$ in Fig. 4-4(a) is obtained and the original maximum amplitude is restored accurately.

In order to extend the quantitative comparison between the two deblurring methods processing of the data in Fig. 4-4(c) is repeated many times with varying parameters α [Fig. 4-6(a)] and M, $\Delta\zeta$ [Fig. 4-6(b)]. A root mean squared (RMS) error measure is defined as

$$\text{Relative RMS Error} = \sqrt{\sum_{\text{pixels}} |\hat{f}(\overline{\rho}) - f(\overline{\rho})|^2 \Big/ \sum_{\text{pixels}} |f(\overline{\rho})|^2} \tag{4.56}$$

It is remarked that in a real-world situation $f(\overline{\rho})$ is unknown but that in a numerical assessment the quantity (4.56) is one of primary interest.

It is seen that the relative RMS error for both methods can be minimized by appropriately choosing the parameters α and $\Delta\zeta$; above choice leading to the results in Fig. 4-5 is confirmed as nearly optimal. If either of the parameters is chosen too small, the respective method becomes unstable as predicted in Section 4.3. On the other hand, if they are chosen too large the overall operation has the character of a low-pass filter which smoothes out the data instead of enhancing their resolution. We did not compare the locations of the minima in Fig. 4-6 with the solutions of (4.18) and (4.36), respectively. In practice, making a good heuristic choice of the parameter for the local extrapolation might be easier than for Tikhonov regularization because of the simple geometrical meaning of $\Delta\zeta$.

A similar comparison can be made for the solution of the inverse diffraction problem as outlined in Section 4.4.3. In this second example, all images have a resolution

of 128 times 128 pixels. The data are now in general complex-valued and only their magnitude is shown. Dimensions are given in wavelengths λ.

We start with a real-valued, non-negative object function as shown in Fig. 4-7(a) and which has been considered previously by Bertero *et al.* [151]. Since the image contains details with dimensions that are less than a wavelength the problem is related to the question of achievability of super-resolution. In [151], images reconstructed from far-field data ($\zeta_0 > \lambda$) were shown. Here we consider the case of the near-field zone ($\zeta_0 < \lambda$) and when no *a priori* information such as finiteness of support and positivity of the object function are incorporated.

Fig. 4-7(b) shows the magnitude of the data at $\zeta = \zeta_0 = \lambda/4$, exhibiting a general decrease in amplitude and severe blurring. It is pointed out that this ζ_0 is in fact fairly large as in, e. g., scanning near-field optical microscopy distances down to $0.01\,\lambda$ are considered to be of relevance [155]. The reconstructions in Fig. 4-8 are based on the data displayed in Fig. 4-7(c) where noise with $N/S = 5\,\%$ was added.

Fig. 4-8(a) shows the result for Tikhonov regularization with $\alpha = 6 \times 10^{-3}$, and Fig. 4-8(b) was obtained with local extrapolation ($M = 5$, $\Delta\zeta = 0.125\,\lambda$) where the treatment of propagating and evanescent waves was cascaded as described in Section 4.4.3. As in the first example, both methods perform about equally well. Again, Fig. 4-9 confirms the parameter choices leading to Fig. 4-8 as nearly optimal.

The general similarity between the results for the two examples illustrated in Fig. 4-4 to 4-6 and Fig. 4-7 to 4-9, respectively, is remarkable in as much as the underlying physics are quite different (Laplace vs. Helmholtz equation).

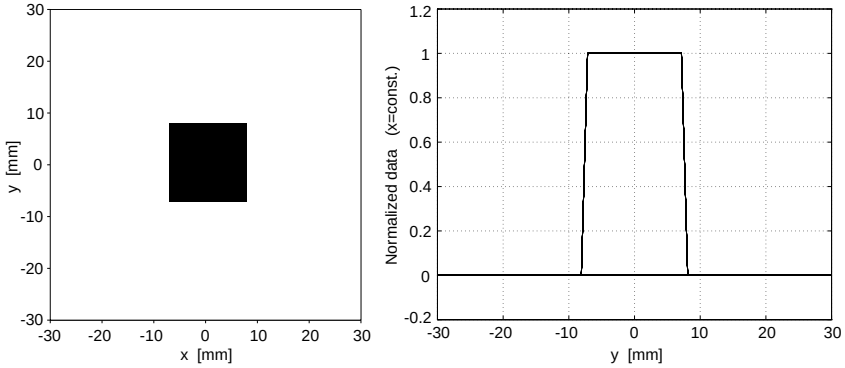

(a) Square with sides of 15 mm length.

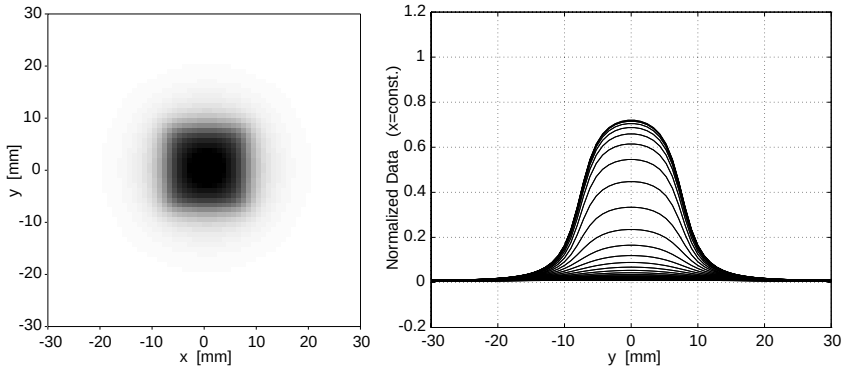

(b) Blurred image ($\zeta = \zeta_0 = 2.5\,\mathrm{mm}$).

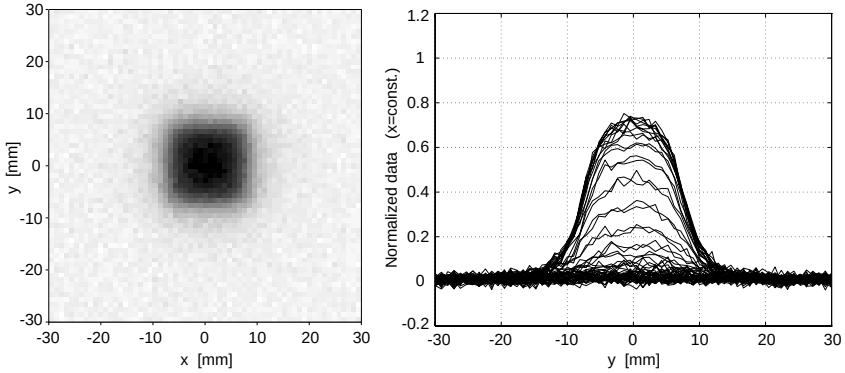

(c) Addition of white Gaussian noise ($N/S = 10\,\%$).

Figure 4-4: Example of the blurring process (Laplace equation).

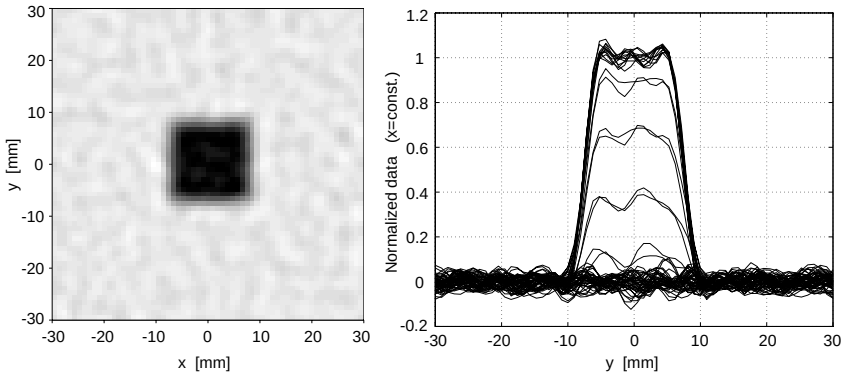

(a) Tikhonov regularization ($\alpha = 8 \times 10^{-3}$).

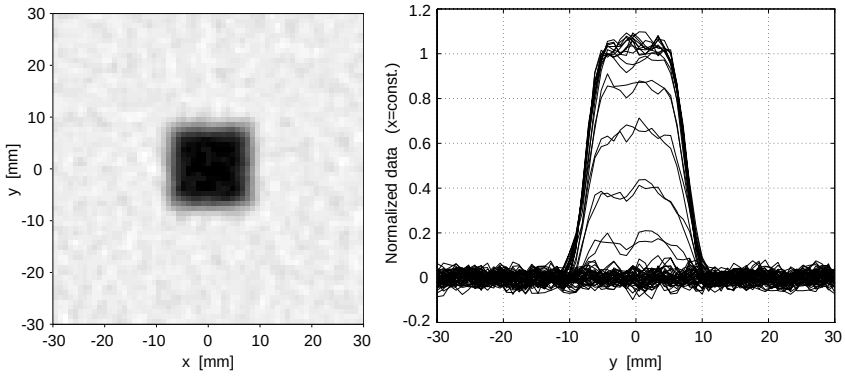

(b) Local extrapolation ($M = 5$, $\Delta\zeta = 1.3\,\mathrm{mm}$).

Figure 4-5: Deblurring based on noisy data (Laplace equation).

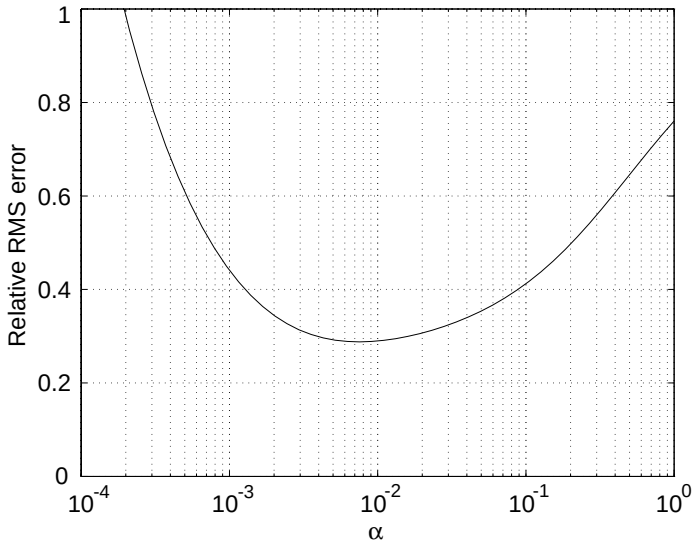

(a) Tikhonov regularization.

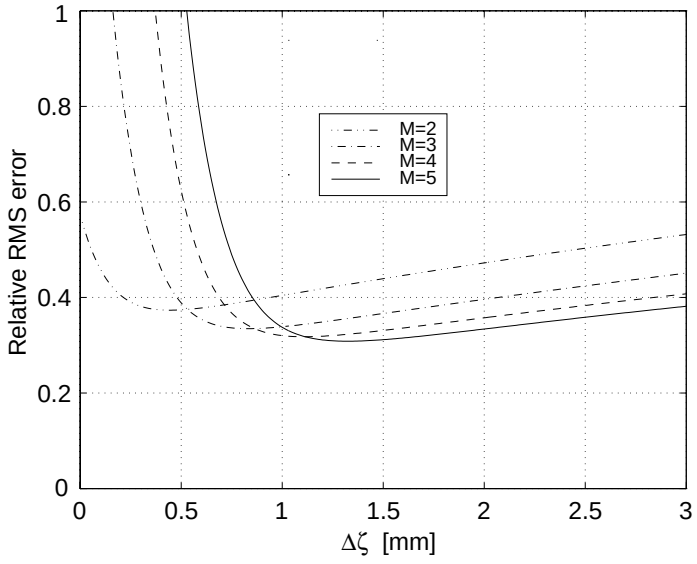

(b) Local extrapolation.

Figure 4-6: Relative RMS error vs. choice of parameters (Laplace equation).

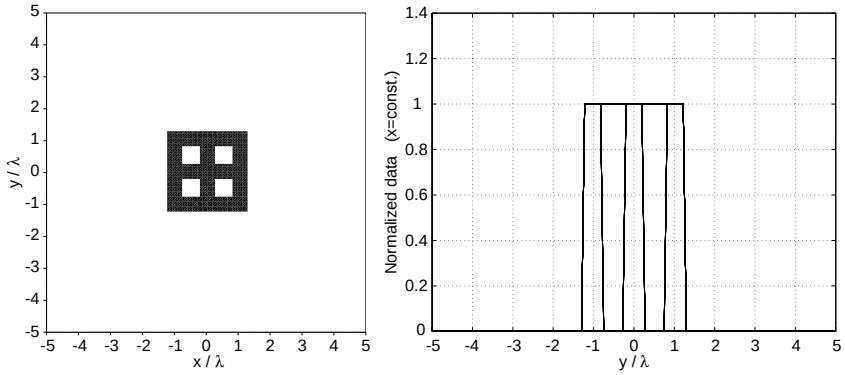

(a) Square with sides of $5 \times \lambda/2$ length.

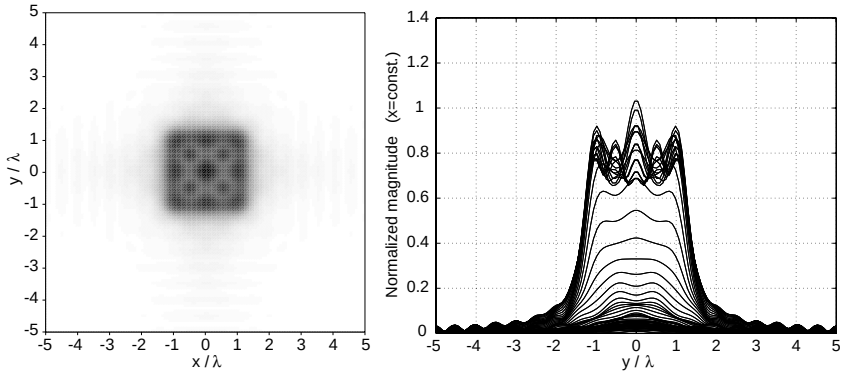

(b) Blurred image ($\zeta = \zeta_0 = \lambda/4$).

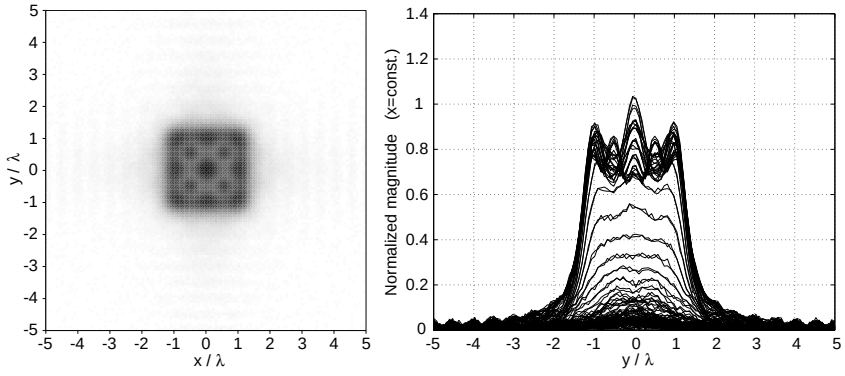

(c) Addition of white Gaussian noise ($N/S = 5\,\%$).

Figure 4-7: Example of the blurring process (Helmholtz equation).

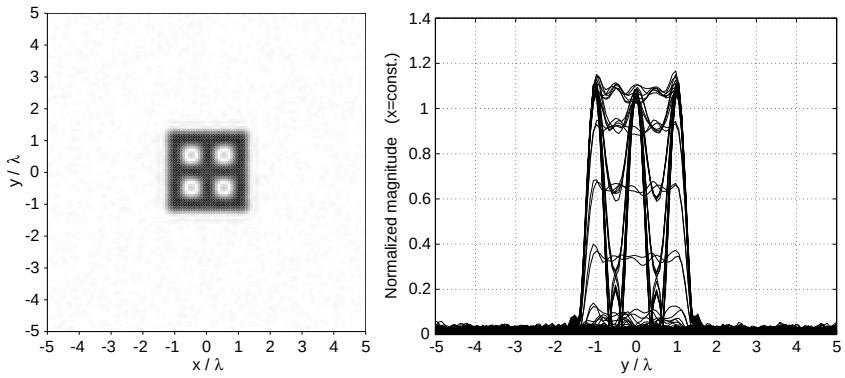

(a) Tikhonov regularization ($\alpha = 6 \times 10^{-3}$).

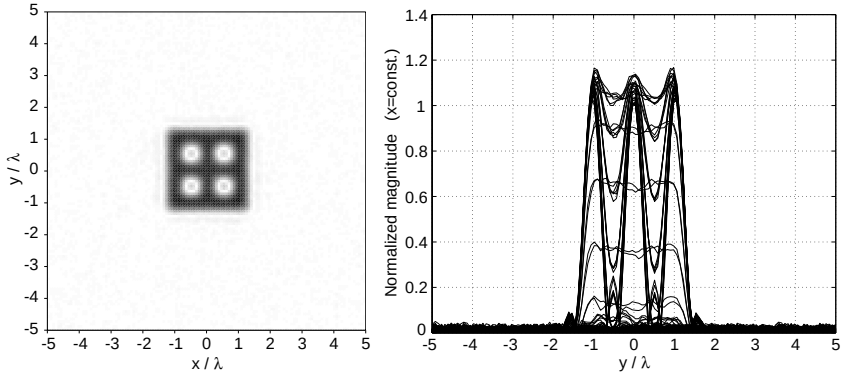

(b) Local extrapolation ($M = 5$, $\Delta\zeta = 0.125\,\lambda$).

Figure 4-8: Deblurring from noisy data (Helmholtz equation).

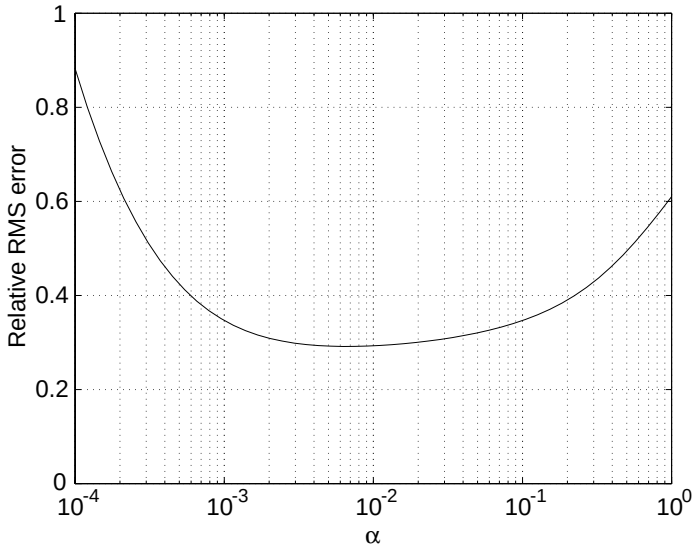

(a) Tikhonov regularization.

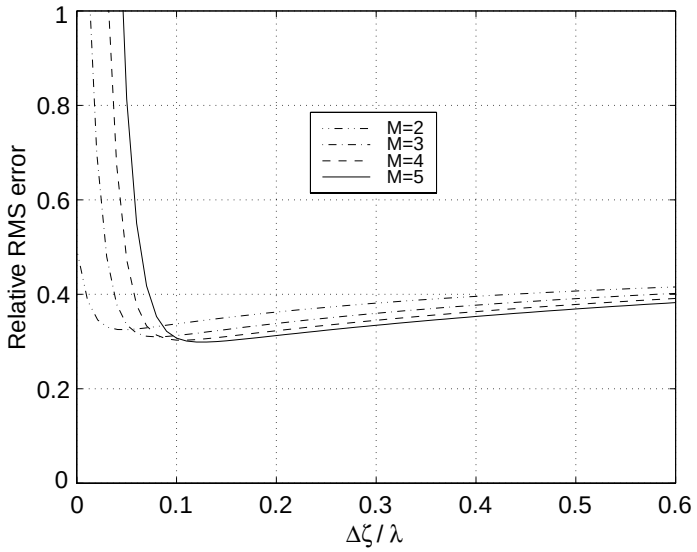

(b) Local extrapolation.

Figure 4-9: Relative RMS error vs. choice of parameters (Helmholtz equation).

4.5 Conclusions

The inverse convolutional, additive blurring process is shown to be unstable in general. The two regularized solutions described in this chapter do not incorporate any *a priori* knowledge on the unblurred data and, when applied to the examples of the planar Poisson kernel and its generalization to the dynamic case, yield results of comparable qualities. The observation that the local extrapolation scheme, in the cases considered, does not perform better than the deconvolution filter derived with the help of Tikhonov regularization is not surprising since the latter is equipped with an optimality property with respect to squared error. However, from the included discussions of the many physical and engineering applications it is clear that the local extrapolation scheme is not only a viable alternative to Tikhonov regularization but that its applicability is of value. For example, its underlying basic idea can be applied also to non-convolutional blurring processes which typically arise from non-planar geometries. Furthermore, the local extrapolation scheme including strategies for the choice of parameters can be formulated entirely in the space domain, without resorting to any numerical inverse Fourier transforms. Finally, the inherent localized nature of the extrapolation scheme may prove useful in certain situations, e. g., in the case of contamination of the data by localized noise.

Chapter 5

Inversion of guided-wave dispersion data with application to borehole acoustics including leaky waves

5.1 Introduction

A common picture for the propagation in waveguides comprises elementary waves bouncing between the boundaries of the structure, interfering constructively only for certain directions of the elementary wavevectors [28]. This determines the set of possible waveguide modes and their propagation constants. The propagation characteristics in the waveguide can therefore be expected to be closely related not only to the geometrical dimensions of the structure but also to the properties of the materials constituting the waveguide. In a different picture, the propagating field of an open waveguide penetrates into the surrounding medium, probing its constitutive parameters which influence the dispersive characteristics of the waveguide.

This motivates obtaining dispersion data with the goal of inferring unknown parameters of the configuration with the help of an appropriate inversion scheme. A conceptual advantage of this basic idea is the source independence of the dispersion in

waveguides which circumvents the need for modeling the transmitters and receivers of the envisioned apparatus. A disadvantage is that dispersion curves can be measured only indirectly, i. e., the inversion has to be preceded by a processing of the measured waveforms in order to extract the dispersion information which is then input to the inversion. This by itself can be difficult and prone to the introduction of uncertainties beyond those of the measurement. However, the advantage of source independence might justify the additional pre-processing step.

After describing a methodology for the inversion of general modal dispersion data, as an important practical example with considerable commercial potential, we take the case of borehole acoustics. A logging tool equipped with transmitters and an array of receivers is considered for recording time-domain waveforms that can be processed in order to separate the various arrivals and obtain samples of the pertinent dispersion curves [157, 158]. Previous approaches for the estimation of one or more parameters influencing the acousto-elastic wave propagation along the borehole include curve fitting procedures that are designed to minimize the error between the measured dispersion samples and synthetic data obtained from a forward model that uses an iterative modal search routine [159, 160]. The same forward model could be utilized to approximate the partial derivatives of the synthetic data with respect to the model parameters that are required in a systematic inversion algorithm. Alternatively, these sensitivity coefficients can be computed by numerical quadrature of appropriate perturbation integrals [159]–[162]. Perturbation theory and comparison of measured and computed dispersion curves plays an important role also in the interpretation of dispersion data influenced by nonlinear effects [163]–[165]. Kimball describes a processing scheme that is not based on direct curve fitting but, again, computed dispersions are required explicitly [166, 167].

For the linear case and in contrast to the methods listed above, in the present work we suggest minimizing a cost function that is derived directly from the determinant representing the boundary conditions at the interfaces of the waveguide model [168].

This cost function can be evaluated rapidly, without the need for any iterations, and allows the possibility of processing multi-frequency and multi-mode data in a potentially exact inversion. An arbitrary number of unknown parameters can be accommodated, provided that the data have sufficient sensitivity to these parameters. The theoretical investigations and numerical simulations carried out and described in this chapter do not incorporate any influence of the tool and only the simplest case of a fluid-filled borehole in a homogeneous and isotropic elastic rock formation is examined. We give a suitable formulation of the pertaining guidance condition and investigate the inversion with uncertain model parameters, the influence of bandwidth and noise, and the utilization of multi-frequency and multi-mode data. Finally, we turn to the leaky-wave modes of the fluid-filled borehole, a topic of general interest not only for the problem of inversion of borehole dispersions.

5.2 Parametric inversion of guided-wave modal dispersions

5.2.1 Modal dispersion curves

The guidance condition or characteristic equation for a two-dimensional waveguide structure invariant in the z direction and described by a parameter vector $\overline{x}$ containing geometrical and material constants can be written as

$$D(k_z, \omega, \overline{x}) = 0 \tag{5.1}$$

Here D is the determinant of the system matrix $\overline{\overline{L}}$ of the homogeneous linear system of equations that follows from matching the appropriate boundary conditions, k_z is the wavenumber in the direction of propagation, and ω is the angular frequency considered.

For a fixed parameter vector $\overline{x}$, it is meaningful to treat D as a function of two

independent complex variables [169], k_z and ω. When seeking steady-state solutions to problems involving a time-harmonic excitation, ω will be real. When computing transients utilizing a temporal Laplace transform both k_z and ω are in general complex, depending on the specific paths of integration chosen [170]–[176]. Due to the unique roles of time and space in a mixed initial boundary value problem k_z and ω are not exchangeable and no simple conversion exists between roots of (5.1) found in the complex k_z domain (for a fixed ω) and the complex ω domain (for a fixed k_z).

For open waveguides that allow radiation of energy away from the vicinity of the waveguide into the background medium (which only in the simplest situation is homogeneous) the complex ω and k_z domains are multi-sheeted Riemann surfaces, i. e., collections of complex planes connected across branch cuts (c. f., Section 5.5). Except for isolated singularities (branch points and poles), D is analytic on these surfaces.

If we choose a smooth curve Ω in the ω domain (typically, but not necessarily, the positive real axis), then the roots of (5.1) for some $\omega = \omega_0 \in \Omega$ constitute a set of modes. Choosing a particular mode by picking one of the roots, the dispersion relation $k_z(\omega, \overline{x})$ for this mode (with respect to Ω) is obtained by tracing the locus of the root in the k_z domain as ω moves away from ω_0 and along Ω. We can require that the dispersion curve $\{k_z(\omega, \overline{x}) : \omega \in \Omega\}$ also be a smooth function of ω in order to avoid a mix-up with other modes at possible points of degeneracy where different dispersion curves intersect.

This notion of dispersion leads directly to a numerical method for computing modal dispersion curves practically. Starting from ω_0, one or two (depending on whether ω_0 is an endpoint of Ω or not) sequences of sufficiently close frequencies on Ω are chosen. For example, by inspecting $|D(k_z, \omega_0, \overline{x})|$ in the k_z domain, a mode is selected and an initial guess for $k_z(\omega_0, \overline{x})$ obtained. In identifying local minima of $|D|$ as zeros, the minimum principle in complex analysis is helpful, assuring us that a local minimum of $|D|$ embedded into a neighborhood, for which it is the absolute

minimum and throughout which D is analytic, must be a zero:

> Minimum Principle [177]. If f is a non-constant analytic function on a bounded open set G and is continuous on the closure of G, then either f has a zero in G or $|f|$ assumes its minimum value on the boundary of G.

Using the initial guess, $k_z(\omega_0, \overline{x})$ is determined by finding the zero of D with the help of, e. g., the complex Newton-Raphson method [104]. Subsequently, stepping along Ω away from ω_0, all the samples of $k_z(\omega, \overline{x})$ are computed for each ω, using the k_z found at the previous frequency as initial guess. Thus the dispersion curve is obtained by this mode tracking procedure.

5.2.2 Inversion of modal dispersion data

We now turn to the inverse problem, i. e., estimation of the N unknown elements of $\overline{x}$ from bandlimited, possibly noisy samples of one or more dispersion curves. The number of parameters N to be determined can be less than the dimension of $\overline{x}$, e. g., in case some of the elements of $\overline{x}$ were obtained from other measurements.

Given M measured pairs (ω_i, k_{zi}) that satisfy

$$k_{zi} = k_z(\omega_i, \overline{x}) + n_i\,, \quad i = 1, 2, \ldots, M \tag{5.2}$$

where the n_i represent the noise in the data and, as in the case of multi-mode data, the $k_z(\omega_i, \overline{x})$ may belong to different modes, one possible formulation of the problem aims at minimizing the cost function

$$\|\overline{e}_0(\overline{x})\|^2 = \sum_{i=1}^{M} |k_z(\omega_i, \overline{x}) - k_{zi}|^2 \tag{5.3}$$

The problem with this approach is that every single evaluation of (5.3) for varying $\overline{x}$, in whatever optimization method employed, requires the M roots $k_z(\omega_i, \overline{x})$ which can be determined exactly only by iteration (Section 5.2.1). If one tries to avoid

these iterations by pre-computing a look-up table of k_z for all possible $\overline{x}$, ω, and modes—which itself might be an extensive computational task and may require a prohibitively large database—then the necessary interpolations during the inversion would preclude an exact answer even in the case of noise-free data. Furthermore, the implicit mode identification problem, i. e., relating each k_{zi} to the correct dispersion curves may complicate the situation. If k_{zi} is used as initial guess when iteratively computing $k_z(\omega_i, \overline{x})$, the wrong mode can be picked up accidentally.

The above difficulties can be avoided by solving the inverse problem without resorting to the dispersion curves $k_z(\omega, \overline{x})$ explicitly. We therefore suggest to pursue the minimization of the "guidance mismatch"

$$\|\overline{e}(\overline{x})\|^2 = \sum_{i=1}^{M} |D(k_{zi}, \omega_i, \overline{x})|^2 \tag{5.4}$$

It is obvious that the cost function defined by (5.4), for the case of noise-free data, can be made zero, similar to (5.3). For noisy data, the least-squares problem can be solved by applying the Gauss-Newton method [112]. The partial derivatives in the Jacobian are typically replaced by finite differences unless the structure considered is simple enough so that the differentiations can be carried out analytically. It is seen that, whereas the cost function in (5.3) is of the same form as in curve fitting problems, in (5.4) the data k_{zi} and thus the noise influence $\overline{e}$ in a nonlinear fashion.

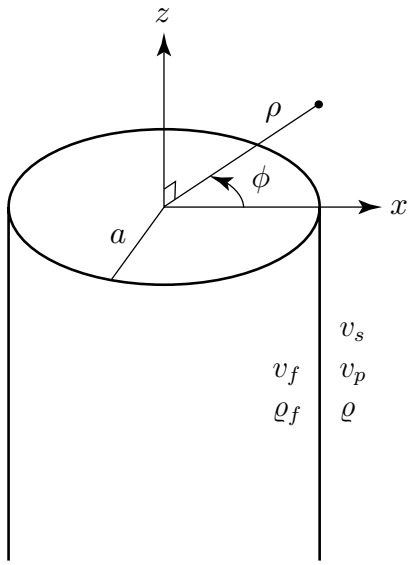

Figure 5-1: A fluid-filled borehole in an elastic, homogeneous, and isotropic rock formation, forming a circularly cylindrical fluid-solid interface.

5.3 Sonic guidance condition for a fluid-filled borehole

5.3.1 Formulation for forward and inverse dispersion analysis

For linearized acoustic wave propagation along a fluid-filled borehole in an elastic, homogeneous, and isotropic rock formation (Fig. 5-1), $\overline{\overline{L}}$ is 4×4 (see below) and

$$\overline{x} = [\, a, v_s, v_p, v_f, \varrho_{fr} \,] \tag{5.5}$$

with a the borehole radius, v_s the shear wave velocity in the formation, v_p and v_f the compressional wave velocities in the formation and the fluid, respectively, and $\varrho_{fr} = \varrho_f / \varrho$ the ratio of mass densities of the fluid and the formation (relative fluid mass density, usually less than one).

The four scalar boundary conditions at an interface between two elastic media where transverse slip may occur require continuity of the normal component of the particle velocity vector $\overline{v}$, and continuity of the normal component and vanishing of the tangential components of the traction vector $\overline{\overline{\tau}} \cdot \hat{n}$, where $\overline{\overline{\tau}}$ is the symmetric stress tensor and $\hat{n}$ the unit vector normal to the interface [178]. An inviscid fluid can be considered as special case of an elastic medium with zero shear wave velocity. In this case, the stress tensor specializes to

$$\overline{\overline{\tau}} = -p\,\overline{\overline{I}} \tag{5.6}$$

with p the fluid pressure and $\overline{\overline{I}}$ the identity tensor. Thus the boundary conditions at the fluid-solid interface in Fig. 5-1 are continuity of $\hat{\rho} \cdot \overline{v}$ and

$$\hat{\rho} \cdot \overline{\overline{\tau}} \cdot \hat{\rho} = -p \tag{5.7}$$

$$\hat{\phi} \cdot \overline{\overline{\tau}} \cdot \hat{\rho} = 0 \tag{5.8}$$

$$\hat{z} \cdot \overline{\overline{\tau}} \cdot \hat{\rho} = 0 \tag{5.9}$$

Starting from [179], we adopt an $\mathrm{e}^{\mathrm{i}\,k_z z - \mathrm{i}\omega t}$ space-time dependence by using the identity relating the Hankel functions of the first and second kind [83]

$$\mathrm{H}_n^{(1)}(\zeta^*) = \left[\mathrm{H}_n^{(2)}(\zeta)\right]^* \tag{5.10}$$

where ζ is a generic complex variable, the asterisk denotes complex conjugation, and $n = 0, 1, \ldots$ is the azimuthal mode order. Some rearranging leads to $\overline{\overline{L}} = [L_{ij}]$ with

$$L_{11} = k_{f\rho} a\, \mathrm{J}_{n+1}(k_{f\rho} a) - n\, \mathrm{J}_n(k_{f\rho} a) \tag{5.11}$$

$$L_{21} = \varrho_{fr}\, (k_s a)^2\, \mathrm{J}_n(k_{f\rho} a) \tag{5.12}$$

$$L_{31} = 0 \tag{5.13}$$

$$L_{41} = 0 \tag{5.14}$$

$$
\begin{aligned}
L_{12} &= n - A_n(k_{p\rho}a) && (5.15)\\
L_{22} &= 2\left[n\,(n-1) + (k_z a)^2 + A_n(k_{p\rho}a)\right] - (k_s a)^2 && (5.16)\\
L_{32} &= 2n\,[1 - n + A_n(k_{p\rho}a)] && (5.17)\\
L_{42} &= 2\mathrm{i}\,k_z a\,[A_n(k_{p\rho}a) - n] && (5.18)
\end{aligned}
$$

$$
\begin{aligned}
L_{13} &= -\mathrm{i}\,k_z a && (5.19)\\
L_{23} &= 2\mathrm{i}\,k_z a\,[n + 1 - B_n(k_{s\rho}a)] && (5.20)\\
L_{33} &= \mathrm{i}\,k_z a\,[2\,(n+1) - B_n(k_{s\rho}a)] && (5.21)\\
L_{43} &= (k_s a)^2 - 2\,(k_z a)^2 - n\,B_n(k_{s\rho}a) && (5.22)
\end{aligned}
$$

$$
\begin{aligned}
L_{14} &= n && (5.23)\\
L_{24} &= 2n\,[n - 1 - A_n(k_{s\rho}a)] && (5.24)\\
L_{34} &= (k_{s\rho}a)^2 - 2n\,(n-1) - 2\,A_n(k_{s\rho}a) && (5.25)\\
L_{44} &= -n\mathrm{i}\,k_z a && (5.26)
\end{aligned}
$$

where $\mathrm{J}_n(\zeta)$ denotes the Bessel function of the first kind and order n and we introduced the auxiliary functions

$$
\begin{aligned}
A_n(\zeta) &= \zeta\,\mathrm{H}^{(1)}_{n+1}(\zeta)/\mathrm{H}^{(1)}_n(\zeta) && (5.27)\\
B_n(\zeta) &= \zeta\,\mathrm{H}^{(1)}_n(\zeta)/\mathrm{H}^{(1)}_{n+1}(\zeta) = \zeta^2/A_n(\zeta) && (5.28)
\end{aligned}
$$

The normalized radial wavenumbers $k_{\alpha r}$ satisfy the dispersion relations

$$
k_{\alpha r}^2 = k_\alpha^2 - k_z^2\,,\ \alpha = s, p, f \qquad (5.29)
$$

where $k_\alpha = \omega/v_\alpha$.

For proper modes, i. e., modes that are bound to the surface of the open waveguide (the fluid-formation interface) and that are either radially evanescent or represent an outgoing, radially decaying wave and which thus satisfy the radiation condition at infinity, we have $\mathrm{Re}\, k_{\alpha r} \geq 0$ and $\mathrm{Im}\, k_{\alpha r} > 0\,,\ \alpha = s, p$.

The choice of sign for $k_{f\rho}$ only contributes a factor of $(-1)^n$ to the determinant and thus does not influence the location of the roots of the characteristic equation. In fact, the associated branch points for D in the complex k_z domain (for a fixed ω) and the complex ω domain (for a fixed k_z) would be removable after multiplication of the determinant by, say, $(k_{f\rho}a)^n$.

The elements of the boundary condition system matrix, (5.15)–(5.26), were formulated with care to avoid infinite values as $k_{\alpha r} \to 0\,,\ \alpha = s, p$. Since we are interested in minimizing the cost function in (5.4), we should also remove zeros of the determinant that do not correspond to guided wave modes in order to avoid the introduction of unwanted minima.

For $n > 0$, column 1 of $\overline{\overline{L}}$ as given by (5.11)–(5.14) vanishes as $k_{f\rho} \to 0$. Even if, in an inversion, the component v_f of $\overline{x}$ is not varied because this parameter might already be known (for a water-filled borehole, $v_f = 1{,}500\,\mathrm{m/s}$) this can be a problem when computing dispersion curves. The zero can be removed by dividing column 1 by $k_{f\rho}a$.

For all n and as $k_{s\rho} \to 0$, the determinant based on the above formulation vanishes in a more subtle way. In view of

$$\lim_{\zeta \to 0} A_n(\zeta) = 2n \tag{5.30}$$

$$\lim_{\zeta \to 0} B_n(\zeta) = 0 \tag{5.31}$$

we find that column 3 and column 4 become linearly dependent as $k_s \to k_z$. By adding

$$\frac{n\, L_{i3}}{\mathrm{i}\, k_z a}$$

to L_{i4} and dividing the result by its third element the following new formulation for the fourth column of $\overline{\overline{L}}$ is obtained, as a replacement of (5.23)–(5.26):

$$L_{14} = 0 \tag{5.32}$$

$$L_{24} = n\left[1 - \frac{(k_{s\rho}a)^2 - (n-2)\,B_n(k_{s\rho}a)}{4n + (k_{s\rho}a)^2 - 2\,A_n(k_{s\rho}a) - n\,B_n(k_{s\rho}a)}\right] \tag{5.33}$$

$$L_{34} = 1 \tag{5.34}$$

$$L_{44} = \frac{n\mathrm{i}}{k_z a}\,\frac{n\,B_n(k_{s\rho}a) - (k_{s\rho}a)^2}{4n + (k_{s\rho}a)^2 - 2\,A_n(k_{s\rho}a) - n\,B_n(k_{s\rho}a)} \tag{5.35}$$

The fourth-order determinant with $L_{14} = L_{31} = L_{41} = 0$ and $L_{34} = 1$ can then be evaluated by expanding down the first column of the matrix and across the first row of the two 3×3 minors, yielding

$$\begin{aligned} D = {} & L_{11}\left\{L_{22}\left[(L_{33}\,L_{44}) - L_{43}\right] + L_{23}\left[L_{42} - (L_{32}\,L_{44})\right]\right. \\ & \left. + L_{24}\,(L_{32}\,L_{43} - L_{33}\,L_{42})\right\} \\ & - L_{21}\left\{L_{12}\left[(L_{33}\,L_{44}) - L_{43}\right] + L_{13}\left[L_{42} - (L_{32}\,L_{44})\right]\right\} \end{aligned} \tag{5.36}$$

5.3.2 High-frequency limit

We can verify our formulation by deriving the equation for the Scholte wave velocity v_{Sch} (the speed of a surface wave along a *planar* fluid-solid interface) where

$$k_z = k_{\mathrm{Sch}} = \frac{\omega}{v_{\mathrm{Sch}}} \tag{5.37}$$

is expected to satisfy the guidance condition for the fluid-filled borehole in the high-frequency limit, $\omega \to \infty$, when all wavenumbers become so large that the local curvature of the fluid-solid interface is negligible. Using

$$A_n(\zeta) \sim -\mathrm{i}\zeta \tag{5.38}$$

$$B_n(\zeta) \sim \mathrm{i}\zeta \tag{5.39}$$

as $|\zeta| \to \infty$ and

$$\frac{\mathrm{J}_{n+1}(k_{f\rho}a)}{\mathrm{J}_n(k_{f\rho}a)} \sim \pm\mathrm{i} \tag{5.40}$$

as $\mathrm{Im}\, k_{f\rho} \to \pm\infty$, we obtain as $\omega \to \infty$ and for $\mathrm{Im}\, k_{f\rho} > 0$

$$\left(k_z^2 - k_{s\rho}^2\right)^2 + 4\, k_{s\rho}\, k_{p\rho}\, k_z^2 + \varrho_{fr}\, k_s^4\, k_{p\rho}\,/k_{f\rho} = 0 \tag{5.41}$$

which, as expected, is independent of n, a, and ω (the frequency ω can be dropped from the equation), and which checks with [180]. It is noted that, for real v_{Sch} and v_f, (5.40) implies $v_{\mathrm{Sch}} < v_f$, and—more stringent—for the surface wave to be bound to the fluid-solid interface

$$v_{\mathrm{Sch}} < v_{s,p,f} \tag{5.42}$$

is required.

5.4 Parametric inversion of borehole dispersions

In the following we will apply the inversion method introduced in Section 5.2.2 to the physical model described by the determinant in Section 5.3.1. Although this example is drawn from acoustics, the methodology applies equally well to electromagnetics and other areas that allow for wave guidance; different waveguide structures can be examined by considering the appropriate guidance conditions. As mentioned above, the choice of the application example is driven by the significant industrial application of borehole logging. In the rest of the paper $\omega = 2\pi f$ is real and positive.

In the cases studied, we assume the practically relevant parameters for a fast and a slow formation considered previously in [179]; they are repeated in Table 5.1 for reference. A formation is classified as fast or slow depending on whether the shear wave velocity in the formation, v_s, is greater or less than the fluid wave velocity v_f. The Scholte wave velocities v_{Sch} as obtained iteratively from (5.41) are also given in Table 5.1 and found to be in compliance with (5.42).

	a [cm]	v_s [m/s]	v_p [m/s]	v_f [m/s]	ϱ/ϱ_f	v_{Sch} [m/s]
fast	10.16	2,032	3,658	1,500	2.350	1,439.6
slow	10.16	508	1,890	1,500	2.054	452.2

Table 5.1: Parameters for a water-filled borehole in a fast and a slow formation. Given also are the resulting Scholte wave velocities v_{Sch}.

5.4.1 Inversion with uncertain model parameters

We now concentrate on the inversion of the formation shear wave velocity v_s, a quantity of particular practical interest in the exploration of hydrocarbons, and investigate the effect of systematic errors introduced into the model parameters borehole radius a and formation compressional wave velocity v_p, where in the first case the exact v_p is assumed to be known and in the second case the exact a. The parameters fluid compressional wave velocity v_f and relative fluid mass density ϱ_{fr} are provided without error.

For noise-free data, it is sufficient to provide a single "measurement" in order to determine the one parameter v_s ($M = N = 1$). This point is taken from the dispersion of the lowest-order mode with $n = 1$, which can be excited by a dipole source placed on the borehole axis and which is known as flexural wave dispersion [160, 181]. For the parameters in Table 5.1, the flexural dispersions are plotted in Fig. 5-2 (these curves can also be found in [179]) where phase slowness is defined as $\mathrm{Re}\{k_z\}/\omega$. Generally speaking, slowness is the reciprocal of velocity. The dashed horizontal lines labeled as "S", "P", "F", and "Sch" show the slownesses corresponding to v_s, v_p, v_f, and v_{Sch}, respectively. "S" is the low-frequency asymptote of the flexural dispersion while "Sch" is approached as $\omega \to \infty$.

The results in Fig. 5-3 for four different frequencies at which the sample of the dispersion curves in Fig. 5-2 was obtained show that if in the inversion the assumed borehole radius is larger than the true borehole radius (leading to the dispersions in Fig. 5-2) then the inverted shear wave velocity exhibits a positive error; the opposite is

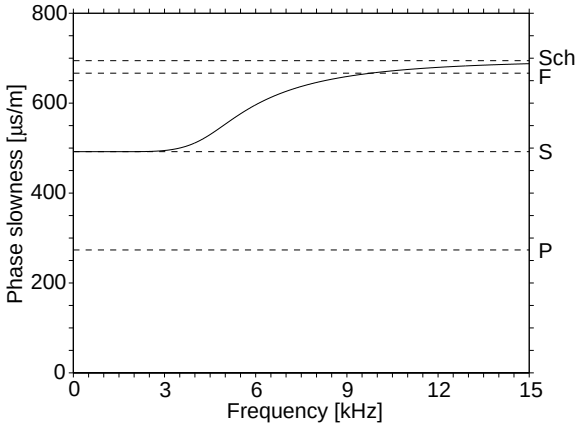

(a) Fast formation.

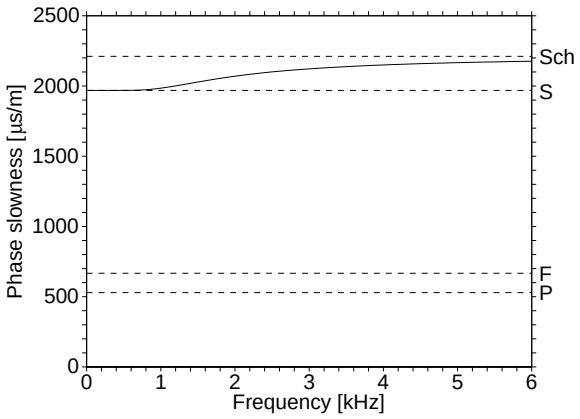

(b) Slow formation.

Figure 5-2: Flexural dispersions for a water-filled borehole.

true for a too small borehole radius. Starting off with a relatively small absolute value at the lowest frequencies considered (4 kHz for the fast formation and 1 kHz for the slow formation), the error in inverted v_s initially grows as the frequency increases and then tends to smaller values again. This is consistent with the asymptotic behavior of the flexural dispersion curve which for both low and high frequencies approaches values that are independent of a. The relative errors in inverted shear wave velocity for the slow formation are found to be about ten times smaller than for the fast formation where in the latter case the ratio of error in shear wave velocity to error in borehole radius can be close to one. This shows that in the slow formation an accurate estimate of v_s can be obtained even when the value of a is uncertain. In the fast formation a good estimate of the borehole radius is required to obtain an accurate inversion result. On the other hand, reversing the roles of v_s and a, if v_s in the fast formation is known with little error then the dispersion information for intermediate frequencies could be used to find an accurate estimate of a. This would not work for the slow formation where the flexural dispersion is much less sensitive to borehole radius.

Similar curves are found for the inversion of v_s when the assumed formation compressional wave velocity v_p exhibits an error (Fig. 5-4). Positive errors in v_p yield a result for v_s that is smaller than the exact value. The magnitude of the error of inverted v_s is found to be increasing with frequency. This is consistent with the fact that the low-frequency asymptote of the flexural dispersion is independent of v_p while the Scholte wave velocity v_{Sch} depends on v_p. In fact, given v_s, v_f, ϱ_{fr}, and v_{Sch}, (5.41) can be rearranged to give an explicit expression for v_p. The result is

$$v_p^{-2} = v_{\mathrm{Sch}}^{-2} - \frac{\left(2\, v_{\mathrm{Sch}}^{-2} - v_s^{-2}\right)^4}{\left[4\, v_{\mathrm{Sch}}^{-2} \left(v_{\mathrm{Sch}}^{-2} - v_s^{-2}\right)^{1/2} - \varrho_{fr}\, v_s^{-4} \left(v_{\mathrm{Sch}}^{-2} - v_f^{-2}\right)^{-1/2}\right]^2} \tag{5.43}$$

As with the dependence of inverted shear wave velocity on the error in borehole

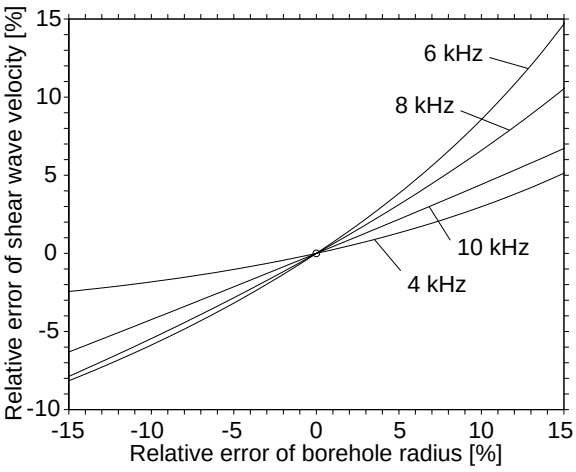

(a) Fast formation.

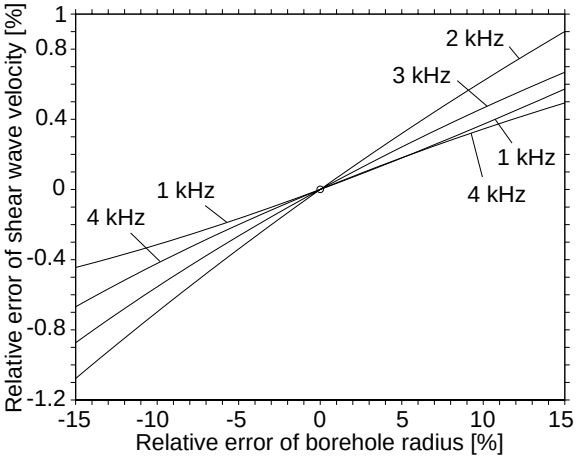

(b) Slow formation.

Figure 5-3: Relative error in inverted formation shear wave velocity for varying relative error of assumed borehole radius (flexural dispersion).

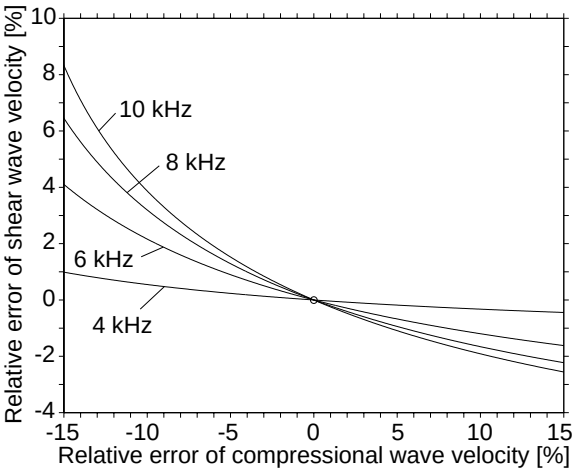

(a) Fast formation.

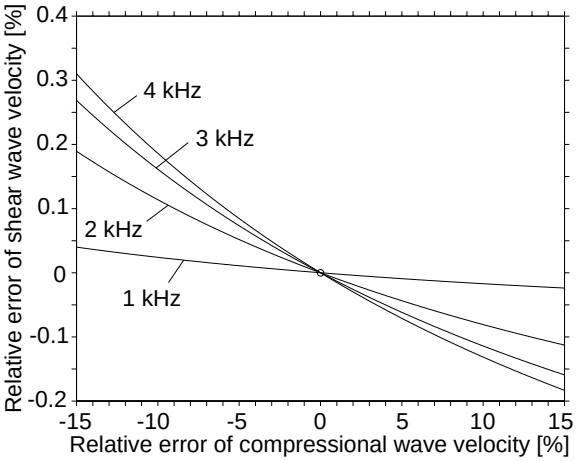

(b) Slow formation.

Figure 5-4: Relative error in inverted formation shear wave velocity for varying relative error of assumed formation compressional wave velocity (flexural dispersion).

radius, errors in formation compressional wave velocity have a much larger influence on the inverted v_s in the case of the fast formation. Comparing Fig. 5-4 with Fig. 5-3, one notes that, in general, the sensitivity of the flexural dispersion data to v_p is smaller than the sensitivity to a. Thus the flexural dispersion for the slow formation is found to be insensitive to both a and v_p while in the case of the fast formation it is sensitive to a and moderately sensitive to v_p. The shear wave velocity v_s acting as the low-frequency asymptote has of course a strong influence on both dispersions. Similar conclusions can be found in [160] where a perturbation model is used to calculate the sensitivity of the flexural dispersion curve to small changes of the parameters.

While from Fig. 5-3 and Fig. 5-4 we can read off detailed information about the error of the inversion as it depends nonlinearly on errors of the underlying model, with frequency as parameter, in Fig. 5-5 we show results for continuously varying frequency (the frequency ranges displayed are the same as in Fig. 5-2). The relative sensitivities plotted are defined, for arbitrary frequency, as the slopes of the corresponding curves in Fig. 5-3 and Fig. 5-4 at the origin, that represents the case of an inversion without error in the assumed model. These relative sensitivities thus give the error of the otherwise exact inversion of shear wave velocity for small errors in the model parameters. For example, the relative sensitivity with respect to borehole radius in the fast formation [Fig. 5-5(a)] peaks near 6 kHz at around 70 %. This means that for an inversion with 1 % error in borehole radius we would expect a result with 0.7 % error in shear wave velocity, assuming that all other parameters are known exactly.

Stoneley dispersion

The Stoneley mode [182] is the lowest-order axisymmetric mode ($n = 0$) and can be excited by a monopole source placed on the borehole axis. The dispersion curves for the fast and the slow formation are plotted in Fig. 5-6 and can also be found in [179]. For comparison, the flexural dispersions of Fig. 5-2 are also shown in Fig. 5-6. At the high-frequency end of the spectrum, the Stoneley mode approaches the

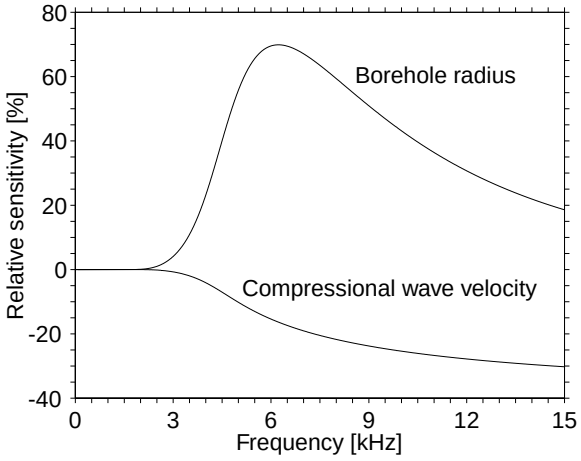

(a) Fast formation.

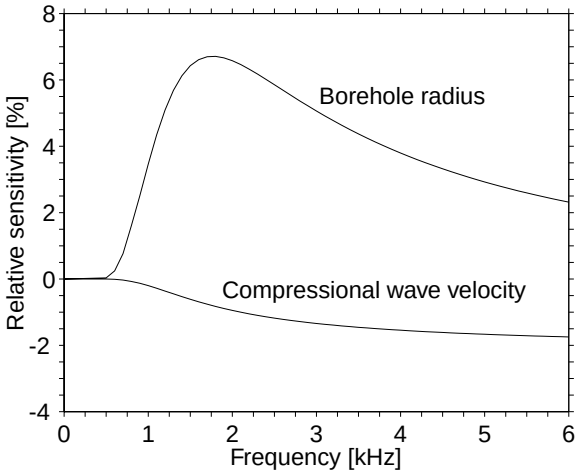

(b) Slow formation.

Figure 5-5: Frequency-dependent relative sensitivity of inverted formation shear wave velocity to model error in borehole radius or formation compressional wave velocity (flexural dispersion).

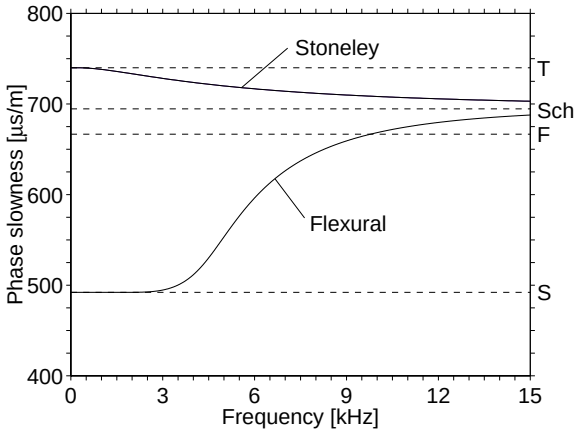

(a) Fast formation.

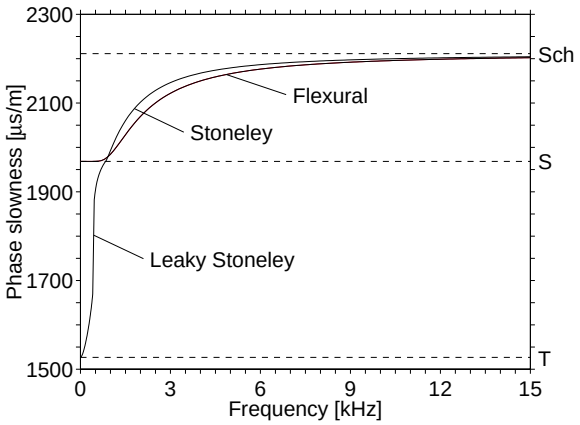

(b) Slow formation.

Figure 5-6: Stoneley dispersions for a water-filled borehole, together with the flexural dispersions of Fig. 5-2.

	v_t [m/s]	cutoff [kHz]
fast	1,351.5	none
slow	655.0	0.835

Table 5.2: The resulting tube wave velocities v_t and Stoneley cutoff frequencies for the configurations with parameters given in Table 5.1 and as indicated in Fig. 5-6.

same asymptotic value as the flexural dispersion, given by the Scholte wave velocity v_{Sch} [recall that (5.41) is independent of the azimuthal mode order n]. The dashed horizontal line labeled "T" in each subfigure of Fig. 5-6, shown in addition to the asymptotes in Fig. 5-2, indicates the slowness corresponding to the tube wave velocity v_t. The tube wave velocity is the low-frequency asymptote of the Stoneley dispersion and given by [182, 183]

$$v_t^{-2} = v_f^{-2} + \varrho_{fr}\, v_s^{-2} \tag{5.44}$$

The resulting tube wave velocities for the parameters in Table 5.1 can be found in Table 5.2. According to (5.44), the tube wave velocity is always slower than the fluid compressional wave velocity v_f and, in a fast formation, slower than the formation shear wave velocity v_s [see the introduction to Section 5.4 and Fig. 5-6(a)]. However, in a slow formation, $v_t > v_s$ is possible, namely if

$$\frac{v_s}{v_f} < \sqrt{1 - \varrho_{fr}} \tag{5.45}$$

as follows from the definition (5.44) under the assumption $\varrho_{fr} < 1$. Since for the high-frequency asymptote, $v_{\mathrm{Sch}} < v_s$ as stated in (5.42), under the condition (5.45) the Stoneley dispersion crosses the shear wave velocity at some cutoff frequency below which the wave is leaky, with $k_{s\rho}$ and k_z in (5.29) complex. This phenomenon can be observed in Fig. 5-6(b), with the cutoff frequency given in Table 5.2. Leaky borehole modes are discussed in detail in Section 5.5. We have included the leaky Stoneley mode into the results of this section for the sake of completeness, however, we leave

out the plot of the associated modal attenuation as defined in (5.47) below.

The results in Fig. 5-6 show that the qualitative behavior of the Stoneley dispersion in the two formations considered is completely different. In the slow formation, the non-leaky portion of the Stoneley dispersion is close to the flexural dispersion while this is not the case in the fast formation. While the phase slowness of the Stoneley mode in Fig. 5-6(a) is monotonically decreasing, it is monotonically increasing in Fig. 5-6(b).

The similarities and differences between Stoneley and flexural dispersions carry over to the results in Fig. 5-7 and 5-8 that are Stoneley results analogous to the results displayed in Fig. 5-3 and 5-4 for the flexural dispersion. Note the opposite signs in Fig. 5-7(a) as compared with Fig. 5-3 and 5-7(b). However, positive errors in formation compressional wave velocity lead to negative errors in inverted formation shear wave velocity in all cases (Fig. 5-4 and 5-8).

The frequency-dependent relative sensitivities for inverting Stoneley dispersion data that are depicted in Fig. 5-9 and 5-10 have a definition and meaning similar to the sensitivities plotted previously for the flexural dispersion (Fig. 5-5). The data of the four curves in Fig. 5-5 are shown again in Fig. 5-9 and 5-10 for comparison. Since the tube wave velocity v_t as given by (5.44) is independent of borehole radius a and formation compressional wave velocity v_p, all Stoneley sensitivity curves shown go to zero as the frequency tends to zero. The sensitivity of inverted shear wave velocity to an error in the assumed borehole radius for the fast formation [Fig. 5-9(a)] is generally smaller in magnitude when inverting Stoneley dispersion data than when using flexural dispersion data, unless low frequencies are considered. The magnitude of the sensitivity of inverted shear wave velocity to an error in assumed v_p for the fast formation [Fig. 5-9(b)] is somewhat larger for the Stoneley dispersion as compared with the flexural dispersion. Setting the leaky Stoneley results aside, the most striking feature of Fig. 5-10 for the slow formation is the general closeness of the sensitivity curves for the Stoneley and the flexural dispersions. The sharp peaks of the relative

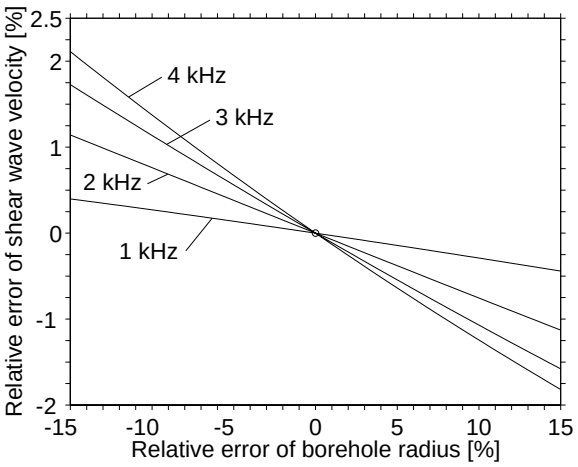

(a) Fast formation.

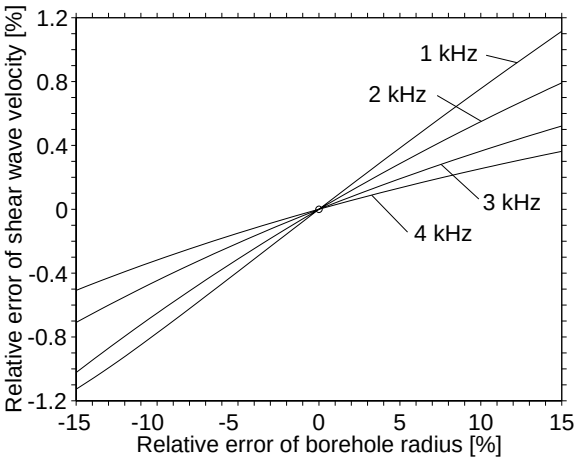

(b) Slow formation.

Figure 5-7: Relative error in inverted formation shear wave velocity for varying relative error of assumed borehole radius (Stoneley dispersion).

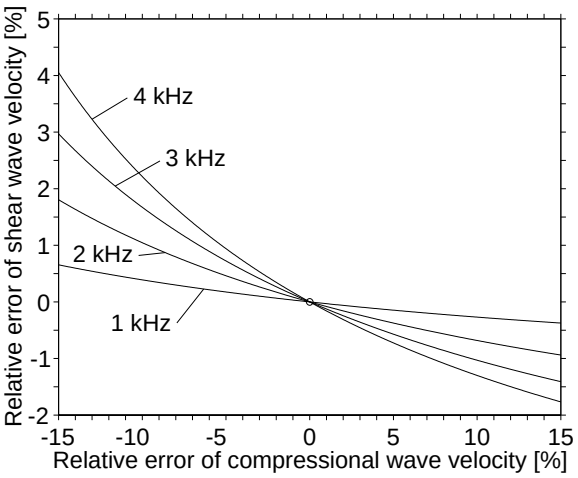

(a) Fast formation.

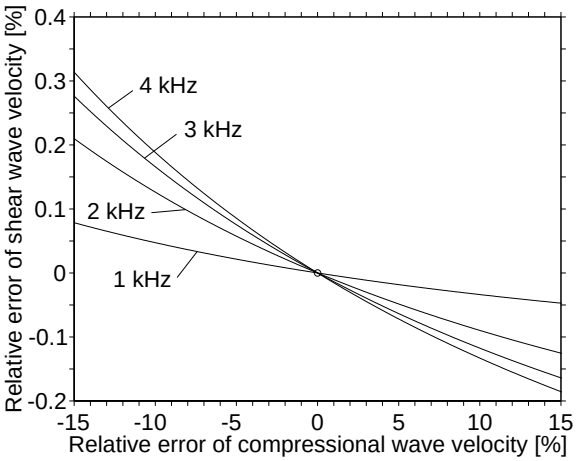

(b) Slow formation.

Figure 5-8: Relative error in inverted formation shear wave velocity for varying relative error of assumed formation compressional wave velocity (Stoneley dispersion).

sensitivities for the leaky Stoneley mode in Fig. 5-10 occur at that frequency where the dispersion curve in Fig. 5-6 goes through a very steep section.

5.4.2 Bandwidth and noise

It is important to realize that sensitivity of the dispersion data to several parameters (e. g., v_s, v_p, and a for the fast formation) does not necessarily allow the simultaneous inversion of the data for these parameters. For example, if the data depend only on the ratio v_s/v_p and are sensitive to this ratio then they will be sensitive to changes in v_s with v_p fixed, and vice versa, but simultaneous determination of both parameters will be impossible due to the non-uniqueness of the problem. Simultaneous inversion for N parameters requires, beside $M \geq N$ where M is the number of data points, a sufficient degree of independent information about the individual parameters in the data. Guided by principles of communications engineering, it is quite natural for the problem at hand to try adding more information to the data by sampling the dispersion curve with a larger bandwidth.

For the example of the fast formation and for inverting v_s and v_p from flexural dispersion data, we will examine if the increased technological demands of designing a wideband system would be worth pursuing.

We choose a fixed spacing $\Delta f = 200\,\mathrm{Hz}$ between the samples which are centered about $f_c = 6.5\,\mathrm{kHz}$ [a point to the right of the turning point of the dispersion curve in Fig. 5-2(a)], and, starting with $M = 2$, add points at both ends of the sampled interval, extending the bandwidth by 400 Hz at each step. For a fixed systematic model error in formation compressional wave velocity v_p of $-10\,\%$ and with no noise added to the data, Table 5.3 shows the error in inverted shear wave velocity v_s with increasing bandwidth or, equivalently, number of samples M. It is seen that the inversion result is practically independent of bandwidth and the resulting error, which could as well be read off from Fig. 5-4(a), is determined by the error in v_p. Table 5.3 also provides the number of iterations required in the application of the Gauss-Newton

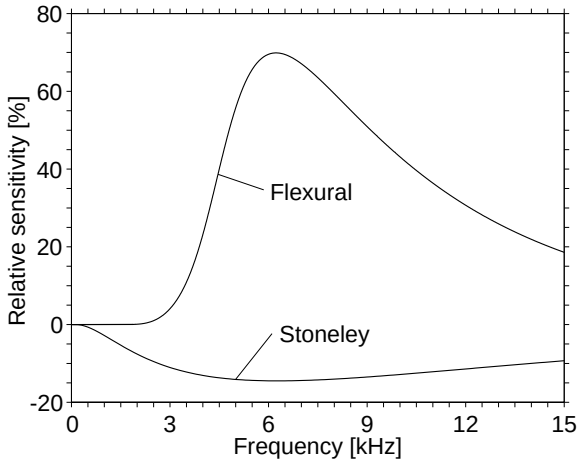

(a) Borehole radius.

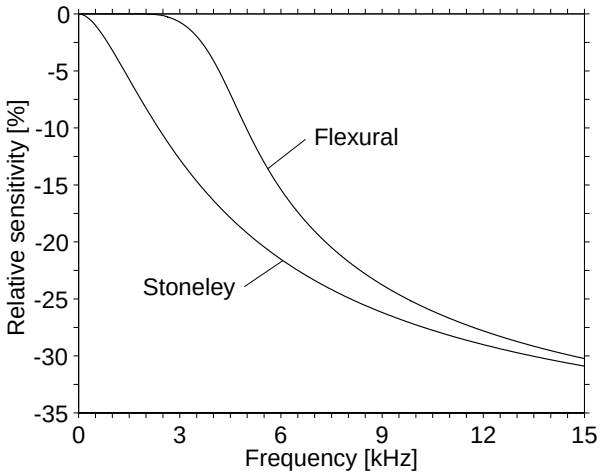

(b) Formation compressional wave velocity.

Figure 5-9: Frequency-dependent relative sensitivity of inverted formation shear wave velocity to model error in borehole radius or formation compressional wave velocity using Stoneley or flexural dispersion data (fast formation).

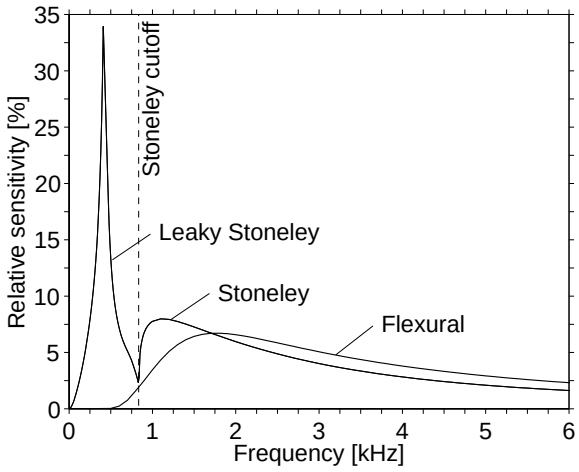

(a) Borehole radius.

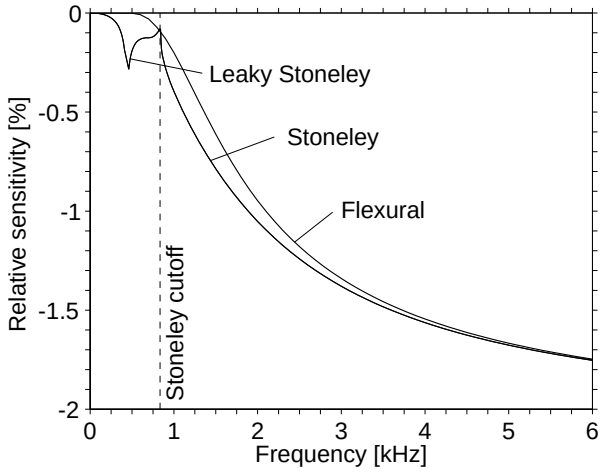

(b) Formation compressional wave velocity.

Figure 5-10: Frequency-dependent relative sensitivity of inverted formation shear wave velocity to model error in borehole radius or formation compressional wave velocity using Stoneley or flexural dispersion data (slow formation).

Bandwidth [kHz]	M	Inverted v_s [m/s]	Error [%]	Iter.
0.2	2	2,082.3	2.5	4
0.6	4	2,082.6	2.5	5
1.0	6	2,083.0	2.5	5
1.4	8	2,083.7	2.5	6
1.8	10	2,084.4	2.6	6
2.2	12	2,085.3	2.6	6
2.6	14	2,086.3	2.7	6
3.0	16	2,087.3	2.7	5

Table 5.3: Effect of increasing bandwidth on the inversion for formation shear wave velocity with $-10\,\%$ error in formation compressional wave velocity (fast formation, flexural dispersion, $f_c = 6.5\,\mathrm{kHz}$, no noise).

method. The initial guess for v_s is obtained directly from the data by taking it to be a few percent larger than the largest "measured" phase velocity.

In order to achieve a more accurate result for v_s and remove the uncertainty due to v_p, one can try to invert the data for the two parameters simultaneously ($N = 2$). In the present noise-free case and for all bandwidths in Table 5.3, this gives back the exact values for v_s and v_p listed in Table 5.1 and originally used to generate the dispersion curve in Fig. 5-2(a). This potentially exact inversion of dispersion data is an important feature of the methodology employed in this thesis. However, the condition numbers of the inversion matrix in Table 5.4 show that the problem at hand is not well posed, i. e., the successful simultaneous inversion for v_s and v_p relies on the fact that the supplied data contain no errors. The condition number in the context here is defined as the ratio of the largest to the smallest of the eigenvalues of $\overline{\overline{J}}_0^{\,\mathrm{T}} \cdot \overline{\overline{J}}_0$ where $\overline{\overline{J}}_0$ is the $2M \times N$ real Jacobian matrix at the start of the Gauss-Newton iteration. The reciprocal of this condition number is an indicator of how well defined the solution to the minimization problem is in terms of uniqueness. As seen from the data in Table 5.4, increasing the bandwidth when sampling the flexural dispersion yields a considerable improvement of the condition number for the simultaneous inversion of

Bandwidth [kHz]	M	Condition number
0.2	2	582,000
0.6	4	64,400
1.0	6	18,800
1.4	8	7,780
1.8	10	3,900
2.2	12	2,210
2.6	14	1,370
3.0	16	903

Table 5.4: Effect of increasing bandwidth on the conditioning of the problem of simultaneous inversion for formation shear and compressional wave velocities (fast formation, flexural dispersion, $f_c = 6.5\,\mathrm{kHz}$, no noise).

v_s and v_p. But even for 3 kHz bandwidth, after a decrease by about three orders of magnitude, the condition number is still much larger than the ideal unity.

When examining the cost functions associated with the cases in Table 5.4 as functions of v_s and v_p, it is found that, while there is a minimum at the correct position which is accurately determined by the Gauss-Newton iteration procedure, it is located inside a long valley with a shallow bottom [c. f., Fig. 5-11(b) below]. Small perturbations in the data therefore can lead to a great displacement of the minimum's location and thus to an inaccurate inversion result. This effect is similar to the determination of the location of the intersection point of two almost parallel lines in a plane; small changes in the parameters describing the lines can move the intersection point far away from its original position.

The detrimental effect of ill conditioning in the presence of noise is demonstrated by the results in Table 5.5. Pseudo-random white Gaussian noise is added to the real-valued slowness data with 3 kHz bandwidth, with the noise level defined as relative root mean squared (RMS) error. It is seen that only for the cases of zero and 0.5 % noise, reasonable inversion results are obtained. For further increase of the noise level a rapid degradation is observed.

Noise [%]	Inverted v_s [m/s]	Inverted v_p [m/s]	Error v_s [%]	Error v_p [%]	Iter.
0.0	2,032.0	3,658.0	0.0	0.0	7
0.5	2,023.7	3,784.1	−0.4	3.5	7
1.0	2,227.9	2,969.8	9.6	−18.8	7
1.5	2,981.3	3,057.0	46.7	−16.4	18

Table 5.5: Effect of increasing noise level on the simultaneous inversion for formation shear and compressional wave velocities (fast formation, flexural dispersion, $f_c = 6.5\,\text{kHz}$, 16 samples with 3 kHz bandwidth).

Returning to the case of inversion for formation shear wave velocity with fixed $-10\,\%$ error in formation compressional wave velocity (as in Table 5.3), the results documented in Table 5.6 show that the inversion with $N = 1$ is robust against noise in the data. Because only one realization of the noise process is considered, after an initial increase of the resulting error in inverted shear wave velocity with increasing noise level, we observe an improvement of the error; this would not be expected on average.

Similar results as described above are found when inverting the flexural dispersion data for the shear wave velocity and the borehole radius simultaneously. Again, a high degree of non-uniqueness of the problem precludes accurate extraction of both parameters from the data when noise is present, a situation that cannot be circumvented by increasing the bandwidth. It is pointed out that this is not because of a possible shortcoming of the inversion procedure employed but rather dictated by the physics of the problem.

The conclusion here is that for the fast formation one of the parameters v_s, v_p, or a can be determined from the flexural dispersion data considered. For the slow formation, only v_s can be inverted successfully due to a lack of sensitivity to the other parameters. Increasing the bandwidth does not add enough information to the data in order to overcome this problem. It primarily helps in the identification of the dispersion curve so that, e. g., outliers in the data can be removed prior to further

Noise [%]	Inverted v_s [m/s]	Error [%]	Iter.
0.0	2,087.3	2.7	5
0.5	2,091.8	2.9	5
1.0	2,094.3	3.1	5
1.5	2,094.9	3.1	5
2.0	2,093.4	3.0	5
2.5	2,089.9	2.9	5
3.0	2,084.3	2.6	4
3.5	2,076.8	2.2	4
4.0	2,067.3	1.7	4
4.5	2,055.5	0.6	4
5.0	2,042.5	0.5	4

Table 5.6: Effect of increasing noise level on the inversion for formation shear wave velocity with $-10\,\%$ error in formation compressional wave velocity (fast formation, flexural dispersion, $f_c = 6.5\,\text{kHz}$, 16 samples with 3 kHz bandwidth).

processing, and in providing a larger number of measured points so that noise averages out. The latter, however, could also be realized by stacking repeated narrow-band measurements at one frequency.

5.4.3 Multi-frequency and multi-mode data

Since we found that increasing the bandwidth about an intermediate frequency of the flexural dispersion does not add any significant independent information to the data (Section 5.4.2), we experimented with providing the inversion algorithm with narrow-band data collected at different frequencies and combining data belonging to different dispersion curves.

Multi-frequency data

Since the formation shear wave velocity constitutes the low-frequency asymptote of the flexural dispersion, it is obvious that by combining one point taken from that

section of the dispersion curve where the asymptote practically has been reached [e. g., at 2 kHz in Fig. 5-2(a)] and one point at an intermediate frequency (such as 6.5 kHz for the fast formation), a simultaneous inversion for v_s and one other parameter to which the second measurement is sensitive (a or v_p for the fast formation) would be possible. However, this scenario is somewhat trivial because obtaining the first point requires measuring the low-frequency part of the dispersion curve which, if acquired with success, would yield knowledge of v_s directly. Furthermore, it is pointed out that if a k_{zi} is close to ω_i/v_s the cost function in (5.4) exhibits, due to the non-removable branch point of the determinant D at ω/v_s in the complex k_z domain, an undesired kink with respect to the component of $\overline{x}$ representing the model shear wave velocity, which is close to the location of the pursued minimum and thus likely to interfere with the optimization. These considerations lead to the question of how far the first point can be moved up the dispersion curve (away from the knee towards higher frequencies, keeping the second measurement fixed) while the two data points can still be used to deduce v_s and a second parameter (a or v_p) simultaneously, without recreating the non-unique situation as in Section 5.4.2. The outcome of this numerical experiment is that typically the transition to an underdetermined problem is a sharp one, occurring almost immediately after the data point departs away from the asymptote.

Multi-mode data

Since typical logging tools have both monopole and dipole sources available, it is reasonable to combine flexural and Stoneley mode dispersion data and to investigate the possibility of simultaneous inversion for more than one parameter. The capability of processing such multi-mode data without any modifications is a major advantage of the inversion scheme introduced in Section 5.2.2, which is not based on dispersion curve fitting. For the borehole problem with proper modes, on input each data point (ω_i, k_{zi}) has to be characterized only with respect to the azimuthal mode order n so that the determinant can be evaluated accordingly; no further labeling of the data is

Iter.	Inverted v_s [m/s]	Inverted a [cm]
0	1,828.8000	9.144000
1	2,156.9832	11.342040
2	2,042.9865	10.389955
3	2,032.3390	10.172504
4	2,031.9958	10.160209
5	2,032.0002	10.160003
6	2,032.0000	10.160000

Table 5.7: Numerical values of the iterates shown in Fig. 5-11(a).

necessary.

As an example, consider the fast formation and simultaneous inversion for formation shear wave velocity v_s and borehole radius a. Combination of one point from the Stoneley mode at 5 kHz and one point from the flexural mode at 6 kHz leads to a minimum of the cost function that is much better defined than in the case of using flexural data only. However, when using the same data for the simultaneous inversion of v_s and formation compressional wave velocity v_p no improvement results and a long, shallow minimum of the cost function is encountered.

This and the application of the Gauss-Newton minimization approach are illustrated in Fig. 5-11. Starting from an initial guess with $-10\,\%$ error in both parameters [v_s and a in Fig. 5-11(a), and v_s and v_p in Fig. 5-11(b)] the straight lines drawn connect successive iterates. Shown also are contours of the RMS cost based on (5.4). At the points marked "x" the cost is zero; the contour lines are equidistant on linear scale. For reference, Table 5.7 and 5.8 give the numerical values of the inverted parameters at each iteration step, starting with the initial guesses. These data illustrate the rapid convergence of the Gauss-Newton method applied to our problem.

The dark strips surrounding $v_s = 1,677\,\mathrm{m/s}$ in Fig. 5-11(a) and 5-11(b) are explained as follows. The cost function exhibits a kink here due to a branch point when v_s approaches the largest phase velocity provided as input. This is the point of

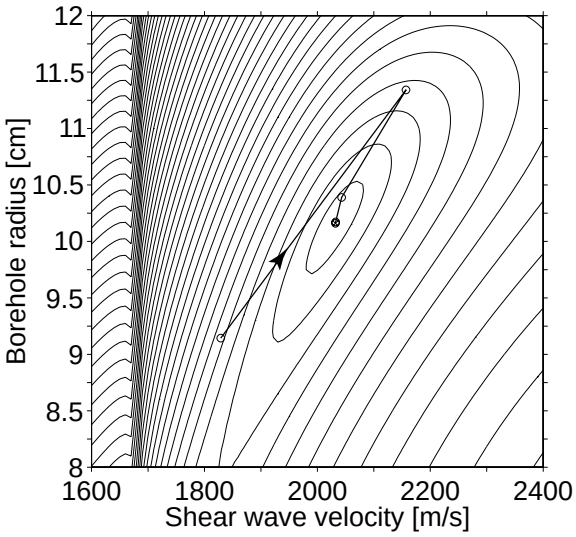

(a) Borehole radius.

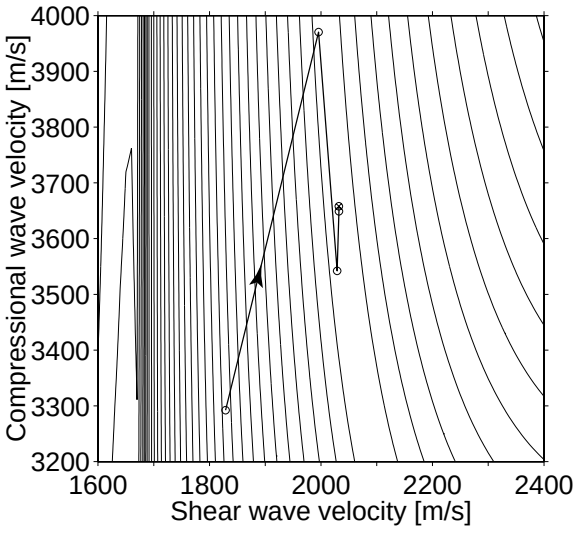

(b) Formation compressional wave velocity.

Figure 5-11: Examples of the Gauss-Newton search in the case of simultaneous inversion for formation shear wave velocity and borehole radius or formation compressional wave velocity (fast formation, Stoneley and flexural dispersion).

Iter.	Inverted v_s [m/s]	Inverted v_p [m/s]
0	1,828.8000	3,292.2000
1	1,995.6785	3,970.3752
2	2,028.9154	3,542.2408
3	2,032.1967	3,648.9515
4	2,031.9901	3,658.1178
5	2,032.0003	3,657.9982
6	2,031.9997	3,658.0026

Table 5.8: Numerical values of the iterates shown in Fig. 5-11(b).

the flexural dispersion at 6 kHz in Fig. 5-6 $[1/(1,677\,\mathrm{m/s}) = 596\,\mu\mathrm{s/m}]$. The special formulation of the determinant given in Section 5.3.1 takes care of keeping the value here finite (neither zero nor infinite). In the inversion, we have to make sure that the initial guess for v_s is to the right of the kink, knowing that the Stoneley and the flexural mode both are slower than the formation shear wave velocity v_s.

By providing several samples of the Stoneley and flexural dispersion curves from around 5 kHz and 6 kHz, respectively, and dividing M, the number of data points, unevenly between the two modes, it is possible to change their relative importance in the inversion and influence the shape of the minimum shown in Fig. 5-11(a). If the same number of data points is provided from both dispersion curves, however, the minimum is found to be similar to the case $M = 2$, once again showing the weak influence of data bandwidth on the information content of the data.

For the slow formation, we found that combining Stoneley and flexural dispersion data does not help in improving the conditioning of either of the two simultaneous inversion problems (e. g., when using two points located both at 2 kHz).

5.5 Borehole leaky-wave modes

Encouraged by the partial success of employing multi-mode information in the inversion for more than one parameter, we now focus our attention on the so-called leaky-wave modes.

In electromagnetics, there exists an extensive body of literature on the subject of leaky guided waves. The classical steepest-descent analysis implicating leaky-wave modes can be found in Collin's *Field Theory of Guided Waves* [184], originally published in 1960. The leaky-wave modes supported by open waveguides of various configurations have been studied extensively by A. A. Oliner and his collaborators; for an overview of papers starting in the early 1980s, refer to [185]. The observation that guided-wave modes associated with a layered background medium and not only its bulk wavenumbers give rise to branch points in the complex k_z domain and thus to various classes of leaky waves was made in [185, 186]. Recent efforts are, e. g., directed towards application of steepest-descent analysis to such more complicated structures [187, 188].

In what follows below, we explore the possibility of a systematic treatment of the leaky-wave domain in the area of acoustics. Leaky waves arising in borehole acoustics were discussed in [171]–[176], [189].

5.5.1 Classification of leaky-wave modes

Leaky-wave modes are unphysical or "improper" in the sense that they cannot exist as individual propagating waves. They exhibit an exponential radial growth while being attenuated longitudinally, not satisfying the radiation condition at infinity. Despite this they can contribute to the wave field in limited space regions and help in the understanding of how energy is radiated away from open waveguides. We turn to the question if the dispersions of these modes, for acoustic wave propagation in a borehole, can actually be measured later in this section.

Instead of concentrating on proper modes alone by requiring $k_{\alpha r}$ for $\alpha = s, p$ to be in the first quadrant of the complex plane including the positive imaginary axis, c. f., Section 5.3.1, we now specify $k_{\alpha r}$ analytically as

$$k_{\alpha r} = \mathrm{i}\, n_\alpha \sqrt{k_z^2 - k_\alpha^2} \tag{5.46}$$

where n_α can be 1 or -1 and the unique principal value of the square root is taken, i. e., that branch of the square root which maps the complex plane onto the right half-plane including the positive imaginary axis and zero, consistent with the standard numerical implementation of this function. Each specific choice of the n_s, n_p pair corresponds to locating k_z on one of four copies of the complex plane whose collection form what is known as Riemann surface, serving as the complex k_z domain. The four Riemann sheets are connected across hyperbolic Sommerfeld branch cuts [190, 191] emanating from the branch points $\pm k_\alpha$ and approaching $\pm\mathrm{i}\infty$. The choice of the Sommerfeld branch cuts is implicit in the definition (5.46) where the branch cut for the square root function is along the negative real axis. While from a mathematical point of view there is a high degree of arbitrariness in the introduction of branch cuts (if the main purpose is the construction of domains on which analyticity holds) the Sommerfeld branch cuts are of fundamental nature physically. This is because, for real, positive k_α (with each of the hyperbolas degenerated to an "L" on the real and imaginary axes) and $n_\alpha = 1$, (5.46) maps the first quadrant of the respective k_z sheet onto the second quadrant of the complex $k_{\alpha r}$ plane (with the $k_z > k_\alpha$ portion of the real axis mapped onto the positive imaginary axis corresponding to surface waves that propagate without attenuation in the axial direction); if $n_\alpha = -1$ the first quadrant is mapped onto the fourth quadrant corresponding to waves that propagate in the axial and radial directions while being attenuated in the axial direction and growing in the radial direction (leaky waves). This leads to a clear relation between the $k_{\alpha r}$ and k_z depending on which of the four Riemann sheets k_z is located, with

corresponding physical meaning.

We are thus led to a natural classification of the roots of (5.1) and the associated modes (again considering real, positive k_α for simplicity). Real roots $k_z > k_\alpha$ on the sheet with $n_s = n_p = 1$ (termed the top sheet) represent modes that are bound to the surface of the waveguide. They are thus classified in the present work as proper nm modes, where n, as before, is the azimuthal mode order and m a second index distinguishing the various modes encountered for a given n. Without proof we state here that no other than real roots with $|k_z| > k_\alpha$ are found on the top sheet (note that if k_z is a root then $-k_z$ is also a root). Roots in the first quadrant of the sheet with $n_s = -1$, $n_p = 1$ which we call the S sheet are associated with leaky modes that exhibit leakage in the shear component only and are labeled as S_{nm}. Accordingly, when $n_s = n_p = -1$, i. e., on the SP sheet, the roots correspond to leaky SP_{nm} modes with shear *and* compressional components that grow exponentially in the radial direction. Finally, the P sheet where $n_s = 1, n_p = -1$ is populated with leaky P_{nm} modes that have bound shear and leaky compressional components.

For example, in this classification scheme the modes corresponding to the Stoneley dispersions in Fig. 5-6 would be designated as proper 01 modes and the leaky Stoneley mode in Fig. 5-6(b) as S_{01}. The transition from S_{01} to proper 01 is an example of the migration of a zero of D from a bottom Riemann sheet to the top sheet as frequency increases.

5.5.2 Leaky-wave modal dispersions

For the parameters of the fast formation in Table 5.1 and for azimuthal mode order $n = 1$ (dipole modes) we computed a comprehensive classified set of modal dispersion curves (Fig. 5-12 and Fig. 5-13). All modes detected (by inspection of $|D|$, Section 5.2.1) and with an attenuation of less than 50 dB/m in the frequency range $f = 0 \ldots 15$ kHz were included. Phase slowness is defined as $\mathrm{Re}\{k_z\}/\omega$ and modal

attenuation as

$$\alpha_{\mathrm{dB}} = \frac{20\,\mathrm{m}}{\ln 10}\,\mathrm{Im}\{k_z\} \times 1\,\mathrm{dB/m} \tag{5.47}$$

The modes encountered on each of the four Riemann sheets were labeled with $m = 1, 2, \ldots$ according to phase slowness at the low-frequency end of the spectrum, starting with $m = 1$ for the slowest mode. Thus, the flexural dispersion in Fig. 5-2(a) is here referred to as belonging to the proper 11 mode [Fig. 5-12(a)]; since a lossless formation is considered, the proper modes have zero attenuation [Fig. 5-13(a)]. The various leaky modes exhibit a quite rich frequency dependency. It is observed that, as $\omega \to 0$, the phase slowness of the leaky waves considered here either approaches zero or goes to infinity [Fig. 5-12(b) to Fig. 5-12(d)], contrasting the behavior of the proper modes. At high frequencies, the slowness of the leaky S_{12} mode approaches $1/v_s$ while SP_{12} and P_{11} apparently go to $1/v_p$, a dependence that makes the latter two modes interesting candidates for inversion of v_p. Comparing Fig. 5-13(b) through Fig. 5-13(d), our interest in SP_{12} further increases since this mode exhibits a relatively low attenuation over a wide frequency band.

We conclude the qualitative description of the computed dipole dispersion curves with reporting an as yet unexplained "resonant" behavior of the SP_{12} mode at higher frequencies. The modal dispersion, plotted in Fig. 5-14 over an extended frequency range $f = 0 \ldots 35\,\mathrm{kHz}$, shows well-defined and roughly equally spaced maxima of attenuation at $f = 13.69, 21.88, 30.03\,\mathrm{kHz}$ with sections of decreasing attenuation and slightly increasing phase slowness in between. At the location of each of the attenuation maxima the phase slowness forms a kind of step with finite negative slope.

In principle, given its dispersion data, the leaky SP_{12} mode is found to be suited for helping in the simultaneous inversion of v_s and v_p in the fast formation. When examining the guidance mismatch as defined in (5.4) with $M = 2$, where one sample is taken from the proper 11 dispersion at 6 kHz and the other from the SP_{12} dispersion at 9 kHz, a well-defined minimum in the v_s-v_p plane is encountered, promising a robust

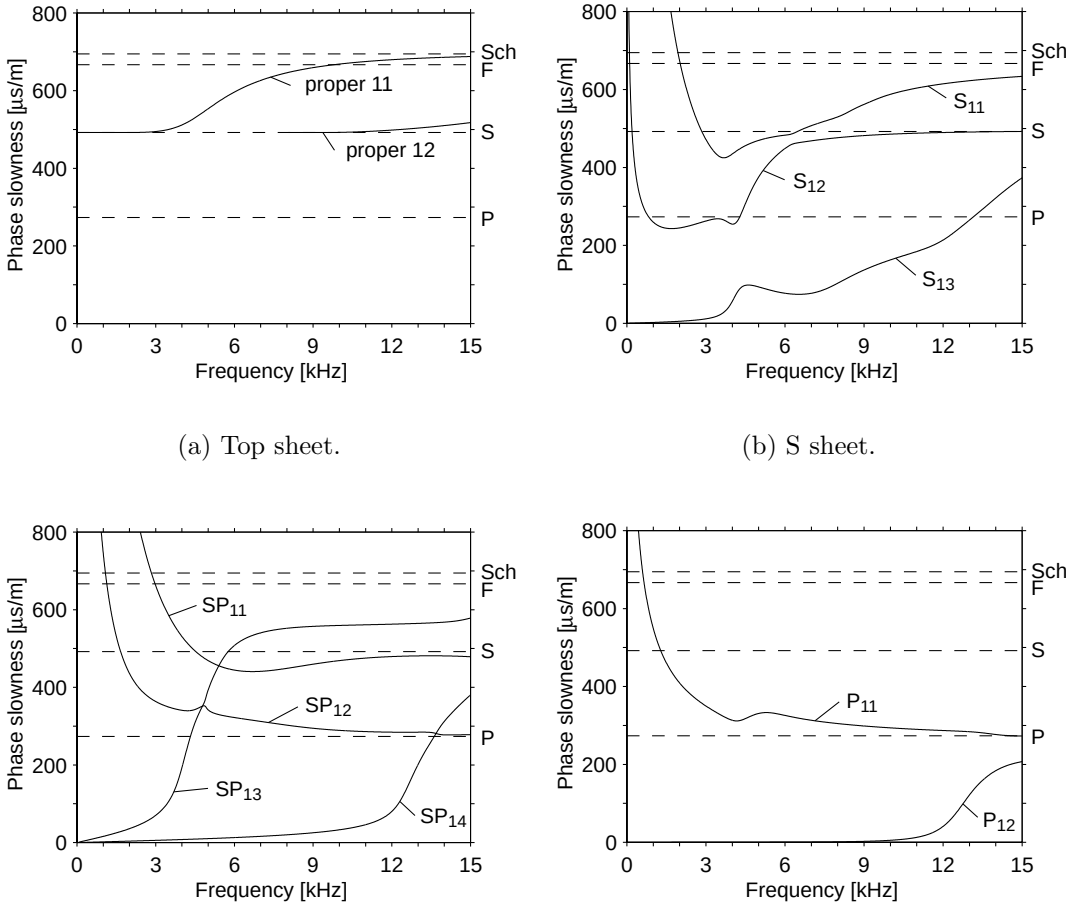

(a) Top sheet.

(b) S sheet.

(c) SP sheet.

(d) P sheet.

Figure 5-12: Comprehensive classified set of dipole modal dispersions: modal phase slowness (fast formation).

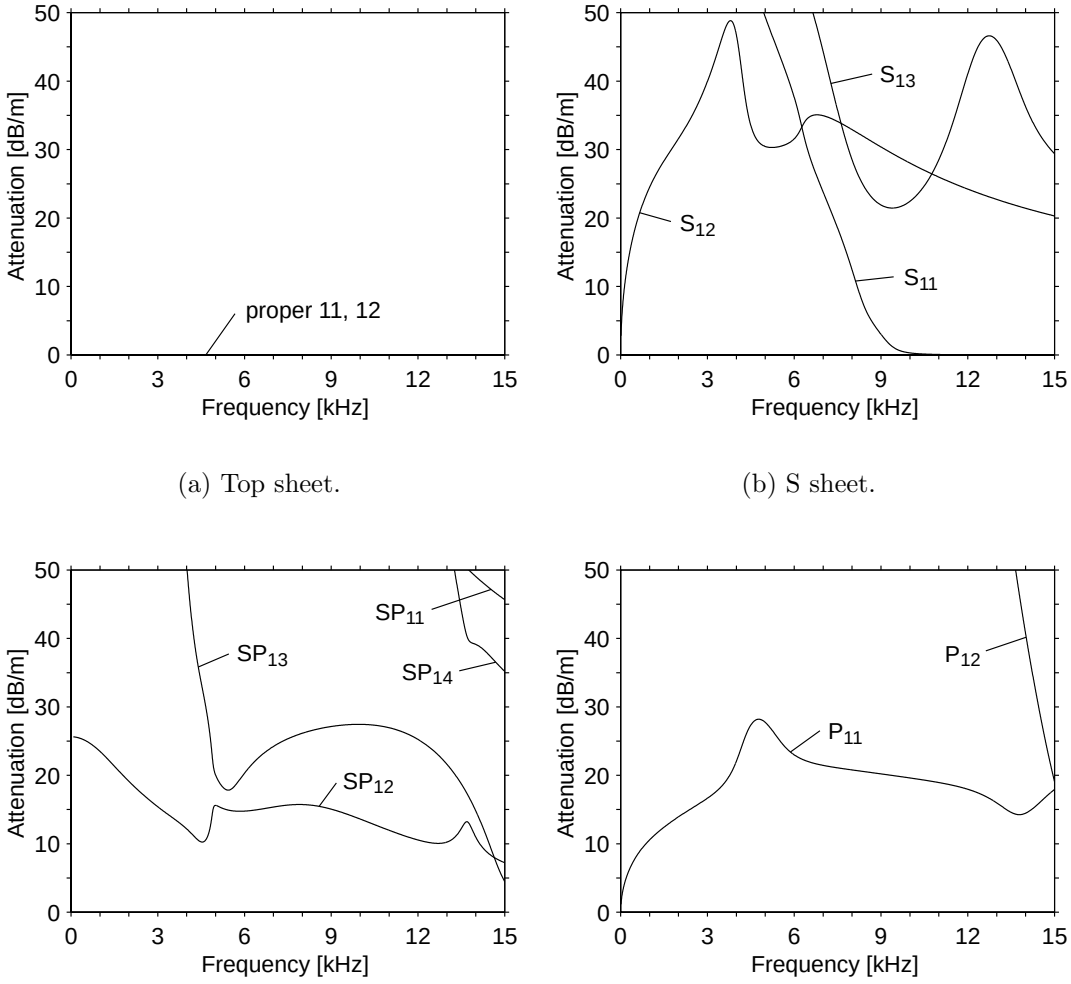

(a) Top sheet.

(b) S sheet.

(c) SP sheet.

(d) P sheet.

Figure 5-13: Comprehensive classified set of dipole modal dispersions: modal attenuation (fast formation).

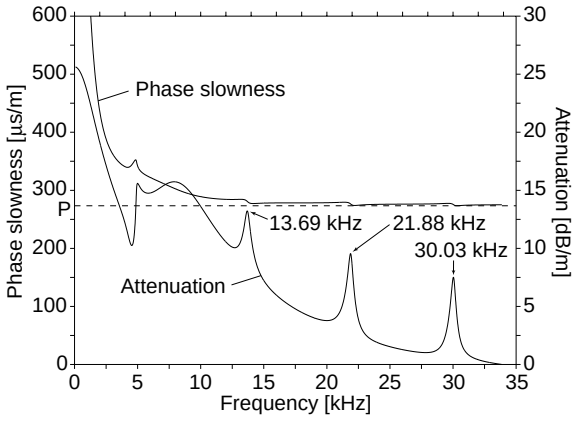

Figure 5-14: "Resonant" behavior of the leaky SP_{12} dispersion at higher frequencies (fast formation).

inversion of the two parameters in the presence of noise. The attenuation of the SP_{12} mode at the sampling frequency, read off from Fig. 5-13(c) as about 15 dB/m, is not exceedingly high.

5.5.3 Excitation of leaky-wave modes

Before conducting any further sensitivity experiments we should address the question which of all the leaky modes satisfying the boundary conditions at the surface of the open waveguide are actually excited with appreciable amplitude, so that their dispersions could possibly be obtained experimentally.

For this purpose we simulated the dipole excitation problem in the fast formation under consideration (Table 5.1) with a 3-D Green tensor code for cylindrically layered structures [192]. The dipole source was placed on the borehole axis, with the dipole axis in the radial direction. Sixteen receivers on the borehole axis with interspacing of 15.24 cm (6 in) were simulated to record the radial component (co-polarized with the dipole source) of the velocity waveforms in the time domain, in response to a transmitted pulse with a spectrum of Blackman-Harris type and center frequency 7.5 kHz. For the results discussed below, the receiver closest to the source had a

separation from the source equal to the receiver spacing. The time sampling step was $4\,\mu$s and the fast Fourier transform (FFT) employed of length 1024.

The simulated noise-free waveforms were then input to a modified matrix pencil algorithm [158] which returns estimated modal dispersion data (Fig. 5-15). It is important to note that this is a pure signal processing step the application of which requires no knowledge of the configuration of the waveguide and no information about the details of the source. The model order was set to $p = 6$, the tolerance for accepting forward-backward pole matches was $10\,\%$, and the FFT of length 2048. Discarding poles with a residue of less than $-30\,\mathrm{dB}$ as compared to the pole showing the strongest excitation over the whole frequency range, the remaining dispersion data are plotted in Fig. 5-15, marked with circles of 10 sizes each of which covers $3\,\mathrm{dB}$ of energy. We furthermore selected dispersion curves from Fig. 5-12 and Fig. 5-13 (obtained independently by mode tracking) and overlaid them with the discrete dispersion data as shown in Fig. 5-15.

The result is a quite convincing demonstration of the physical reality of leaky waves in general! In fact, here, with the receiver array not far from the source, they are seen to be the dominant contributors to the energy of the wavefield. We clearly identify the excitation of the SP_{13}, SP_{14}, and S_{13} leaky modes over certain sub-spectra (note the simultaneous match in phase slowness and attenuation). Above $4.5\,\mathrm{kHz}$ the chain of estimated dispersion data that up to this point matches closely the SP_{13} dispersion curve appears to divert in favor of the S_{12} dispersion, leading to a poorer match. This observation might reflect a non-uniqueness of the decomposition into leaky-wave modes. We also find the proper 11 mode (dominant for a greater distance from the source) and, much weaker, the proper 12 mode. The estimation of both proper modes suffers from a removable phase wrapping problem, seen in the phase slowness data [Fig. 5-15(a)] beginning at about $10\,\mathrm{kHz}$ and $13\,\mathrm{kHz}$, respectively; the estimated phase slownesses erroneously jump down to zero, an effect that does not concern us here. Finally, to a number of poles a phase slowness close to $1/v_s$ and

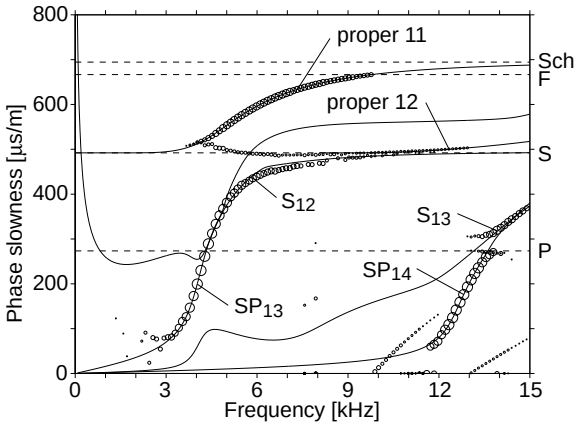

(a) Modal phase slowness.

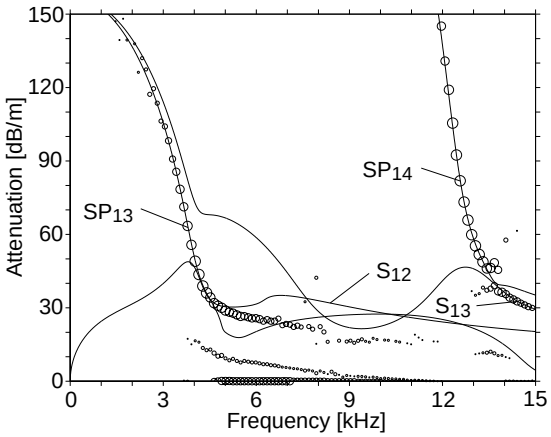

(b) Modal attenuation.

Figure 5-15: Dispersion data from processing simulated waveforms with a modified matrix pencil algorithm, matched with dispersion curves obtained by mode tracking (fast formation).

$1/v_p$ is assigned, commonly interpreted as indication of shear and compressional head waves. We are not discussing here the possibility of using the latter information for the deduction of v_s and v_p.

While all of the above is interesting, we find that the sought after SP_{12} mode is not encountered in the simulation results in Fig. 5-15. Testing the possibility of simultaneous inversion of v_s and v_p in a similar way as for SP_{12}, but now combining the point from the proper 11 dispersion at 6 kHz with a sample from the SP_{13} dispersion at 4 kHz, then with one from the S_{12} dispersion at 5.5 kHz, one from the SP_{14} dispersion at 13 kHz, and finally one from the S_{13} dispersion at 14.5 kHz, leads in the first two cases to a very poorly defined minimum and in the second two cases to a poorly defined minimum of the guidance mismatch in the v_s-v_p plane. Thus, the leaky-wave mode dispersion data extracted with help of the present signal processing methodology are not helpful in the simultaneous inversion of v_s and v_p.

While we cannot exclude the possibility that a different signal processing scheme would indicate the contribution of leaky modes not shown in Fig. 5-15, the question whether or not a particular mode is excited and thus physically significant will depend on the frequency-dependent location of the associated root in the k_z domain. For the electromagnetic open-waveguide problem, necessary conditions for the physical significance of leaky-wave modes have been established, namely the path consistency condition [193, 194] and the capturing of the roots by a steepest-descent path [187, 188]. Similar conditions may hold for acousto-elastic waves.

5.6 Conclusions

We have described a very efficient and versatile procedure for a parametric model-based inversion of guided-wave modal dispersions. The new method avoids the explicit computation or tabulation of dispersion curves and is applicable to multi-frequency and multi-mode data. Using a suitable formulation of the guidance condition, we

investigated the practically important case of sonic wave propagation along a fluid-filled borehole in a homogeneous, isotropic elastic rock formation, concentrating on the inversion for the formation shear and compressional wave velocities and the borehole radius. While the inversion principle proved to work well, in some cases physical limitations were encountered, caused by a lack of sensitivity of the data or non-uniqueness of the inverse problem. Some of the results are summarized qualitatively in the following paragraph.

For the fast formation considered, the individual flexural and Stoneley dispersions were found to be invertible robustly only for one of the three parameters. A simultaneous inversion for more than one parameter proved difficult due to the high degree of non-uniqueness encountered. For the slow formation considered, the data were shown to be relatively insensitive to the formation compressional wave velocity and the borehole radius. Collecting data over a wider frequency band (but away from the asymptotes) seemed not to improve this situation. Combining Stoneley and flexural dispersion data was found to be beneficial for the simultaneous inversion for formation shear wave velocity and borehole radius, but only in the case of the fast formation.

Inspired by similar efforts in the area of electromagnetics, we classified the borehole leaky-wave modes according to the location of the roots of the characteristic equation on the various Riemann sheets of the complex longitudinal wavenumber domain. This natural classification scheme can be generalized to multi-layer structures. A comprehensive set of dipole leaky-wave modal dispersions was computed for the fast formation, showing a rich variety of frequency dependencies. The mode termed SP_{12} was found to be suitable for the inversion for formation compressional wave velocity. In an independent numerical investigation (using a 3-D Green tensor code with subsequent dispersion data extraction) the excitation of several of the predicted leaky-wave modes was clearly demonstrated (with the receiver array close to the source point). None of the extracted modes, however, proved useful for the simultaneous inversion for the formation shear and compressional wave velocities. Despite this, we hope that

similar systematic investigations of the leaky-wave mode regime might contribute to a more detailed understanding of the sonic wave propagation along boreholes.

Chapter 6

Summary

The material in Chapter 2 discusses the construction of tapered waves for the numerical simulation of three-dimensional (3-D) rough surface scattering via the method of moments. The use of such waves enables truncating the computational model of the rough surface and avoids artificial edge diffraction due to an illumination with plane waves. We consider the class of incident fields that can be written as the most general superposition of a two-dimensional (2-D) spectrum of plane waves with arbitrary individual polarization, including propagating and evanescent waves. The amplitude spectrum is chosen to synthesize an arbitrary footprint of the tapered wave. The use of a simple Gaussian spectrum is recommended and avoids problems near the grazing incidence. A dominant polarization state of the tapered wave for all angles of incidence is achieved as prescribed, by choosing the polarization vector of each individual plane wave as the orthogonal projection of the polarization vector of the central plane wave onto the plane determined by the respective wavevector. The virtue of this procedure is the removal of an irregularity at the origin of the 2-D wavenumber space that follows from a conventional construction in which constant horizontal and vertical polarization components are used. This irregularity would lead to anomalies observed at and near the normal incidence. The resulting polarization vector as proposed is analytic throughout the domain of 2-D wavenumbers corresponding to

propagating waves. Furthermore, the above mentioned orthogonal projection leads to a certain least squared error property of the total Maxwellian field with respect to a field distribution that is ideal regarding tapering and polarization but that does not satisfy Maxwell's equations. An exhaustive numerical comparison of the behavior of the optimal tapered wave versus the tapered wave, that exhibits the mentioned irregular behavior at normal incidence, as a function of incidence angle and footprint size is carried out. Relations to other tapered waves are pointed out and issues in the application of the tapered wave concept to 3-D scattering are discussed. The formation of the beam of the tapered wave is illustrated and it is noted that the inclusion of evanescent waves enables clean footprints even at grazing incidence. However, at grazing incidence and when objects are present in the simulation, energy is directed toward the edges of the simulation domain, leading to secondary edge diffraction although a tapered incident wave is used, showing the aggravated challenge of the low grazing angle scattering problem. In a conceptually logic next step, the established regularity of the polarization vector is exploited in deriving a closed-form approximation of the tapered wave that can be evaluated without resorting to any numerical integration. The derivation is based on an asymptotic expansion of the superposition integral with the Gaussian amplitude spectrum for large footprint sizes. The result has an interesting algebraic structure consisting of three separate factors that represent a plane wave, an amplitude shape factor, and a variable polarization vector. The local character of the expansion forces the breakdown of this approximation near the grazing incidence, similar to the 2-D scalar Thorsos wave.

In Chapter 3, the focus is on low-frequency broadband electromagnetic induction involving highly but not perfectly conducting and permeable objects. In view of the large conductivity contrast encountered in practice, the development is carried out in the domain of magnetoquasistatics. This regime is characterized by magnetic diffusion inside the objects, governed by a Helmholtz equation with imaginary squared wavenumber, and rapidly decaying, quasistatic scattered or secondary fields in the

background medium, described by Laplace's equation. The problem of a conducting and permeable prolate spheroid under axial, time harmonic excitation is solved analytically in terms of an infinite matrix equation. To this end, the fields inside the spheroid are expanded in terms of angular and radial spheroidal wavefunctions of the first kind, and the fields outside the spheroid in terms of associated Legendre functions of the first and second kind. These expansions are based on the separability of the scalar Helmholtz and Laplace equation in prolate spheroidal coordinates. We then match the tangential electric and magnetic fields and expand the angular spheroidal wavefunctions in terms of associated Legendre functions of the first kind, thereby eliminating the angular variable from the problem but retaining the infinite series in the resulting linear equations for the unknown expansion coefficients. A consideration of the far scattered field using the asymptotic behavior of the associated Legendre function of the second kind leads to an expression of the magnetic dipole moment induced in the spheroid or, equivalently, the magnetic polarizability factor of the spheroid, in terms of the first of the exterior expansion coefficients and elementary functions. We then derive special cases of the theory, among them the high-frequency limit and the low-frequency limit including the additional limits of large elongation and large relative permeability. A reconsideration of the derivation of the high-frequency limit shows that a particular asymptotic formula might constitute a broadband, closed-form approximation for the magnetic polarizability, however, a negligence of the angular aspect of the problem leads to an inaccuracy at intermediate frequencies. This prompts the development of an analytical thin-skin approximation that takes the metric of the spheroidal coordinate system into account, leading to an infinite system of equations featuring associated Legendre functions of the second kind and integrated associated Legendre functions of the first kind, instead of radial spheroidal wavefunctions of the first kind and spheroidal expansion coefficients, that are difficult to compute in a stable manner at high frequencies. The resulting high-frequency approximation, seen to extend to lower frequencies when the relative

permeability is large, implies a significant reduction in mathematical complexity as compared to the exact solution. Approximate solutions for long spheroids and long circular cylinders are derived, given in terms of Bessel functions with complex argument and based on an exact functional, relating the induced magnetic dipole moment and the fields interior to the spheroid, and an infinite cylinder approximation. For numerical implementation, the infinite matrix equations are truncated and the radial spheroidal wavefunctions expanded in terms of spherical Bessel functions with complex argument and spheroidal expansion coefficients. Hodge's method is used to obtain the complex spheroidal eigenvalues. To bridge a sometimes remaining gap between low-frequency and high-frequency results, a broadband rational function approximation is developed and demonstrated. The magnetoquasistatic response of a collection of small conducting and permeable objects is investigated, using a Foldy-Lax-type multiple scattering formulation with the induced magnetic dipole moments as unknowns. A simulation and measurement results demonstrate the discriminating capability of broadband electromagnetic induction methods.

Chapter 4 concentrates on a particular class of linear inverse problems, motivated as follows. As fields and waves propagate into space, information on the spatial details of their originating sources is gradually lost. This is evident from the observed blurring of the field distribution in free space when propagating, e. g., from a plane to a parallel plane away from the sources. This free-space diffraction phenomenon, based on a formulation that employs the equivalence principle, corresponds to a straightforward outward analytical continuation of the data, which is a numerically stable operation. However, the inverse problem, i.e., the determination of the field distribution on a surface located between the surface where the data are given and the unknown sources, is unstable. The solution of this problem, where no *a priori* knowledge on the unblurred data is assumed, is of interest in, but not limited to, such diverse fields as magnetometry, gravimetry, diffraction tomography, and scanning near-field optical microscopy. In an abstraction from the physical applications that are described in the second half

of the chapter, we have considered a multi-dimensional deconvolution problem, where the kernel depends on a parameter. This scalar, non-negative parameter describes the degree of blurring of the unknown object function. Based on the sole assumption that the blurring is additive, i. e., that a certain degree of distortion can as well be obtained by repeated application of the convolution operator with appropriate fractional choice of the blurring parameter, it is shown that the frequency domain representation of the kernel must be of exponential form. Consequently, the blurring process suppresses high-frequency components exponentially and the deconvolution problem is ill-conditioned. The ill-posedness of this type of inverse problems is often addressed with the help of the popular Tikhonov regularization technique, where a weighted energy functional is added to a data mismatch cost functional to be minimized. For our case of a convolutional operator this leads to a linear, shift-invariant filter which can be implemented numerically in the spatial frequency domain, using the fast Fourier transform algorithm. A strategy for choosing the regularization parameter is discussed. However, the somewhat artificial character of the introduction of the regularization parameter in the Tikhonov method, calls for the development of an alternative approach. Inspired by the geometry of the underlying physical applications, a solution based on a local extrapolation scheme is developed. Here an outward continuation away from the sources (a stable operation) is performed first, followed by an inward extrapolation towards the sources along lines perpendicular to the data surfaces. From a detailed analysis of this process, it is concluded that there is an optimal choice of the extrapolation parameters for which the error in the reconstructed data is minimized. It is interesting to note that, although fundamentally different, the two solutions behave similarly at the two extreme ends of their respective parameter space; the methods become either unstable due to exponential amplification of noise or inaccurate due to loss of resolution. For the planar inverse diffraction problem it is shown that a separate treatment of propagating and evanescent waves allows the application of the local extrapolation scheme to data obeying the Helmholtz equation.

While numerical results for the planar Poisson kernel and its generalization to the dynamic case indicate no superior performance of the local extrapolation method as compared with the common Tikhonov regularization technique, its direct applicability to non-convolutional problems is of interest. Furthermore, the local extrapolation scheme including parameter choice strategies can be formulated entirely in the space domain. Its local character may prove useful, e.g., in the case of contamination of the data by localized noise.

The inversion of guided-wave dispersion data with the goal of inferring unknown waveguide constitutive and geometric parameters is the topic of Chapter 5. The forward problem of obtaining modal dispersion curves is considered first. The determinant of the system matrix of the homogeneous linear system of equations that follows from matching the appropriate boundary conditions is a function of in general complex axial wavenumber, angular frequency, and a waveguide parameter vector. The discrete zeros of this determinant or roots of the guidance condition correspond to different modes. The corresponding dispersion curves, giving the associated axial wavenumber as a function of frequency and obtained by a numerical mode tracking procedure, depend on the waveguide parameter vector. Thus, for the inverse problem, an estimate of the waveguide parameter vector from noisy samples of one or more dispersion curves can in principle be obtained with help of a curve fitting procedure. However, this scheme has several disadvantages, largely caused by the nesting of the iterations of mode tracking and nonlinear optimization. Therefore, an inversion methodology is proposed which eliminates the inner of the two iterations by formulating the cost function to be minimized directly in terms of the determinant of the boundary conditions, allowing a rapid, iteration-free evaluation of the cost function. As an example of a significant technological application with considerable commercial potential, the sonic guidance condition for a fluid-filled borehole is considered. In the formulation, care is exercised in avoiding parasitic zeros and infinite values that are likely to cause problems in numerical forward and inverse dispersion analyses. The

high-frequency limit, the guidance condition of the Scholte wave, is obtained as a check. For the examples of a fast and a slow rock formation, the inversion of formation shear wave velocity, a quantity of great practical interest, with an error of the assumed model in borehole radius and formation compressional wave velocity is investigated numerically. Results are given for both the flexural and the Stoneley mode (the lowest-order dipole and monopole modes, respectively), providing useful insights into the nonlinear dependence of inverted formation shear wave velocity on the model errors. The frequency-dependent sensitivities of inverted shear wave velocity to the model errors are also displayed. These sensitivities are not to be confused with the elements of the Jacobian in the Gauss-Newton method used to perform the inversion via nonlinear optimization. The simultaneous inversion of formation shear and compressional wave velocities from flexural dispersion data in the fast formation is studied next, varying the bandwidth of the provided data and the level of contaminating noise. It is found that the simultaneous inversion problem is difficult due to the intrinsic insensitivity of the data with respect to the formation compressional wave velocity. Increasing the bandwidth is beneficial, but less than desirable. The inversion for formation shear wave velocity only, is found to be robust in the presence of noise and little dependent on bandwidth. A numerical experiment using multi-frequency data for simultaneous inversion is described and evaluated. Combining data from different dispersions—in the example the flexural and Stoneley dispersions in the fast formation—enables the simultaneous inversion of formation shear wave velocity and borehole radius. The leaky borehole modes are subsequently considered and classified according to the location of the associated roots on a multi-sheeted Riemann surface. A comprehensive classified set of dipole modes in the fast formation is presented. Using a 3-D Green tensor code and a modified matrix pencil algorithm, the excitation of some of the leaky modes is demonstrated. The possibility of using these modes in an inversion is discussed.

Bibliography

[1] K. Pak, L. Tsang, C. H. Chan, and J. Johnson, "Backscattering enhancement of electromagnetic waves from two-dimensional perfectly conducting random rough surfaces based on Monte Carlo simulations," *J. Opt. Soc. Am. A*, vol. 12, pp. 2491–2499, Nov. 1995.

[2] J. T. Johnson, L. Tsang, R. T. Shin, K. Pak, C. H. Chan, A. Ishimaru, and Y. Kuga, "Backscattering enhancement of electromagnetic waves from two-dimensional perfectly conducting random rough surfaces: A comparison of Monte Carlo simulations with experimental data," *IEEE Trans. Antennas Propagat.*, vol. 44, pp. 748–756, May 1996.

[3] K. Pak, L. Tsang, and J. Johnson, "Numerical simulations and backscattering enhancement of electromagnetic waves from two-dimensional dielectric random rough surfaces with the sparse-matrix canonical grid method," *J. Opt. Soc. Am. A*, vol. 14, pp. 1515–1529, July 1997.

[4] G. Zhang and L. Tsang, "Angular correlation function and scattering coefficient of electromagnetic waves scattered by a buried object under a two-dimensional rough surface," *J. Opt. Soc. Am. A*, vol. 15, pp. 2995–3001, Dec. 1998.

[5] Q. Li, L. Tsang, K. S. Pak, and C. H. Chan, "Bistatic scattering and emissivities of random rough dielectric lossy surfaces with the physics-based two-grid method in conjunction with the sparse-matrix canonical grid method," *IEEE Trans. Antennas Propagat.*, vol. 48, pp. 1–11, Jan. 2000.

[6] J. T. Johnson, *Applications of Numerical Models for Rough Surface Scattering*,

Ph.D. thesis, Massachusetts Institute of Technology, 1996.

[7] R. L. Wagner, J. Song, and W. C. Chew, "Monte Carlo simulation of electromagnetic scattering from two-dimensional random rough surfaces," *IEEE Trans. Antennas Propagat.*, vol. 45, pp. 235–245, Feb. 1997.

[8] V. Jandhyala, E. Michielssen, B. Shanker, and W. C. Chew, "A combined steepest descent-fast multipole algorithm for the fast analysis of three-dimensional scattering by rough surfaces," *IEEE Trans. Geosci. Remote Sensing*, vol. 36, pp. 738–748, May 1998.

[9] V. Jandhyala, B. Shanker, E. Michielssen, and W. C. Chew, "Fast algorithm for the analysis of scattering by dielectric rough surfaces," *J. Opt. Soc. Am. A*, vol. 15, pp. 1877–1885, July 1998.

[10] J. T. Johnson, R. T. Shin, J. A. Kong, L. Tsang, and K. Pak, "A numerical study of ocean polarimetric thermal emission," *IEEE Trans. Geosci. Remote Sensing*, vol. 37, pp. 8–20, Jan. 1999.

[11] Y. Zhang, *Forward and Inverse Problems in Microwave Remote Sensing of Objects in Complex Media*, Ph.D. thesis, Massachusetts Institute of Technology, 1999.

[12] Y. Zhang, Y. E. Yang, H. Braunisch, and J. A. Kong, "Electromagnetic wave interaction of conducting object with rough surface by hybrid SPM/MoM technique: abstract," *J. Electromagnetic Waves and Applications*, vol. 13, no. 7, pp. 983–984, 1999.

[13] Y. Zhang, Y. E. Yang, H. Braunisch, and J. A. Kong, "Electromagnetic wave interaction of conducting object with rough surface by hybrid SPM/MoM technique," in *Progress in Electromagnetics Research (PIER)*, J. A. Kong, Ed., vol. 22, pp. 315–335. EMW Publishing, Cambridge, 1999.

[14] Y. Zhang, Y. E. Yang, H. Braunisch, and J. A. Kong, "Electromagnetic scattering from conducting objects above a randomly rough surface," in *USNC/URSI Nat. Radio Sci. Meeting: Program and Abstracts*, Boulder, Jan. 4–8, 1999, p.

316.

[15] Y. E. Yang, Y. Zhang, H. Braunisch, and J. A. Kong, "Electromagnetic wave scattering from conducting objects partially buried under a randomly rough surface," in *Proc. Progress in Electromagnetics Research Symp. (PIERS)*, Taipei, Mar. 22–26, 1999, vol. 1, p. 540.

[16] K. O'Neill, R. Lussky, Jr., and K. D. Paulsen, "Scattering from a metallic object embedded near the randomly rough surface of a lossy dielectric," *IEEE Trans. Geosci. Remote Sensing*, vol. 34, pp. 367–376, Mar. 1996.

[17] G. Zhang, L. Tsang, and Y. Kuga, "Studies of the angular correlation function of scattering by random rough surfaces with and without a buried object," *IEEE Trans. Geosci. Remote Sensing*, vol. 35, pp. 444–453, Mar. 1997.

[18] G. Zhang and L. Tsang, "Angular correlation function of wave scattering by a random rough surface and discrete scatterers and its application in the detection of a buried object," *Waves Random Media*, vol. 7, pp. 467–479, July 1997.

[19] A. Madrazo and M. Nieto-Vesperinas, "Scattering of light and other electromagnetic waves from a body buried beneath a highly rough random surface," *J. Opt. Soc. Am. A*, vol. 14, pp. 1859–1866, Aug. 1997.

[20] J. Ripoll, A. Madrazo, and M. Nieto-Vesperinas, "Scattering of electromagnetic waves from a body over a random rough surface," *Opt. Commun.*, vol. 142, pp. 173–178, Oct. 1997.

[21] A. Madrazo, J. R. Arias-González, and M. Nieto-Vesperinas, "Polarization effects in scattering of electromagnetic waves by an object beneath a random rough surface," *Opt. Commun.*, vol. 162, pp. 91–98, Apr. 1999.

[22] M. Rodríguez Pino, L. Landesa, J. L. Rodríguez, F. Obelleiro, and R. J. Burkholder, "The generalized forward-backward method for analyzing the scattering from targets on ocean-like rough surfaces," *IEEE Trans. Antennas Propagat.*, vol. 47, pp. 961–969, June 1999.

[23] J. R. Arias-González, M. Nieto-Vesperinas, and A. Madrazo, "Morphology-

dependent resonances in the scattering of electromagnetic waves from an object buried beneath a plane or a random rough surface," *J. Opt. Soc. Am. A*, vol. 16, pp. 2928–2934, Dec. 1999.

[24] H. Braunisch, Y. Zhang, C. O. Ao, S.-E. Shih, Y. E. Yang, K.-H. Ding, J. A. Kong, and L. Tsang, "Tapered wave with dominant polarization state for all angles of incidence," *IEEE Trans. Antennas Propagat.*, vol. 48, pp. 1086–1096, July 2000.

[25] H. Braunisch, Y. Zhang, C. O. Ao, S.-E. Shih, Y. E. Yang, K.-H. Ding, J. A. Kong, and L. Tsang, "Tapered wave with a least squared error property," in *Proc. IEEE Int. Geosci. Remote Sensing Symp. (IGARSS)*, Honolulu, July 24–28, 2000, vol. 7, pp. 3123–3125.

[26] H. Braunisch, Y. Zhang, C. O. Ao, S.-E. Shih, Y. E. Yang, K.-H. Ding, J. A. Kong, and L. Tsang, "A modified tapered wave for the simulation of rough surface scattering," in *Proc. Progress in Electromagnetics Research Symp. (PIERS)*, Cambridge, July 5–14, 2000, p. 835.

[27] L. Tsang, J. A. Kong, and R. T. Shin, *Theory of Microwave Remote Sensing*, Wiley, New York, 1985.

[28] J. A. Kong, *Electromagnetic Wave Theory*, EMW Publishing, Cambridge, 2000.

[29] J. T. Johnson, "Surface currents induced on a dielectric half-space by a Gaussian beam: An extended validation for point matching method of moment codes," *Radio Sci.*, vol. 32, pp. 923–934, May–June 1997.

[30] J. A. Ratcliffe, "Some aspects of diffraction theory and their application to the ionosphere," *Reports Progress Phys.*, vol. 19, pp. 188–267, 1956.

[31] J. W. Goodman, *Introduction to Fourier Optics*, McGraw-Hill, New York, 1968.

[32] L. Tsang, C. H. Chan, and K. Pak, "Monte Carlo simulation of a two-dimensional random rough surface using the sparse-matrix flat-surface iterative approach," *Electron. Lett.*, vol. 29, pp. 1153–1154, June 1993.

[33] L. Tsang, C. H. Chan, and K. Pak, "Backscattering enhancement of a two-dimensional random rough surface (three-dimensional scattering) based on Monte Carlo simulations," *J. Opt. Soc. Am. A*, vol. 11, pp. 711–715, Feb. 1994.

[34] E. I. Thorsos, "The validity of the Kirchhoff approximation for rough surface scattering using a Gaussian roughness spectrum," *J. Acoust. Soc. Am.*, vol. 83, pp. 78–92, Jan. 1988.

[35] E. I. Thorsos and D. R. Jackson, "Studies of scattering theory using numerical methods," *Waves Random Media*, vol. 1, pp. S165–S190, July 1991.

[36] L. Tsang, C. H. Chan, K. Pak, and H. Sangani, "Monte-Carlo simulations of large-scale problems of random rough surface scattering and applications to grazing incidence with the BMIA/canonical grid method," *IEEE Trans. Antennas Propagat.*, vol. 43, pp. 851–859, Aug. 1995.

[37] D. J. Donohue, H.-C. Ku, and D. R. Thompson, "Application of iterative moment-method solutions to ocean surface radar scattering," *IEEE Trans. Antennas Propagat.*, vol. 46, pp. 121–132, Jan. 1998.

[38] J. T. Johnson, "A numerical study of low-grazing-angle backscatter from ocean-like impedance surfaces with the canonical grid method," *IEEE Trans. Antennas Propagat.*, vol. 46, pp. 114–120, Jan. 1998.

[39] J. V. Toporkov, R. T. Marchand, and G. S. Brown, "On the discretization of the integral equation describing scattering by rough conducting surfaces," *IEEE Trans. Antennas Propagat.*, vol. 46, pp. 150–161, Jan. 1998.

[40] J. V. Toporkov, R. S. Awadallah, and G. S. Brown, "Issues related to the use of a Gaussian-like incident field for low-grazing-angle scattering," *J. Opt. Soc. Am. A*, vol. 16, pp. 176–187, Jan. 1999.

[41] R. T. Marchand and G. S. Brown, "On the use of finite surfaces in the numerical prediction of rough surface scattering," *IEEE Trans. Antennas Propagat.*, vol. 47, pp. 600–604, Apr. 1999.

[42] H. D. Ngo and C. L. Rino, "Application of beam simulation to scattering at low grazing angles: 1. Methodology and validation," *Radio Sci.*, vol. 29, pp. 1365–1379, Nov.–Dec. 1994.

[43] C. H. Chan, L. Tsang, and Q. Li, "Monte Carlo simulations of large-scale one-dimensional random rough-surface scattering at near-grazing incidence: Penetrable case," *IEEE Trans. Antennas Propagat.*, vol. 46, pp. 142–149, Jan. 1998.

[44] P. Tran and A. A. Maradudin, "The scattering of electromagnetic waves from a randomly rough 2D metallic surface," *Opt. Commun.*, vol. 110, pp. 269–273, Aug. 1994.

[45] A. W. Glisson, *On the Development of Numerical Techniques for Treating Arbitrarily-Shaped Surfaces*, Ph.D. thesis, University of Mississippi, 1978.

[46] S. M. Rao, *Electromagnetic Scattering and Radiation of Arbitrarily-Shaped Surfaces by Triangular Patch Modeling*, Ph.D. thesis, University of Mississippi, 1980.

[47] S. M. Rao, D. R. Wilton, and A. W. Glisson, "Electromagnetic scattering by surfaces of arbitrary shape," *IEEE Trans. Antennas Propagat.*, vol. AP-30, pp. 409–418, May 1982.

[48] N. Bleistein and R. A. Handelsman, *Asymptotic Expansions of Integrals*, Holt, Rinehart and Winston, New York, 1975.

[49] C. M. Bender and S. A. Orszag, *Advanced Mathematical Methods for Scientists and Engineers*, McGraw-Hill, New York, 1978.

[50] I. S. Gradshteyn, I. M. Ryzhik, and A. Jeffrey (Ed.), *Table of Integrals, Series, and Products*, Academic Press, Boston, 5th edition, 1994.

[51] C. E. Baum, Ed., *Detection and Identification of Visually Obscured Targets*, Taylor & Francis, Philadelphia, 1999.

[52] P. Gao, L. Collins, P. M. Garber, N. Geng, and L. Carin, "Classification of landmine-like metal targets using wideband electromagnetic induction," *IEEE*

Trans. Geosci. Remote Sensing, vol. 38, pp. 1352–1361, May 2000.

[53] I. J. Won, D. A. Keiswetter, D. R. Hanson, E. Novikova, and T. M. Hall, "GEM-3: A monostatic broadband electromagnetic induction sensor," *J. Env. Eng. Geophys.*, vol. 2, pp. 53–64, Mar. 1997.

[54] C. C. Chen and L. Peters, Jr., "Buried unexploded ordnance identification via complex natural resonances," *IEEE Trans. Antennas Propagat.*, vol. 45, pp. 1645–1654, Nov. 1997.

[55] H. A. Haus and J. R. Melcher, *Electromagnetic Fields and Energy*, Prentice Hall, Englewood Cliffs, 1989.

[56] N. Geng, C. E. Baum, and L. Carin, "On the low-frequency natural response of conducting and permeable targets," *IEEE Trans. Geosci. Remote Sensing*, vol. 37, pp. 347–359, Jan. 1999.

[57] K. Sun, K. O'Neill, S. A. Haider, and K. D. Paulsen, "Numerical modeling of scattering from targets with small but non-negligible skin depths," in *Proc. IEEE Int. Geosci. Remote Sensing Symp. (IGARSS)*, Honolulu, July 24–28, 2000, vol. 4, pp. 1411–1414.

[58] F. Shubitidze, K. O'Neill, S. A. Haider, K. Sun, and K. D. Paulsen, "Analysis of induction responses from metal objects using the method of auxiliary sources," in *Proc. 8th Int. Conf. Mathematical Methods in Electromagnetic Theory (MMET)*, Kharkov, Sep. 12–15, 2000, pp. 468–470.

[59] J. R. Wait, "A conducting sphere in a time varying magnetic field," *Geophysics*, vol. 16, pp. 666–672, 1951.

[60] J. R. Wait, "A conducting permeable sphere in the presence of a coil carrying an oscillating current," *Can. J. Phys.*, vol. 31, pp. 670–678, 1953.

[61] J. Van Bladel, *Electromagnetic Fields*, McGraw-Hill, New York, 1964.

[62] M. N. Nabighian and J. D. Corbett, Eds., *Electromagnetic Methods in Applied Geophysics, Vol. 1: Theory*, Society of Exploration Geophysicists, Tulsa, 1987.

[63] A. A. Kaufman, *Geophysical Field Theory and Method, Part C: Electromagnetic*

Fields II, Academic Press, San Diego, 1994.

[64] A. A. Kaufman and G. V. Keller, *Inductive Mining Prospecting, Part I: Theory*, Elsevier, Amsterdam, 1985.

[65] V. F. Aleksin, V. P. Demutskii, and S. S. Romanov, "Diffusion of a quasistatic electromagnetic field into spheroids," *Sov. Phys. Tech. Phys.*, vol. 25, pp. 548–551, May 1980.

[66] C. O. Ao, H. Braunisch, K. O'Neill, and J. A. Kong, "Quasi-magnetostatic solution for a conducting and permeable spheroid," in *Proc. IEEE Int. Geosci. Remote Sensing Symp. (IGARSS)*, Honolulu, July 24–28, 2000, vol. 4, pp. 1418–1420.

[67] C. O. Ao, H. Braunisch, K. O'Neill, and J. A. Kong, "Quasi-magnetostatic solution for a conducting and permeable spheroid," in *Proc. Progress in Electromagnetics Research Symp. (PIERS)*, Cambridge, July 5–14, 2000, p. 452.

[68] T. Oguchi, "Scattering properties of oblate raindrops and cross polarization of radio waves due to rain: calculations at 19.3 and 34.8 GHz," *J. Radio Res. Lab.*, vol. 20, no. 102, pp. 79–118, 1973.

[69] S. Asano and G. Yamamoto, "Light scattering by a spheroidal particle," *Appl. Opt.*, vol. 14, pp. 29–49, Jan. 1975.

[70] V. G. Farafonov, "Diffraction of a plane electromagnetic wave at a dielectric spheroid," *Diff. Equ.*, vol. 19, pp. 1319–1329, Oct. 1983.

[71] M. F. R. Cooray and I. R. Ciric, "Scattering of electromagnetic waves by a system of two dielectric spheroids of arbitrary orientation," *IEEE Trans. Antennas Propagat.*, vol. 39, pp. 680–684, May 1991.

[72] M. F. R. Cooray and I. R. Ciric, "Scattering by systems of spheroids in arbitrary configurations," *Computer Phys. Comm.*, vol. 68, pp. 279–305, 1991.

[73] N. V. Voshchinnikov and V. G. Farafonov, "Optical properties of spheroidal particles," *Astrophys. Space Sci.*, vol. 204, pp. 19–86, June 1993.

[74] S. Nag and B. P. Sinha, "Electromagnetic plane wave scattering by a system of

two uniformly lossy dielectric prolate spheroids in arbitrary orientation," *IEEE Trans. Antennas Propagat.*, vol. 43, pp. 322–327, Mar. 1995.

[75] N. V. Voshchinnikov, "Electromagnetic scattering by homogeneous and coated spheroids: calculations using the separation of variables method," *J. Quant. Spectrosc. Radiat. Transfer*, vol. 55, pp. 627–636, May 1996.

[76] I. R. Ciric and F. R. Cooray, "Separation of variables for electromagnetic scattering by spheroidal particles," in *Light Scattering by Nonspherical Particles: Theory, Measurements, and Applications*, M. I. Mishchenko, J. W. Hovenier, and L. D. Travis, Eds., pp. 89–130. Academic Press, San Diego, 2000.

[77] S. Zhang and J. Jin, *Computation of Special Functions*, Wiley, New York, 1996.

[78] W. J. Thompson, *Atlas for Computing Mathematical Functions: an Illustrated Guide for Practitioners, with Programs in Fortran 90 and Mathematica*, Wiley, New York, 1997.

[79] W. J. Thompson, *Atlas for Computing Mathematical Functions: an Illustrated Guide for Practitioners, with Programs in C and Mathematica*, Wiley, New York, 1997.

[80] H. Braunisch, C. O. Ao, K. O'Neill, and J. A. Kong, "Magnetoquasistatic response of a distribution of small conducting and permeable objects," in *Proc. IEEE Int. Geosci. Remote Sensing Symp. (IGARSS)*, Honolulu, July 24–28, 2000, vol. 4, pp. 1424–1426.

[81] C. Flammer, *Spheroidal Wave Functions*, Stanford University Press, Stanford, 1957.

[82] J. R. Wait, *Geo-Electromagnetism*, Academic Press, New York, 1982.

[83] M. Abramowitz and I. A. Stegun, Eds., *Handbook of Mathematical Functions with Formulas, Graphs, and Mathematical Tables*, National Bureau of Standards, Washington, 1964.

[84] D. J. Jackson, *Classical Electrodynamics*, Wiley, New York, 3rd edition, 1999.

[85] A. A. Kaufman, *Geophysical Field Theory and Method, Part A: Gravitational,*

Electric, and Magnetic Fields, Academic Press, San Diego, 1992.

[86] D. Slepian, "Some asymptotic expansions for prolate spheroidal wave functions," *J. Math. and Phys.*, vol. 44, pp. 99–140, 1965.

[87] W. Streifer, "Uniform asymptotic expansions for prolate spheroidal wave functions," *J. Math. and Phys.*, vol. 47, pp. 407–415, 1968.

[88] J. des Cloizeaux and M. L. Mehta, "Some asymptotic expressions for prolate spheroidal functions and for the eigenvalues of differential and integral equations of which they are solutions," *J. Math. Phys.*, vol. 13, pp. 1745–1754, Nov. 1972.

[89] J. W. Miles, "Asymptotic approximations for prolate spheroidal wave functions," *Stud. Appl. Math.*, vol. 54, pp. 315–349, Dec. 1975.

[90] L. Jen and C.-S. Hu, "Spheroidal wave functions of large frequency parameters $c = kf$ and the radiation fields of a metallic prolate spheroid excited by any circumferential slot," *IEEE Trans. Antennas Propagat.*, vol. AP-31, pp. 382–389, Mar. 1983.

[91] C.-S. Hu, "Prolate spheroidal wave functions of large frequency parameters $c = kf$ and their applications in electromagnetic theory," *IEEE Trans. Antennas Propagat.*, vol. AP-34, pp. 114–119, Jan. 1986.

[92] T. M. Dunster, "Uniform asymptotic expansions for prolate spheroidal functions with large parameters," *SIAM J. Math. Anal.*, vol. 17, pp. 1495–1524, Nov. 1986.

[93] S. S. Seker and A. Schneider, "Electromagnetic scattering from a dielectric cylinder of finite length," *IEEE Trans. Antennas Propagat.*, vol. 36, pp. 303–307, Feb. 1988.

[94] M. A. Karam, A. K. Fung, and Y. M. M. Antar, "Electromagnetic wave scattering from some vegetation samples," *IEEE Trans. Geosci. Remote Sensing*, vol. 26, pp. 799–808, Nov. 1988.

[95] L. Tsang, C. H. Chan, J. A. Kong, and J. Joseph, "Polarimetric signatures of a canopy of dielectric cylinders based on first and second order vector radiative

transfer theory," *J. Electromagnetic Waves and Applications*, vol. 6, no. 1, pp. 19–51, 1992.

[96] L. Tsang, K.-H. Ding, G. Zhang, C. C. Hsu, and J. A. Kong, "Backscattering enhancement and clustering effects of randomly distributed dielectric cylinders overlying a dielectric half space based on Monte-Carlo simulations," *IEEE Trans. Antennas Propagat.*, vol. 43, pp. 488–499, May 1995.

[97] Y.-C. Lin and K. Sarabandi, "Electromagnetic scattering model for a tree trunk above a tilted ground plane," *IEEE Trans. Geosci. Remote Sensing*, vol. 33, pp. 1063–1070, July 1995.

[98] Y.-C. Lin and K. Sarabandi, "A Monte Carlo coherent scattering model for forest canopies using fractal-generated trees," *IEEE Trans. Geosci. Remote Sensing*, vol. 37, pp. 440–451, Jan. 1999.

[99] J. M. López-Sánchez, H. Esteban-González, M. Baquero-Escudero, and J. Fortuny-Guasch, "An electromagnetic scattering model for multiple tree trunks above a tilted rough ground plane," *IEEE Trans. Geosci. Remote Sensing*, vol. 37, pp. 659–667, Mar. 1999.

[100] X. Wang, X. Luo, Z. Zhang, and J. Fu, "The study of an electromagnetic scattering model for two adjacent trunks above a rough surface ground plane," *Microwave Opt. Technol. Lett.*, vol. 20, pp. 369–376, Mar. 1999.

[101] T. Chiu and K. Sarabandi, "Electromagnetic scattering interaction between a dielectric cylinder and a slightly rough surface," *IEEE Trans. Antennas Propagat.*, vol. 47, pp. 902–913, May 1999.

[102] L. Tsang, J. A. Kong, and K.-H. Ding, *Scattering of Electromagnetic Waves, Vol. I: Theories and Applications*, Wiley, New York, 2000.

[103] E. Anderson, Z. Bai, C. Bischof, S. Blackford, J. Demmel, J. Dongarra, J. Du Croz, A. Greenbaum, S. Hammarling, A. McKenney, and D. Sorensen, *LAPACK Users' Guide*, Society for Industrial and Applied Mathematics, Philadelphia, 3rd edition, 1999.

[104] W. H. Press, S. A. Teukolsky, W. T. Vetterling, and B. P. Flannery, *Numerical Recipes in Fortran 77: the Art of Scientific Computing*, Cambridge University Press, Cambridge, 2nd edition, 1992.

[105] K. W. Fong, T. H. Jefferson, T. Suyehiro, and L. Walton, *Guide to the SLATEC Common Mathematical Library*, Lawrence Livermore and Sandia National Laboratories, Livermore and Albuquerque, 1993.

[106] D. B. Hodge, "Eigenvalues and eigenfunctions of the spheroidal wave equation," *J. Math. Phys.*, vol. 11, pp. 2308–2312, Aug. 1970.

[107] L.-W. Li, M.-S. Leong, T.-S. Yeo, P.-S. Kooi, and K.-Y. Tan, "Computations of spheroidal harmonics with complex arguments: a review with an algorithm," *Phys. Rev. E*, vol. 58, pp. 6792–6806, Nov. 1998.

[108] H. A. Eide, J. J. Stamnes, K. Stamnes, and F. M. Schulz, "New method for computing expansion coefficients for spheroidal functions," *J. Quant. Spectrosc. Radiat. Transfer*, vol. 63, pp. 191–203, Sep. 1999.

[109] T. Oguchi, "Eigenvalues of spheroidal wave functions and their branch points for complex values of propagation constants," *Radio Sci.*, vol. 5, pp. 1207–1214, Aug.–Sep. 1970.

[110] T. V. Nguyen, "Recursive convolution and discrete time domain simulation of lossy coupled transmission lines," *IEEE Trans. Computer-Aided Design*, vol. 13, pp. 1301–1305, Oct. 1994.

[111] H. Braunisch and H. Grabinski, "Time-domain simulation of large lossy interconnect systems on conducting substrates," *IEEE Trans. Circuits Syst. I*, vol. 45, pp. 909–918, Sep. 1998.

[112] P. E. Gill, W. Murray, and M. H. Wright, *Practical Optimization*, Academic Press, New York, 1981.

[113] J. Meixner and F. W. Schäfke, *Mathieusche Funktionen und Sphäroidfunktionen mit Anwendungen auf physikalische und technische Probleme*, Springer-Verlag, Göttingen, 1954.

[114] H. Braunisch and T. M. Habashy, "Deblurring by a local extrapolation scheme," *Inverse Problems*, vol. 15, pp. 1263–1281, Oct. 1999.

[115] H. Braunisch and T. M. Habashy, "An alternative to Tikhonov regularization for deblurring and inverse diffraction," in *Proc. Progress in Electromagnetics Research Symp. (PIERS)*, Cambridge, July 5–14, 2000, p. 546.

[116] A. N. Tikhonov, "Solution of incorrectly formulated problems and the regularization method," *Sov. Math. Doklady*, vol. 4, pp. 1035–1038, 1963.

[117] A. N. Tikhonov, "Regularization of incorrectly posed problems," *Sov. Math. Doklady*, vol. 4, pp. 1624–1627, 1963.

[118] A. N. Tikhonov and V. Y. Arsenin, *Solutions of Ill-Posed Problems*, Winston, New York, 1977.

[119] C. W. Groetsch, *The Theory of Tikhonov Regularization for Fredholm Equations of the First Kind*, Pitman, Boston, 1984.

[120] V. A. Morozov, "On the solution of functional equations by the method of regularization," *Sov. Math. Doklady*, vol. 7, pp. 414–417, 1966.

[121] V. A. Morozov, *Methods for Solving Incorrectly Posed Problems*, Springer-Verlag, New York, 1984.

[122] V. A. Morozov, *Regularization Methods for Ill-Posed Problems*, Chemical Rubber Company Press, Boca Raton, 1993.

[123] D. L. Donoho, "De-noising by soft-thresholding," *IEEE Trans. Inform. Theory*, vol. 41, pp. 613–627, May 1995.

[124] K. Kunisch and J. Zou, "Iterative choices of regularization parameters in linear inverse problems," *Inverse Problems*, vol. 14, pp. 1247–1264, 1998.

[125] G. Wahba, "Practical approximate solutions to linear operator equations when the data are noisy," *SIAM J. Math. Anal.*, vol. 14, pp. 651–667, 1977.

[126] P. Craven and G. Wahba, "Smoothing noisy data with spline functions: Estimating the correct degree of smoothing by the method of generalized cross-validation," *Numer. Math.*, vol. 31, pp. 377–403, 1979.

[127] G. Wahba, *Spline Models for Observational Data*, Society for Industrial and Applied Mathematics, Philadelphia, 1990.

[128] M. A. Lukas, "Comparisons of parameter choice methods for regularization with discrete noisy data," *Inverse Problems*, vol. 14, pp. 161–184, 1998.

[129] Q.-N. Jin, "A convergence analysis for Tikhonov regularization of nonlinear ill-posed problems," *Inverse Problems*, vol. 15, pp. 1087–1098, 1999.

[130] D. Calvetti, S. Morigi, L. Reichel, and F. Sgallari, "Tikhonov regularization and the L-curve for large discrete ill-posed problems," *J. Comput. Appl. Math.*, vol. 123, pp. 423–446, 2000.

[131] A. Abubakar, *Three-Dimensional Nonlinear Inversion of Electrical Conductivity*, Ph.D. thesis, Delft University of Technology, 2000.

[132] A. Cuyt and L. Wuytack, *Nonlinear Methods in Numerical Analysis*, North-Holland, New York, 1987.

[133] F. S. Grant and G. F. West, *Interpretation Theory in Applied Geophysics*, McGraw-Hill, New York, 1965.

[134] O. D. Kellogg, *Foundations of Potential Theory*, Dover, New York, 1953.

[135] W. A. Heiskanen and H. Moritz, *Physical Geodesy*, Freeman, San Francisco, 1967.

[136] H. Moritz, *Advanced Physical Geodesy*, Wichmann, Karlsruhe, 1980.

[137] W. Torge, *Gravimetry*, de Gruyter, Berlin, 1989.

[138] V. Dimri, *Deconvolution and Inverse Theory: Application to Geophysical Problems*, Elsevier, Amsterdam, 1992.

[139] R. J. Blakely, *Potential Theory in Gravity and Magnetic Applications*, Cambridge University Press, Cambridge, 1995.

[140] S. P. Huestis and R. L. Parker, "Upward and downward continuation as inverse problems," *Geophys. J. R. Astr. Soc.*, vol. 57, pp. 171–188, Apr. 1979.

[141] W. Keller and M. Hirsch, "A boundary value approach to downward continuation," *Manuscripta Geodaetica*, vol. 19, no. 2, pp. 101–118, 1994.

[142] M. A. Zumberge, J. R. Ridgway, and J. A. Hildebrand, "A towed marine gravity meter for near-bottom surveys," *Geophysics*, vol. 62, pp. 1386–1393, Sep.–Oct. 1997.

[143] R. L. Parker, *Geophysical Inverse Theory*, Princeton University Press, Princeton, 1994.

[144] R. G. Henderson, "A comprehensive system of automatic computation in magnetic and gravity interpretation," *Geophysics*, vol. 25, pp. 569–585, June 1960.

[145] T. Bláha, M. Hirsch, W. Keller, and M. Scheinert, "Application of a spherical FFT approach in airborne gravimetry," *J. Geod.*, vol. 70, pp. 663–672, Sep. 1996.

[146] A. Sommerfeld, *Optics*, Academic Press, New York, 1954.

[147] J. R. Shewell and E. Wolf, "Inverse diffraction and a new reciprocity theorem," *J. Opt. Soc. Am.*, vol. 58, pp. 1596–1603, Dec. 1968.

[148] H. P. Baltes, Ed., *Inverse Source Problems in Optics*, Springer-Verlag, Berlin, 1978.

[149] M. Bertero, C. De Mol, F. Gori, and L. Ronchi, "Number of degrees of freedom in inverse diffraction," *Optica Acta*, vol. 30, pp. 1051–1065, Aug. 1983.

[150] A. P. Anderson and M. F. Adams, "Holographic and tomographic imaging with microwaves and ultrasound," in *Inverse Methods in Electromagnetic Imaging, Part 2*, W.-M. Boerner, H. Brand, L. A. Cram, D. T. Gjessing, A. K. Jordan, W. Keydel, G. Schwierz, and M. Vogel, Eds., pp. 1077–1105. Reidel, Dordrecht, 1985.

[151] M. Bertero, P. Boccacci, and M. Piana, "Resolution and super-resolution in inverse diffraction," in *Inverse Problems of Wave Propagation and Diffraction*, G. Chavent and P. C. Sabatier, Eds., pp. 1–17. Springer-Verlag, Berlin, 1997.

[152] M. Bertero and C. De Mol, "Stability problems in inverse diffraction," *IEEE Trans. Antennas Propagat.*, vol. AP-29, pp. 368–372, Mar. 1981.

[153] E. Wolf, "Three-dimensional structure determination of semi-transparent ob-

jects from holographic data," *Opt. Commun.*, vol. 1, pp. 153–156, 1974.

[154] D. W. Pohl and D. Courjon, Eds., *Near Field Optics*, Kluwer, Dordrecht, 1993.

[155] P. Blattner, H. P. Herzig, and R. Dändliker, "Scanning near-field optical microscopy: Transfer function and resolution limit," *Opt. Commun.*, vol. 155, pp. 245–250, Oct. 1998.

[156] B. G. Levi, "Progress made in near-field imaging with light from a sharp tip," *Phys. Today*, vol. 52, pp. 18–20, July 1999.

[157] S. W. Lang, A. L. Kurkjian, J. H. McClellan, C. F. Morris, and T. W. Parks, "Estimating slowness dispersion from arrays of sonic logging waveforms," *Geophysics*, vol. 52, pp. 530–544, Apr. 1987.

[158] M. P. Ekstrom, "Dispersion estimation from borehole acoustic arrays using a modified matrix pencil algorithm," in *Conf. Record of the 29th Asilomar Conf. on Signals, Systems, and Computers*, Pacific Grove, Oct. 31, 1995, vol. 1, pp. 449–453, IEEE Comp. Soc. Press, Los Alamitos, 1996.

[159] J. L. Stevens and S. M. Day, "Shear velocity logging in slow formations using the Stoneley wave," *Geophysics*, vol. 51, pp. 137–147, Jan. 1986.

[160] B. K. Sinha, "Sensitivity and inversion of borehole flexural dispersions for formation parameters," *Geophys. J. Int.*, vol. 128, pp. 84–96, Jan. 1997.

[161] C. H. Cheng, M. N. Toksöz, and M. E. Willis, "Determination of in situ attenuation from full waveform acoustic logs," *J. Geophys. Res.*, vol. 87, pp. 5477–5484, July 1982.

[162] K. J. Ellefsen, C. H. Cheng, and M. N. Toksöz, "Applications of perturbation theory to acoustic logging," *J. Geophys. Res.*, vol. 96, pp. 537–549, Jan. 1991.

[163] B. K. Sinha and S. Kostek, "Stress-induced azimuthal anisotropy in borehole flexural waves," *Geophysics*, vol. 61, pp. 1899–1907, Nov.–Dec. 1996.

[164] B. K. Sinha and K. W. Winkler, "Formation nonlinear constants from sonic measurements at two borehole pressures," *Geophysics*, vol. 64, pp. 1890–1900, Nov.–Dec. 1999.

[165] B. K. Sinha, M. R. Kane, and B. Frignet, "Dipole dispersion crossover and sonic logs in a limestone reservoir," *Geophysics*, vol. 65, pp. 390–407, Mar.–Apr. 2000.

[166] C. V. Kimball, "Shear slowness measurement by dispersive processing of the borehole flexural mode," *Geophysics*, vol. 63, pp. 337–344, Mar.–Apr. 1998.

[167] C. V. Kimball and D. J. Scheibner, "Error bars for sonic slowness measurements," *Geophysics*, vol. 63, pp. 345–353, Mar.–Apr. 1998.

[168] H. Braunisch, T. M. Habashy, B. K. Sinha, and J. Pabon, "Inversion of borehole dispersions for formation elastic moduli," in *Proc. IEEE Int. Ultrasonics Symp.*, San Juan, Oct. 22–25, 2000, 6 pages, in print.

[169] G. W. Hanson and A. B. Yakovlev, "An analysis of leaky-wave dispersion phenomena in the vicinity of cutoff using complex frequency plane singularities," *Radio Sci.*, vol. 33, pp. 803–819, July–Aug. 1998.

[170] E. W. Peterson, "Acoustic wave propagation along a fluid-filled cylinder," *J. Appl. Phys.*, vol. 45, pp. 3340–3350, Aug. 1974.

[171] L. Tsang and D. Rader, "Numerical evaluation of the transient acoustic waveform due to a point source in a fluid-filled borehole," *Geophysics*, vol. 44, pp. 1706–1720, Oct. 1979.

[172] C. H. Cheng and M. N. Toksöz, "Elastic wave propagation in a fluid-filled borehole and synthetic acoustic logs," *Geophysics*, vol. 46, pp. 1042–1053, July 1981.

[173] F. L. Paillet and C. H. Cheng, "A numerical investigation of head waves and leaky modes in fluid-filled boreholes," *Geophysics*, vol. 51, pp. 1438–1449, July 1986.

[174] R. A. W. Haddon, "Numerical evaluation of Green's functions for axisymmetric boreholes using leaking modes," *Geophysics*, vol. 52, pp. 1099–1105, Aug. 1987.

[175] R. A. W. Haddon, "Exact Green's functions using leaking modes for axisymmetric boreholes in solid elastic media," *Geophysics*, vol. 54, pp. 609–620, May 1989.

[176] Q.-H. Liu and C. Chang, "Compressional head waves in attenuative formations: forward modeling and inversion," *Geophysics*, vol. 61, pp. 1908–1920, Nov.–Dec. 1996.

[177] J. B. Conway, *Functions of One Complex Variable*, Springer-Verlag, New York, 2nd edition, 1978.

[178] K. F. Graff, *Wave Motion in Elastic Solids*, Dover, New York, 1991.

[179] B. K. Sinha and S. Asvadurov, "Higher-order modes in a fluid-filled borehole," in *Proc. IEEE Int. Ultrasonics Symp.*, Sendai, Oct. 5–8, 1998, vol. 2, pp. 1115–1120.

[180] A. N. Norris and B. K. Sinha, "The speed of a wave along a fluid/solid interface in the presence of anisotropy and prestress," *J. Acoust. Soc. Am.*, vol. 98, pp. 1147–1154, Aug. 1995.

[181] C.-H. Hsu and B. K. Sinha, "Mandrel effects on the dipole flexural mode in a borehole," *J. Acoust. Soc. Am.*, vol. 104, pp. 2025–2039, Oct. 1998.

[182] M. A. Biot, "Propagation of elastic waves in a cylindrical bore containing a fluid," *J. Appl. Phys.*, vol. 23, pp. 997–1005, Sep. 1952.

[183] H. Lamb, "On the velocity of sound in a tube as affected by the elasticity of the walls," *Mem. Proc. Manchester Lit. Philos. Soc.*, vol. 42, no. 9, pp. 1–16, July 1898.

[184] R. E. Collin, *Field Theory of Guided Waves*, IEEE Press, New York, 2nd edition, 1991.

[185] D. P. Nyquist, J. M. Grimm, D. J. Infante, and H. Braunisch, "Classification of the proper propagation-mode spectrum and leaky-wave modes on open planar waveguides," *Electromagnetics*, vol. 17, pp. 105–130, Mar.–Apr. 1997.

[186] D. P. Nyquist and D. J. Infante, "Discrete higher-order leaky-wave modes and the continuous spectrum of stripline," *IEICE Trans. Electronics*, vol. E78-C, pp. 1331–1338, Oct. 1995.

[187] D. R. Jackson, D. P. Nyquist, F. Mesa, and C. Di Nallo, "The role of the

steepest-descent path in the excitation of leaky modes on printed-circuit lines," in *Proc. URSI Commission B Int. Symp. Electromagnetic Theory*, Thessaloniki, May 25–28, 1998, vol. 2, pp. 494–496.

[188] D. R. Jackson, F. Mesa, M. J. Freire, D. P. Nyquist, and C. Di Nallo, "An excitation theory for bound modes, leaky modes, and residual-wave currents on stripline structures," *Radio Sci.*, vol. 35, pp. 495–510, Mar.–Apr. 2000.

[189] G. A. Winbow, "A theoretical study of acoustic S-wave and P-wave velocity logging with conventional and dipole sources in soft formations," *Geophysics*, vol. 53, pp. 1334–1342, Oct. 1988.

[190] A. Sommerfeld, "Über die Ausbreitung der Wellen in der drahtlosen Telegraphie," *Ann. Physik*, vol. 28, pp. 665–737, 1909.

[191] A. Baños, Jr., *Dipole Radiation in the Presence of a Conducting Half-Space*, Pergamon, Oxford, 1966.

[192] C.-C. Lu and Q.-H. Liu, "A three-dimensional Green's function for elastic waves in multilayer cylindrical structures," *J. Acoust. Soc. Am.*, vol. 98, pp. 2825–2835, Nov. 1995.

[193] D. Nghiem, J. T. Williams, D. R. Jackson, and A. A. Oliner, "Proper and improper dominant mode solutions for a stripline with an air gap," *Radio Sci.*, vol. 28, pp. 1163–1180, Nov.–Dec. 1993.

[194] C. Di Nallo, F. Mesa, and D. R. Jackson, "Excitation of leaky modes on multilayer stripline structures," *IEEE Trans. Microwave Theory Tech.*, vol. 46, pp. 1062–1071, Aug. 1998.

Biographical note

Henning Braunisch was born in Hanover, Germany, on November 16, 1969.

He received the M. S. degree in electrical engineering from Michigan State University, East Lansing, Michigan, in 1995, and the Dipl.-Ing. degree in electrical engineering from the University of Hanover, Germany, in 1996. The German degree of Dipl.-Ing. is usually considered to be roughly equivalent to an M. S. degree; there is no degree equivalent to the B. S. in the traditional engineering education in Germany.

During the first half of 1997, he was with Philips Research Laboratories, Hamburg, Germany, where he was working on problems of image reconstruction and data processing in cone-beam computed tomography. Since 1997 he has been a research assistant in the Department of Electrical Engineering and Computer Science and the Research Laboratory of Electronics at the Massachusetts Institute of Technology, Cambridge, Massachusetts, where he has concentrated on applications of the theory of fields and waves. He spent the four summers of 1995 and 1998–2000 at Schlumberger-Doll Research, Ridgefield, Connecticut, working on electromagnetic and acoustic, forward and inverse modeling and simulation.

Henning Braunisch is an alumnus of the German National Merit Foundation (1992–96), the Department of State Foreign J. W. Fulbright Graduate Student Program (1994–95), and the German Academic Exchange Service (1997–98). He is a Student Member of the IEEE (since 1999), an Affiliate Member of the Institute of Physics, London (since April 2000), and a member of the Editorial Board of the Journal of Electromagnetic Waves and Applications (since May 2000).